Ministry of Education and Science of Ukraine
Vasyl Stefanyk Precarpathian National University

ISSN 2311-0155

Journal of Vasyl Stefanyk Precarpathian National University

SCIENTIFIC JOURNAL

Series Natural and Mathematical Sciences

Vol. 1, No. 1, 2014

Ivano-Frankivsk
2014

Journal of Vasyl Stefanyk Precarpathian National University

SCIENTIFIC JOURNAL Vol. 1, No. 1, 2014

Recommended for publication by Scientific Council of Vasyl Stefanyk Precarpathian National University
Certificate of State Registration KB No 20385-10185P

Horob Stepan, *Vasyl Stefanyk Precarpathian National University, Ukraine* (Philological Sciences)
Ivashkovych Serge, *University Lille 1, France* (Mathematical Analysis)
Karpiński Mikołaj, *University of Bielsko-Biala, Poland* (Security of Information Technologies)
Klanichka Volodymyr, *Vasyl Stefanyk Precarpathian National University, Ukraine* (Physics of Metals)
Klymychyn Ivan, *Vasyl Stefanyk Precarpathian National University, Ukraine* (Astrophysics)
Kobetska Nadiya, *Vasyl Stefanyk Precarpathian National University, Ukraine* (Landed Law, Agrarian Law, Ecolaw, Natural Resource Law)
Kogut Igor, *Vasyl Stefanyk Precarpathian National University, Ukraine* (Solid State Electronics)
Kononenko Iryna, *University of Warsaw, Poland* (Ukrainian and Polish Language)
Kononenko Vitaliy, *Vasyl Stefanyk Precarpathian National University, Ukraine* (Philological Sciences)
Korobeynikov Georgiy, *National University of Physical Education and Sport, Ukraine* (Physiology of Man and Zoons)
Kosarevych Rostyslav, *Karpenko Physical-Mechanical Institute of the National Academy of Sciences of Ukraine, Ukraine* (Automated Systems, Advanced Information Technology)
Kosiewicz Jerzy, *Józef Piłsudski University of Physical Education in Warsaw, Poland* (Philosophy)
Kotyk Tetyana, *Vasyl Stefanyk Precarpathian National University, Ukraine* (Theory and Methodology of teaching)
Kozak Ihor, *Vasyl Stefanyk Precarpathian National University, Ukraine; The John Paul II Catholic University of Lublin, Poland* (Ecology, Landscape Ecology and Modeling)
Kozak Stefan, *Warsaw University, Poland* (Philological Sciences)
Kozlenko Mykola, *Vasyl Stefanyk Precarpathian National University, Ukraine* (Computer Systems and Components)
Krul Petro, *Vasyl Stefanyk Precarpathian National University, Ukraine* (Theory and History of Culture)
Kugutiak Mykola, *Vasyl Stefanyk Precarpathian National University, Ukraine* (Ethnology)
Kulyk Oleksii, *Ukrainian National Academy of Sciences, Ukraine* (Probability Theory, Mathematical Statistics)
Kurta Sergiy, *Vasyl Stefanyk Precarpathian National University, Ukraine* (Chemical Technology)
Kyyak Svyatoslav, *Vasyl Stefanyk Precarpathian National University, Ukraine* (Philosophy of Science, Philosophy of Education, Religious studies, Ukrainian studies)
Lazarovych Mykola, *Vasyl Stefanyk Precarpathian National University, Ukraine* (Elements and Devices of Computer Facilities and Control Systems)
Łebkowski Piotr, *«AGH» University of Science and Technology, Poland* (Automation and Robotics, Operational Researches, Information Technologies)
Levytsky Andriy, *Taras Shevchenko National University of Kyiv, Ukraine* (German Language)
Lopushansky Oleh, *Rzeszow University, Poland* (Mathematical Analysis)
Lushchak Volodymyr, *Vasyl Stefanyk Precarpathian National University, Ukraine* (Biochemistry)
Lytovchenko Volodymyr, *V. Lashkaryov Institute of Semiconductor Physics of NAS of Ukraine, Ukraine* (Physics of Semiconductors and Dielectrics)
Makarewicz Edwin, *University of Technology and Life Sciences, Poland* (Chemical Technology)
Makcymenko Sergiy, *Institute of Psychology of G.S. Kostyuka NAPN of Ukraine, Ukraine* (Philological Sciences)
Malashkevich Georgii, *National Academy of Sciences of Belarus, Belarus* (Optics, Laser Physics)
Mykhailenko Valeriy, *Bukovyna State University of Finance and Economics, Ukraine* (German Language)
Myronyuk Ivan, *Vasyl Stefanyk Precarpathian National University, Ukraine* (Physics and Chemistry of Surfaces)
Novosyadly Stepan, *Vasyl Stefanyk Precarpathian National University, Ukraine* (Solid State Electronics)
Nykyforchyn Oleh, *Vasyl Stefanyk Precarpathian National University, Ukraine* (Geometry and Topology)
Nykyruy Lyubomyr, *Vasyl Stefanyk Precarpathian National University, Ukraine (*Physics of Semiconductors and Dielectrics*)*
Ostafiychuk Bohdan, *Vasyl Stefanyk Precarpathian National University, Ukraine* (Solid State Physics, Physics and Chemistry of Surface)
Ostapovych Oleh, *Vasyl Stefanyk Precarpathian National University, Ukraine* (German Language)

Editorial address:
Vasyl Stefanyk Precarpathian National University,
57, Shevchenko Str.,
76018, Ivano-Frankivsk, Ukraine
Tel.: +380 (342) 59-60-50
E-mail: jpnu@pu.if.ua
http://jpnu.pu.if.ua/

ISSN 2311-0155

Journal of Vasyl Stefanyk
Precarpathian National University

CONTENTS

Journal of Vasyl Stefanyk Precarpathian National University
http://jpnu.pu.if.ua
Vol. 1, No. 1 (2014), 9-15

UDC 547.791.8, 546.01.05+541.1363 548.736
PACS numbers: 61.18Fs, 81.16.-c, 81.20.Ka, 82.45.Fk, 84.37.+q
doi: 10.15330/jpnu.1.1.9-15

ELECTRIC PROPERTIES OF Mg-SUBSTITUTED LITHIUM IRON SPINEL

L.S. KAYKAN, I.M. GASYUK, V.V. UGORCHUK, J.S. KAYKAN, M.Y. SICHKA

Abstract: Complex impedances of sintered polycrystalline $Li_{0.5}Fe_{2.5-x}Mg_xO_4$ (x = 0.0, 0.1, 0.3, 0.6, 0.8, 1.0) ferrite in the frequency range of 0.01 Hz to 100 kHz were measured at several temperatures in the range of 295-723 K. The complex-plane impedance spectra indicate that the material can be represented by a two-layer leaky capacitor which corresponds to the bulk and the grain boundary phenomena at high and low frequencies respectively. The dependence of impedance and conductivity and dielectric properties on temperature and frequency are discussed.

Keywords: ferrite, complex impedance, dielectric constant, dielectric losses, polarization.

1. INTRODUCTION

Lithium ferrites are of considerable interest owing to their acceptable dielectric properties which depend on a number of factors: a method of preparation [8], temperature [7, 14], atmosphere of sintering [7, 8], as well as iso- and heterovalent substitution [2]. The structure of a spinel being crystal, it allows to carry out substitution in a fairly wide range, while remaining one phase. Especially interesting in this case are ions of magnesium. With a slight advantage over the oxygen octaenvironment in the spinel structure ions of magnesium can move in both sub lattices replacing iron practically in a stoichiometric ratio [3]. In their electric properties ferretes belong to the class called valency-controlled semiconductors. This is a group of transition metals oxides with a blank 3d - shell, so they are under certain conditions [11] may obtain a metallic type of conductivity. However, samples of stoichiometric composition in the absence of additives are dielectrics. Conductivity of these oxides can be increased by introducing in the lattice additives of other elements [11]. Low resistance, due to the simultaneous presence of two- and trivalency ions of iron in the equivalent nodes of stoichiometric oxides lattice, can also be achieved by a valency - controlled method. If a small amount of extraneous ions, valence of which differs from the valency of stoichiometric composition, is introduced in the oxide with a high resistance, then a part of ions changes its valence. As a result, ions of the same atom have different valence, and electrical resistance of oxide falls [4].

In order to find out the impact of substitution on the dielectric properties of *Mg*-doped lithium iron spinels, we have by method of complex electric impedance conducted a systematic research of dielectric constants and losses of tangent as a function of composition and the frequency both at room temperature and in a wide temperature range.

2. EXPERIMENTAL PROCEDURE

Synthesis of the general stoichiometric composition $Li_{0.5}Fe_{2.5-x}Mg_xO_4$ (x = 0.0, 0.1, 0.3, 0.6, 0.8, 1.0) was a standard ceramic technology of double sintering with outgoing oxides Fe_2O_3, MgO and lithium hydroxide *LiON* grade. An X-ray study of synthesized compounds on the diffractometer DRON-3 in $CuK\alpha$- radiation showed the samples obtained as single-phase and their belonging to the spatial group Fd3m, cation distribution was found by Ritveld' method. Based on cationic distribution of magnesium and iron ions as well as on the terms of electroneutrality it was discovered that lithium ions were both in octa- and tetra positions [3]. In this same work the results of x-ray studies were confirmed by the method of messbauer spectroscopy.

Coinductivity of alternating current, the tangent of losses, the real and imaginary parts of penetration were determined on the basis of experimental dependencies of complex impedance, obtained at the spectrometer $Autolab\,PGSTAT\,12/FRA-2$ in the frequency range 0.01Hz-100 kHz. The temperature dependence obtained was based on the impedance studies in step-by-step mode heating with isothermal exposure after every 50 degrees in the temperature range 295-723 K. Frequency dependence of dielectric functions was derived from the experimental Nyquist 's diagram (Fig. 2, b):

$$\varepsilon^* = \varepsilon' - j\varepsilon''$$

$$M^* = M' + jM''$$

$$Z^* = Z' - jZ''$$

$$Y^* = Y' + jY''$$

$$\tan\delta = \frac{\varepsilon''}{\varepsilon'}$$

$$\varepsilon^* = j\omega C_0 Y^*$$

where ε^* - complex dielectric permeability, M^*- complex coefficient (module), Z^* - complex impedance, Y^*- comprehensive admittance, ω- cyclic frequency, j- imaginary unit, C_0- capacity of the system.

3. RESULTS AND DISCUSSION

The change of the specific resistance to direct current ρ_{dc} and dielectric constant ε' depending on the content of magnesium ions are shown in Fig. 1. As it can be seen from the Figure, ρ_{dc} and ε' are mutually inverse dependent. This tendency is quite understandable, since the basis of activity of conductivity and polarization of ferrite systems are one and the same processes; and it is a jump of an electron $Fe^{2+} \leftrightarrow Fe^{3+} + e^-$ that results in a local bias charge and holds responsible for polarization. The presence of Fe^{2+} in the octahedral cavities of iron spinels is decisive for implementation of the intermittent mechanism of conductivity and depends on the conditions of synthesis: time of sintering[8], temperature [14], the speed of cooling [14, 3], etc. With increasing the content of Mg^{2+} ions is natural, and it decreases the concentration of Fe^{2+} ions [14], however, as is seen from Fig. 1, resistivity weakly depends on the content of magnesium ions in $x \geq 0.1$. The following behavior can be clearly explained by the fact that the presence of lithium ions in the octasublattice leads to the formation of complexes of the type $[Li^+ + Fe^{3+}]$ that in general behave like Fe^{2+} and capable to take a ' wandering' electron, and so get involved in the intermittent mechanism of conductivity. The frequency of electronic navigation $Fe^{3+} + e \leftrightarrow Fe^{2+}$ depends on the structure of ferrites, concentration of defects, loosely-tied electrons, and temperature of ferrites. Transitions $Fe^{3+} + e \leftrightarrow Fe^{2+}$ occur

between Fe ions in the octahedral cavities, as in small tetrahedral intervals iron ions can be found mainly in the three-valency state. Loosely-tied electrons are responsible for the semiconductor properties of ferrite and determine its main electrical properties.

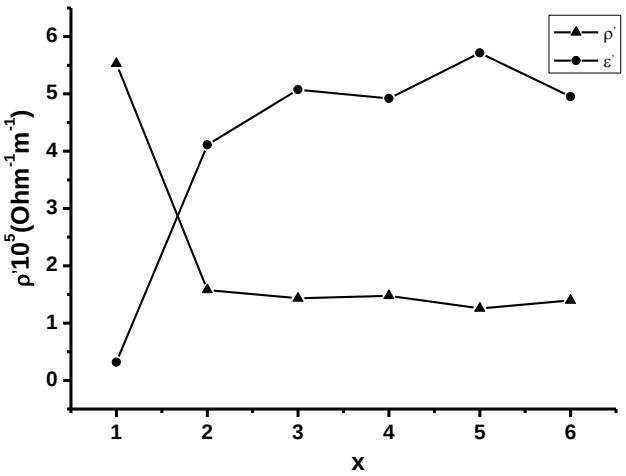

Fig. 1. Dependence of dielectric permeability and conductivity on the direct current from the samples of $Li_{0.5}Fe_{2.5-x}Mg_xO_4$ *(x = 0.0, 0.1, 0.3, 0.6, 0.8, 1.0)*

In Fig. 2 is frequency dependence of conductivity of the sample composition of $Li_{0.5}Fe_{2.4}Mg_{0.1}O_4$ at different temperatures. At relatively low temperatures conductivity defects dependency on frequency, however, ranging from temperature 573K such dependence disappears , indicating the metal-type of conductivity. Frequency dispersion of conductivity at low temperatures is often associated with determining influence [6] inter crystalline transitions.

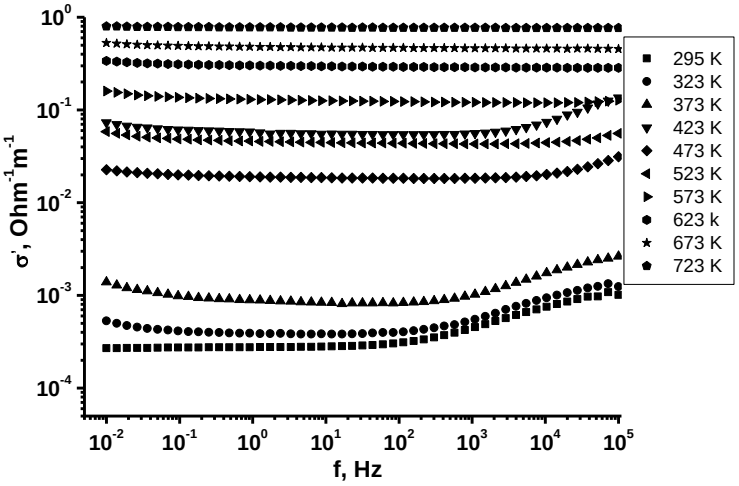

Fig. 2. Dependence of the real part of conductivity on frequency of the system of $Li_{0.5}Fe_{2.4}Mg_{0.1}O_4$

This change of electrophysical settings can be explained within a model of heterogeneous leading environment [10], which is polycrystalline ferrites. According to this model, the strata of varying conductivity occur both on the framework of grains and other inhomogeneities, such as i.e.,domains, dislocations, etc. On the framework emerge locking layers from different sides of such heterogeneities, and locking layers are oriented in straight and locking directions at a certain polarity of the external field. In the works [1, 10] it is concluded that the growth of conductivity with temperature and frequency in polycrystals are due to the effect of tunneling electrons through the inter grain layer. Thus, electrophysical parameters are largely determined by the microstructure of samples.

In Fig. 3 temperature dependences of real and imaginary parts of dielectric permeability of samples. $Li_{0.5}Fe_{2.5-x}Mg_xO_4$ (x = 0.1, 0.3, 1.0).

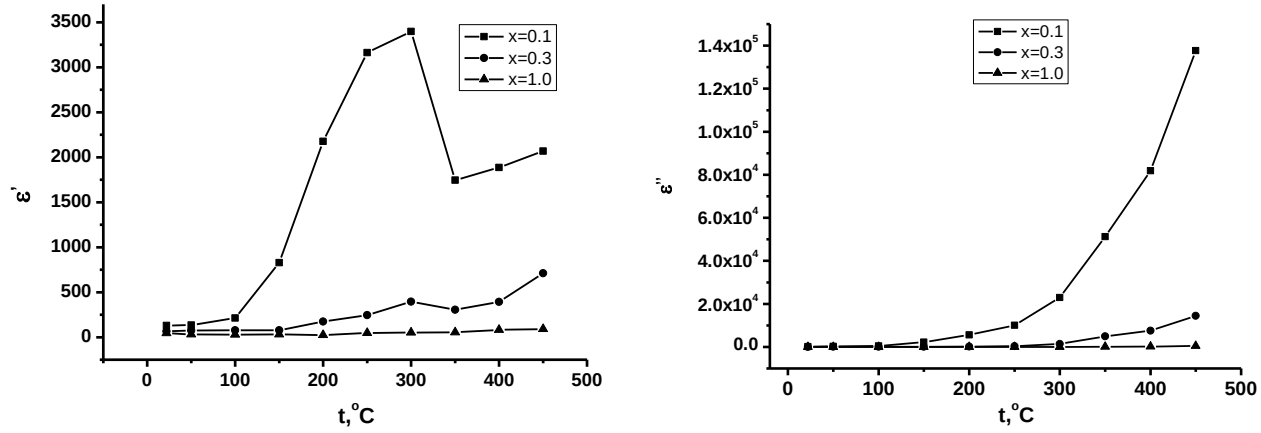

(a) *(b)*

Fig. 3. Temperature dependence of real (a) and imaginary (b) part of dielectric permeability of samples $Li_{0.5}Fe_{2.5-x}Mg_xO_4$ *(x = 0.1, 0.3, 1.0)*

Temperature dependencies ε'' are described by smooth curves , the progress of which has a different character in low and high temperatures. With increasing temperature above T=400K, the imaginary part of dielectric permeability grows stronger with decreasing content of *Mg* ions. Temperature dependences of the real part of dielectric permeability are characterized by the presence of the peak which is most strongly manifested by the sample composition $Li_{0.5}Fe_{2.4}Mg_{0.1}O_4$. With increasing content of *Mg* ions its position shifts in high temperature and is accompanied by a decrease in intensity. For the sample with the greatest concentration Mg^{2+} this peak is missing, and weak dependence of the real part of dielectric permeability can be observed. Dependencies of σ and ε on frequency f and temperature *T* for polycrystalline ferrites [5] are made to interpret within a model of interlayer polarization and interlayer polarization with the participation of external condition of inter grain framework. One of the main reasons for the emergence of interlayer polarization is the process of electrical transfer. Obviously, a certain temperature (in this case 475-575 K) activates electronic transitions between the ions of variable valence ($Fe^{2+} + Fe^{3+} \rightarrow Fe^{3+} + Fe^{2+}$) and such a recharge of ion pairs is the process of dipole reorientation in an alternating field. We can assume that the growth of ε' is due to polarization or (it is more probable) a recharge of pairs in the electrical domains formed spontaneously at this temperature under the influence of the applied electric field. Preceding from this assumption we can suggest that with increasing temperature of the sample these domains are destroyed as a result of the growth of thermal motion of ions, and, as it can be seen from Fig. 2, b, causing the reduction of dielectric permeability. A slight growth of $\varepsilon'(T)$ at temperatures above 625 K is apparently caused by individual recharge of iron ions of different valency. This phenomenon is observed in the works [9, 13], which make assumptions about the manifestation of the effect of ferroelectrics.

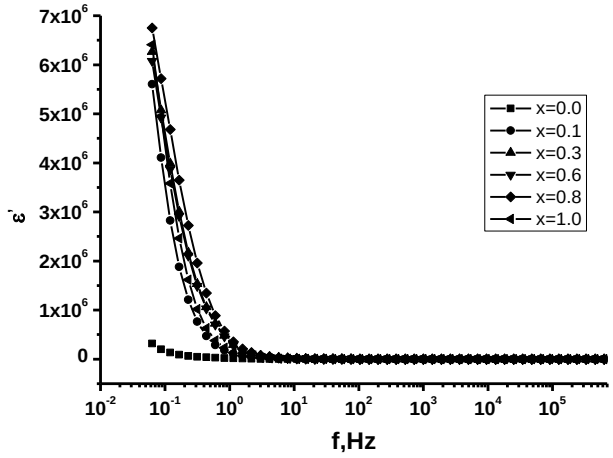

Fig. 4. Dependence of the real part of dielectric permeability on frequency

Frequency and temperature characteristics of dielectric permeability of ferrites to a great extent depend on their composition and structure. At room temperature and frequency of 0.01 Hz the value of ε' is a value of 10^6 order for all compositions, with increasing frequency comes the reduction of value ε' and makes up 10-20 at high frequencies. Dipoles that are formed under the influence of an alternating electric field by electrons and ionic vacancies are obviously the main reason for high dielectric permeability of samples. However, other processes can contribute to the value of this magnitude, the processes that take place in ferrites, in particular, those that are related to the heterogeneity of these systems.

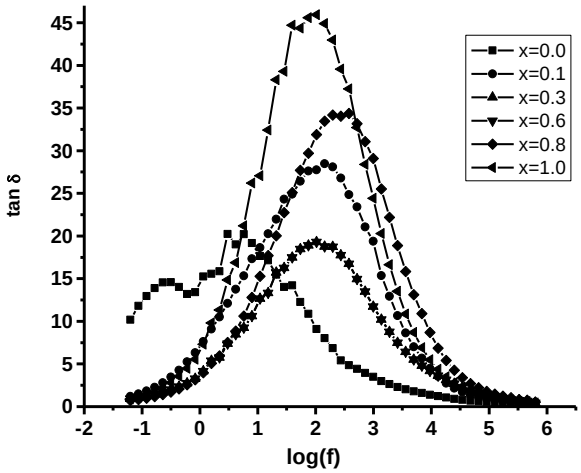

Fig. 5. Dependence of dielectric tangent of losses (tgδ) on the frequency in the samples of $Li_{0.5}Fe_{2.5-x}Mg_xO_4$ *(x = 0.0, 0.1, 0.3, 0.6, 0.8, 1.0)*

In an alternating electric field all processes of displacement and orientation of ferrite particles will have a place until the time these processes are smaller than a half period of changes in an external electric field. The important characteristic is the time of relaxation τ that determines the orientation of the dipole in an alternating electric field. In connection with the late relaxative polarization the energy is dissipated and heats up on the alternating current. The power dissipated in the unit of volume is characterized by a tangent of angle of dielectric losses *(tgδ)*. In Fig. 5 is a frequency dependence of dielectric tangent of losses, in which you can see that the height and shape of the curve depend on the composition and microstructure of samples. For x=0.0 there are two distinctly separated peaks at frequencies 10^{-1} and 10 Hz which usually contribute to the polarization of grains and their framework. Significant expansion of the curve for other samples suggests the presence of two kinds of contribution to polarization that occur at two similar frequencies. The average value of relaxation time for samples

of *Mg* - substituted lithium-iron spinel $Li_{0.5}Fe_{2.5-x}Mg_xO_4$ (x = 0.0, 0.1, 0.3, 0.6, 0.8, 1.0), obtained from experimental dependencies of tangent of dielectric losses on frequency, is from 0.014 (for x=0.8) to 0.047 (for x=1.0). Dependence of relaxation time on composition is in Fig. 6.

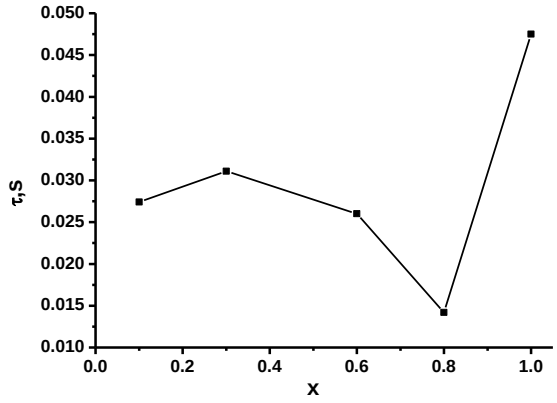

Fig. 6. Dependence of relaxation time of polarization on the content of magnesium ions

Peak expansion of tangent of dielectric losses ($\tan\delta$), as well as the value of relaxation time point out the existence of relaxation time dependence on frequency and not on its constant value [5]. This distribution of relaxation time is a consequence of the difference in the inner circle of different ions in the structure under study, besides, of influence are temperature fluctuations of the lattice at room temperature.

4. CONCLUSION

An impedance range-based analysis shows that behavior of temperature dependence of the real part of dielectric permeability is characterized by the presence of the maximum in the temperature range of 475-575 K that is evidently connected with the processes of activating electronic transfers between ions of variable valence , and is accompanied by dipole reorganization in the AC field. A characteristic view of frequency dependence σ' testifies to the presence in a *Mg*-substituted lithium – iron spinel $Li_{0.5}Fe_{2.4}Mg_{0.1}O_4$ d_c – electric conductivity, the contribution of which increases with temperature, and at T> 573 K its share in conductivity gets predominant.

REFERENCES

[1] Abdullah M.N., Yusoff A.N. Complex impedance and dielectric properties of an Mg-Zn ferrite. *Journal of Alloys and Compounds*, **233** (1996), 129-135.

[2] Bayukov A.A., Savytskyy A.F. Covalence effects and electronic configuration of the valence shells of the ions in ferrites – spinels. *Inst. of Physics*, **568** (1989), 1-21. Preprint: AN USSR SB (in Russian)

[3] Gasyuk I.M., Kaykan L.S., Halihuzova S.A., Yakubovskyy P.P. Mössbauer and X-ray diffraction studies-substituted lithium-iron spinels. *Scientific Bulletin of Chernivtsi University: Proceedings. Physics. Electronics*, **438** (2009), 100-106. (in Ukrainian)

[4] Kony D.El. Dielectric Relaxation in Al-Substituted Ni-Cd Spinel Ferrites. *Egypt. J. Solids*, **27** (2) (2004), 285-297.

[5] Koops C.G. On the Dispersion of Resistivity and Dielectric Constant of Some Semiconductors at Audiofrequencies. *Phys. Rev.*, **33** (1) (1951), 121-124. doi: 10.1103/PhysRev.83.121

[6] Kozlov G.V., Lebedev S.P. Dielectric dispersion of $(NH_4)_2SO_4$ in the near-millimetre and far-infrared range: manifestations of disorder. *J. Phys. C: Solid State Phys.*, **21** (1988), 4883-4894. doi: 10.1088/0022-3719/21/28/005

[7] Krupychka S. *Physics Ferrite and their Related Magnetic Oxides*. Mir, Moscow, 1976. (in Russian)
[8] Letyuk P.I., Zhuravlev G.I. *Chemistry and Technologies ferrites.* Chemistry, Leningrad, 1983. (in Russian)
[9] Malyshev A.V., Peshev V.V., Prytulov A.M. Temperature dependences of the dielectric properties of lithium-titanium ferrite ceramics. *FSS*, **46** (1) (2004), 185-188. (in Russian)
[10] Mansour S.F. Frequency and Composition Dependence on the Dielectric Properties for Mg-Zn Ferrite. *Egypt. J. Solids*, **28** (2) (2005), 263-273.
[11] Mazen S.A., Zaki H.M. AC conductivity of Li-Ge ferrite. *J. Phys. D: Appl. Phys*., **28** (1995), 609-613. doi: 10.1088/0022-3727/28/4/00
[12] Ostafyychuk B.K., Gasyuk I.M., Kaykan L.S. Dielectric properties of magnesium-substituted lithium iron spinel thermal impedance studies. *Electrochemical Energy*, **11** (1) (2011), 18-25. (in Russian)
[13] Palatnykov M.N., Sandler V.A., Efremov V.V. Dielectric properties and conductivity of ferroelectric solid solutions $Li_xNa_{1-x}Ta_{0.1}Nb_{0.9}O_3$. *Inorganic Materials*, **47** (1) (2011), 61-68. (in Russian)
[14] Zhuravlev G.I. *Chemistry and Technologies ferrites.* Chemistry, Leningrad, 1970. (in Russian)

Address: L.S. Kaykan, I.M. Gasyuk, V.V. Ugorchuk, J.S. Kaykan, M.Y. Sichka: Vasyl Stefanyk Precarpathian National University, 57, Shevchenko Str., Ivano-Frankivsk, 76025, Ukraine.
E-mail: uhorchuk@rambler.ru; gasyukim@pu.if.ua.
Received: 01.11.2013; **revised:** 17.03.2014

Кайкан Л.С., Гасюк І.М., Угорчук В.В., Кайкан Ю.С., Січка М.Я. Електричні властивості магній – заміщеної літій – залізної шпінелі. *Журнал Прикарпатського університету імені Василя Стефаника*, **1** (1) (2014), 9–15.

Полікристалічні ферити $Li_{0.5}Fe_{2.5-x}Mg_xO_4$ (x = 0.0, 0.1, 0.3, 0.6, 0.8, 1.0) досліджувались методом комплексного імпедансу в частотному діапазоні від 0,01 Гц до 100 кГц при різних температурах в околі 295-723 К. Спектри комплексного імпедансу показали, що досліджуваний матеріал може бути представлений у вигляді двошарового конденсатора, властивості яких відповідають за зерна і границі зерен матеріалу при високих і низьких частотах. Обговорюються температурні залежності провідності та діелектричної проникності.

Ключові слова: ферити, комплексний імпеданс, діелектрична проникність, діелектричні втрати, поляризація.

Journal of Vasyl Stefanyk Precarpathian National University
http://jpnu.pu.if.ua
Vol. 1, No. 1 (2014), 17-25

UDC 544. 018 : 544. 723
PACS numbers: 61.43.Gt, 81.07.Wx, 88.80.F, 82.47.Uv
doi: 10.15330/jpnu.1.1.17-25

THE IMPACT OF THE SURFACE MORPHOLOGY ON ENERGY CHARACTERISTICS OF NANOPOROUS CARBON MATERIAL

B.K. OSTAFIYCHUK, I.M. BUDZULYAK, B.I. RACHIY, L.O. SHYYKO,
R.P. LISOVSKY, N.YA. IVANICHOK, V.M. VASHCHYNSKY

Abstract: The impact of nanoporous carbon material (PCM) morphology on its electrochemical behavior in aqueous electrolyte has been studied. The optimum concentration of aqueous lithium sulfate which provides the maximum specific energy characteristics of capacitor-type systems C/Li_2SO_4/C is determined. Capacitive parameters of electrochemical capacitors (EC) in aqueous solutions of lithium, sodium and potassium sulfate which have different molar ratio have been studied by comparative analysis. Cyclic voltammograms at different scan rates show that the PCM capacitive behavior in three electrolytes increases in the following order Li_2SO_4<Na_2SO_4<K_2SO_4. This improvement could be a result of increasing the movement speed of hydrated ions in the volume of electrolyte and in the internal pores of PCM in the order Li^+<Na^+<K^+. The obtained results give valuable information for the study of new hybrid supercapacitors.

Keywords: activated carbon material, double electric layer, electrolyte, specific capacity, internal resistance, electrochemical capacitor.

1. INTRODUCTION

Electrochemical capacitors that employ charge/discharge of the electrical double layer (EDLC) occupy an intermediate position between electrochemical batteries and conventional capacitors. The first part of the devices has high energy density with relatively low power density, and the second one has a relatively large capacity at sufficiently low energy density [3]. The increase in operating voltage of EC based on aqueous electrolyte is possible in the so-called hybrid capacitors (HC). It is a hybrid of a supercapacitor and a lithium-ion battery. A hybrid capacitor (HC) differs from a supercapacitor in discharge time (up to 1 hour) and energy density, which is higher with less number of recharge cycles [13]. As it follows from the ref. [2], the electrochemical system is based on a lithium manganese spinel as a cathode, and nanoporous carbon as an anode in Li_2SO_4 aqueous solution, has specific energy density to 30 $J \cdot kg^{-1}$. As electrolytes based on Na_2SO_4 and K_2SO_4 salts are more affordable than Li^+-based electrolytes, it is interesting to compare the energy characteristics of PCM in salt solutions of varying molar ratio.

HC energy characteristics largely depend on the specific capacity of the anode, which is made of PCM. In theory, the greater the surface area of PCM is, the higher specific capacitance is expected. However, the practical situation is more complicated. Experimental capacity usually depends on the

ratio between pore size distribution in carbon material and the size of solvated ions in the electrolytes [7, 8, 14]. The main reason is that nanopores with a small diameter are not available for electrolytic solution. The fact is that ions with their solvating shell are too big to get into nanopores. Therefore, the surface area with this type of nanopores does not make any contribution to the overall capacity of EDLC electrode material. For example, the radius of solvated ions in organic electrolytes is mostly larger than in aqueous electrolytes. As a result, the carbon electrode with a greater number of macropores, is mainly used in/with organic electrolytes [11, 12, 15]. In order to improve the specific energy characteristics of the EC one should study the interrelation of carbon material structural characteristics (specific surface area, pore size distribution and pore volume) for a particular electrolyte.

In this paper we investigate the correlation between structural and energy parameters of PCM which is used to make SC electrodes and HC anodes in sulphate aqueous solutions of lithium, sodium and potassium of varying molar ratio.

2. MATERIALS AND METHODS

As the object of study we use PCM obtained from a raw material of plant origin by hydrothermal carbonization of feedstock.

The process passes under pressure of water vapor $(12 \div 15)\cdot 10^5$ Pa and further thermal activation at temperature of 673 ± 3 K [9].

Determination of structural and adsorption characteristics of the material was carried out use of nitrogen adsorption at temperature T= 77 K by surface area analyzer Quantachrome Autosorb (Nova 2200e). The samples were previously degassed in a stream of helium at 453 K during 20 h. The calculation of adsorption isotherms allowed to obtain pore size distribution, specific surface area and specific pore volume. Electrochemical studies were conducted in a two-electrode cell (type "2525") with the spectrometer Autolab PGSTAT/FRA-2. EC electrodes were made from the mixture:

$$<PCM>:<CA>:<BM>=<75>:<20>:<5>,$$

where *CA* is a conductive additive (acetylene carbon black, graphite KS-15 of «Lonza» company), *BM* is a binding material (F-42L) [4]. In order to study specific capacity that depends on the rate of the EDL charge/discharge process we used a volt-ampere method with scanning rates from 1 to 50 $mV\cdot s^{-1}$. The rate of voltage change on the EC:

$$s = \pm\frac{dU}{dt}$$

and the corresponding capacitor current is associated with capacity by the equation

$$I = C\frac{dU}{dt}$$

or

$$I = Cs$$

PCM specific capacity is calculated by the formula:

$$C_{sp} = \frac{2I}{sm}$$

where I is the current of anodic or cathodic branches of a current-voltage curve, s is a scanning rate, m is an active electrode mass. The specific capacity of carbon material depends on discharge current,

which varied with a range of 1 and 50 mA, and is calculated by a galvanostatic method. The specific capacity of PCM was calculated by using the formula:

$$C_{sp} = \frac{I \cdot t_p}{(U - \Delta U) \cdot m}$$

where I is a discharge current, t_p is discharge time, $U - \Delta U$ is the potential difference between the extreme points of the discharge curve, m is mass of PCM.

Internal resistance is determined by a potential jump after 10 cycles of charge/discharge.

$$\Delta U = 2IR$$

where ΔU is a potential jump at discharge.

3. RESULTS AND DISCUSSION

In carbon particles pores of different size, shape and volume formed depending on the time of thermal activation. For research we selected carbon material, which had the maximum specific surface area and micropore volume.

The specific surface area was calculated by the multipoint BET method with a linear dependence of $1/[W(P_0 / P) - 1]$ on P / P_0 in the adsorption isotherm P / P_0 range from 0.05 to 0.35. The total volume of pores with a radius less than 152.43 nm was determined under pressure of saturation, $P / P_0 = 0.99$. The average pore diameter was calculated according to the method of Horvath-Kawazoe. Table 1 shows the structural and adsorption characteristics of PCM.

Parameter	PCM
Surface area Multipoint BET, $S_a(m^2 \cdot g^{-1})$	800±20
Total pore volume, $V_{total}(sm^3 \cdot g^{-1})$	0.4179
Volume of micropores, $V_m(sm^3 \cdot g^{-1})$	0.2962
Surface area of micropores, $S_m(m^2 \cdot g^{-1})$	722.5
Average pore diameter, $D_{HK}(\overset{0}{A})$	7.224

Tab. 1. Structural and adsorption characteristics of PCM

The adsorption isotherm analysis (Fig. 1, a) of PCM made it possible to determine the specific surface area, total pore volume and distribution both in size and volume (Fig. 1).

Electrochemical studies of carbon materials were performed in 0.5M, 1M, 2M, 3M and saturated aqueous salt solution of Li_2SO_4. Cycle volt-ampere curves of electrochemical capacitors with these electrolytes are shown in Fig. 2.

At low scanning rates the curves of all five electrolytes are close to symmetrical rectangular shape without any peaks which are responsible for the occurrence of redox processes in the system. This waveform is a typical capacitive behavior of EC. With increasing the scanning rate the deviations from the ideal rectangular shape occur due to the reduction of movement time of solvated ions along working pores.

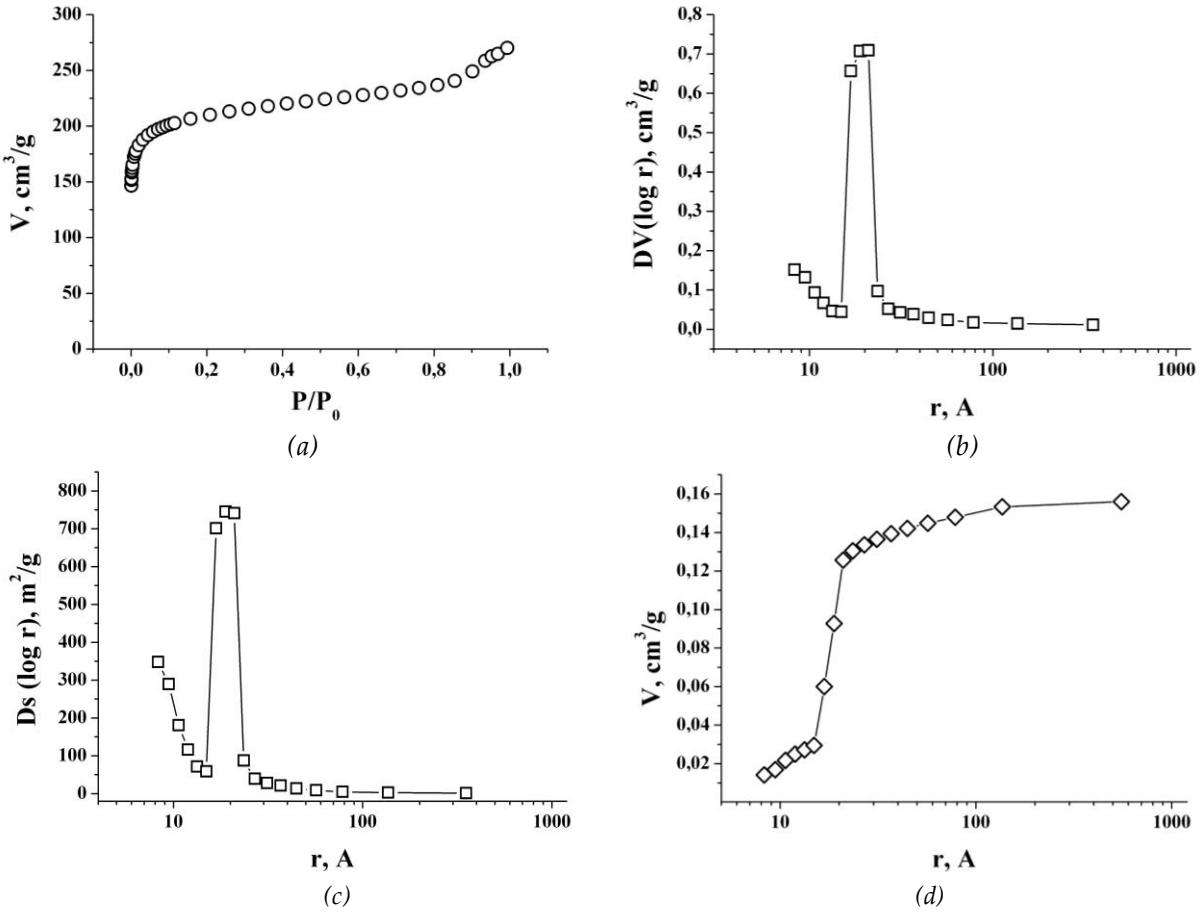

Fig. 1. Adsorption isotherm of nitrogen (a), pore size distribution (b), dependence of specific surface area on pore radius (c), dependence of pore volume on pore radius (d)

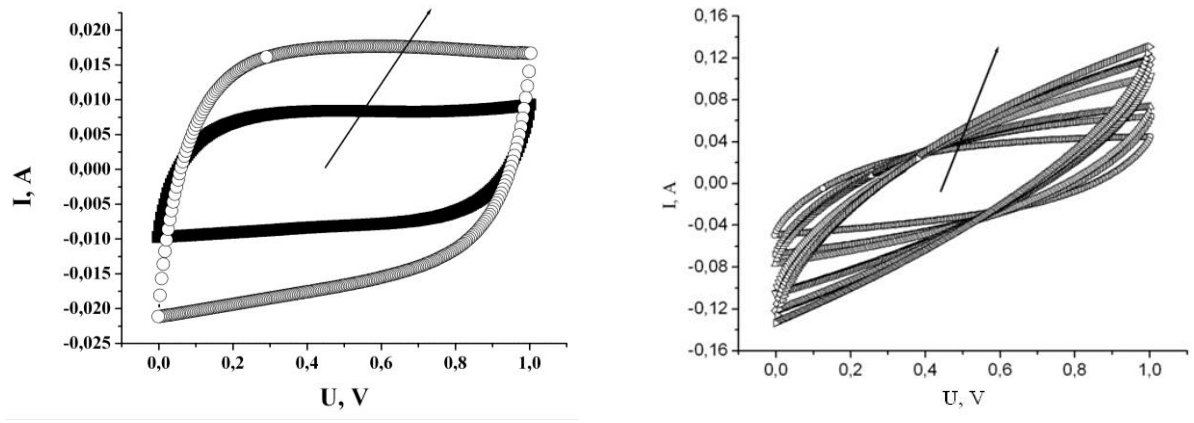

Fig. 2. Cycle volt-ampere characteristics of PCM in 2M aqueous solution of Li_2SO_4. Scanning rates: (a) 1, 2 mV·s^{-1}, (b) 5, 8, 10, 20, 30, 40 mV·s^{-1} (arrow indicates the direction of the scanning rate increase s)

To study the capacitive behaviour of PCM in these electrolytes, the dependence of the specific capacity on the potential change rate of the cell was investigated.

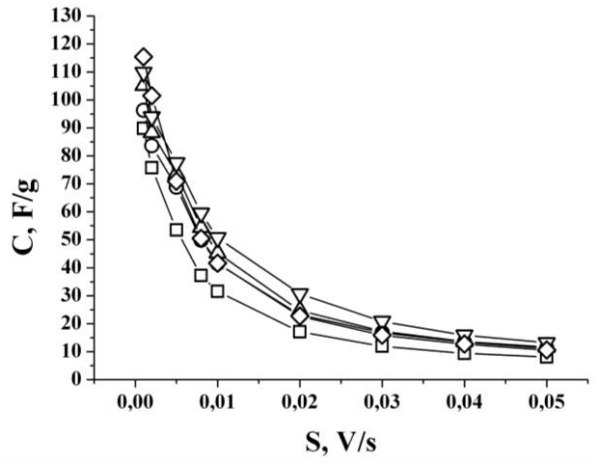

Fig. 3. Dependence of specific capacity of PCM in aqueous solution of Li_2SO_4 on scanning rate for electrolytes of various molar ratio: 0.5 M —□—, 1 M —○—, 2 M — Δ —, 3 M — ∇ —, saturated —◊ —

Figure 3 shows that at low scanning rate (up to 5 $mV \cdot s^{-1}$) carbon material in saturated aqueous salt solution of Li_2SO_4 has the highest specific capacity. It is associated with maximum concentration of electrolyte ions and low charge rate, providing sufficient time for EDL formation. With the increase of the scanning rate (5 to 30 $mV \cdot s^{-1}$) carbon material has a maximum capacity in 3M aqueous salt solution of Li_2SO_4. In our view, it has an optimal ratio between the electrolyte ions concentration and their mobility, providing maximum capacity of EDL. For all samples with the increase of the scanning rate above 10 $mV \cdot s^{-1}$, there is a decrease of specific capacity, which can be explained by low mobility of ions within certain micropores. In the studied carbon materials there is an insufficient number of transport pores, which provide free access of electrolyte ions to the micropores, and the volume of micropores of radius 1.8 - 2.2 nm amounts to 70% of the total pore volume. Therefore, a high scanning rate increases a number of micropores, in which the EDL is not formed completely and results in the reduction of specific capacity of PCM at high charge/discharge rates.

A sharp voltage drop at constant discharge current reveals the presence of ohmic resistance of the supercapacitor. According to ref. [5], the voltage drop $\Delta U_R = IR$ is defined as an intersection point between the voltage curve, which is linearly extrapolated and the axis of time immediately after the discharge circuit is closed. If a voltage drop exceeds 20% of the maximum, discharge current should be reduced twofold, fivefold or tenfold times. Fig. 4 shows the dependence of PCM capacity and voltage drop on the applied discharge current.

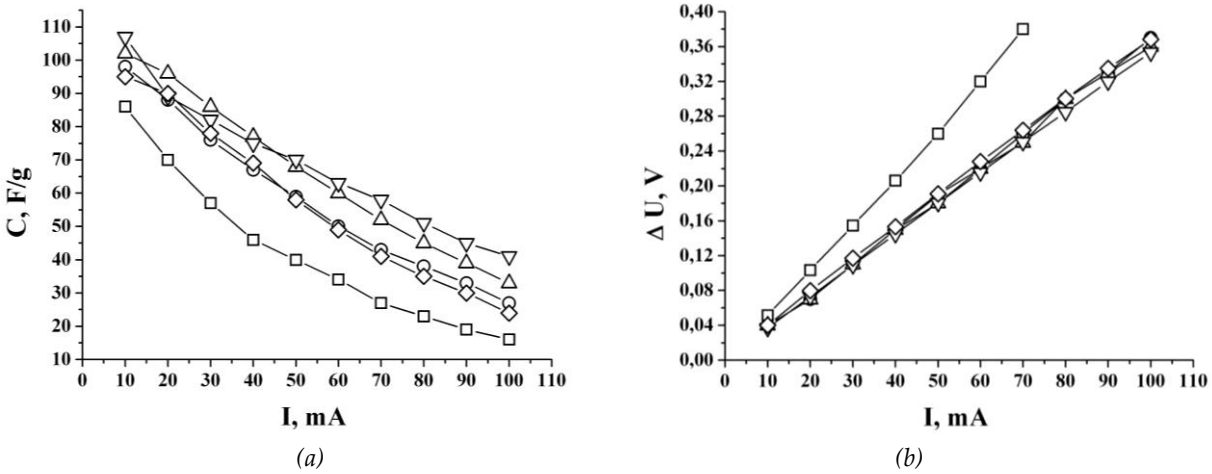

(a) *(b)*

Fig. 4. Dependence of specific capacity of PCM (a) and voltage drop (b on discharge current in aqueous solution of Li_2SO_4 for electrolytes of various molar ratio: 0.5 M —□—, 1 M —○—, 2 M — Δ —, 3 M — ∇ , saturated —◊ —

For all samples the specific capacity decreases with the increase of discharge current (Fig. 4, a), and the maximum operating discharge current is up to 50 mA. With further increase in current the voltage drop exceeds 20% of the maximum voltage during the discharge.

To determine the occurrence of possible chemical reactions for PCM in 0.5 M aqueous salt solution of Li_2SO_4, Na_2SO_4 and K_2SO_4 the electrochemical research into potential 0 ÷ 1 V was performed. Fig. 5 shows cyclic volt-ampere characteristics with the scanning rate of 1 and 20 $mV \cdot s^{-1}$, respectively.

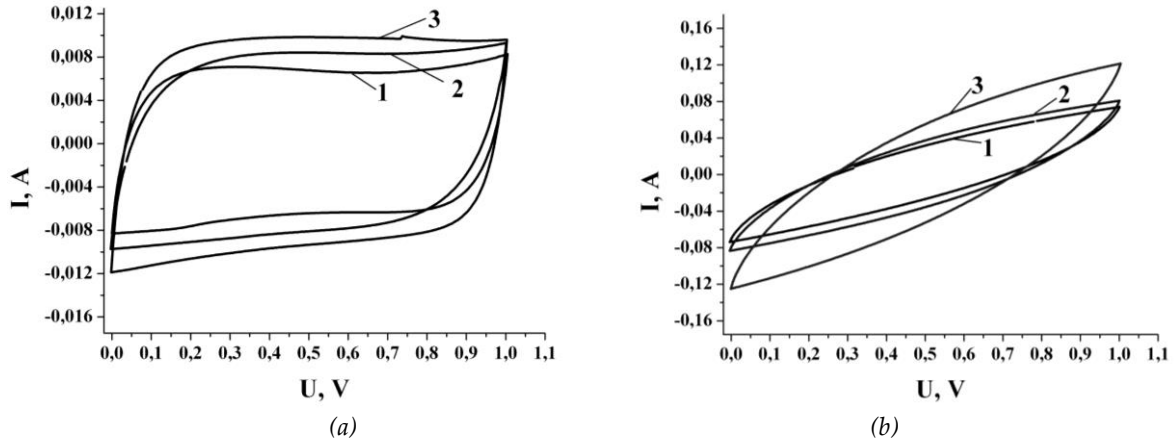

Fig. 5. Potentio dynamic curves for PCM in 0.5M aqueous solution of 1 – Li_2SO_4, 2 – Na_2SO_4 i 3 – K_2SO_4 at scanning rate 1 mV/s (a), 20 mV/s (b)

When scanning rate numbers 1 $mV \cdot s^{-1}$ VA-curves of all the three electrolytes show a symmetrical shape close to rectangular without any noticeable redox peaks that are characteristic of capacitive behavior. The values of specific capacity of PCM in three electrolytes obtained at low scanning rates also do not show any significant differences, either. As a result of the relaxation time for movement of solvated ions at high scanning rate, all the curves deviate from the ideal rectangular shape and the capacity value in aqueous electrolytes increases in the order Li_2SO_4 <Na_2SO_4 <K_2SO_4.

Whereas there are no visible peaks on the volt-ampere characteristics obtained, as is the case of galvanic cells (batteries supply), it can be argued that the electrolyte has a chemical and electrochemical stability in the attached potential field [1].

Getting cyclic volt-ampere curves made it possible to calculate the specific capacity C_n of the investigated PCM. Dependence of the material specific capacity on the scanning rate is shown in Fig. 6.

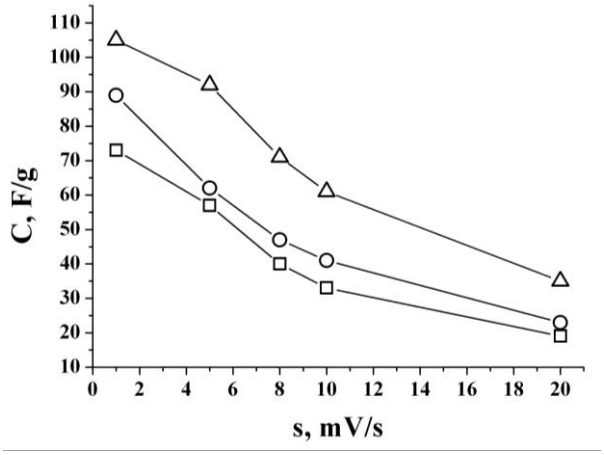

Fig. 6. Dependence of specific capacity of PCM in 0.5 M aqueous Solution of Li_2SO_4 - ■ -, Na_2SO_4 - ○ - and K_2SO_4 – on the scanning rate s

As is seen in the figure, the value of specific capacity decreases due to the increasing scanning rate. PCM in the aqueous salt solution of Li_2SO_4 has the lowest specific capacity and in aqueous K_2SO_4 the largest. This may be due to the fact that hydrated ions have different radius, i.e. Li^+ (3.82 Å), Na^+ (3.58 Å) and K^+ (3.31 Å), and different charge densities and movement rates [6, 10]. Based on the fact that the hydrated K^+ ions are the smallest and their ionic conductivity are the highest and movement time of hydrated K^+ ions along the pore is the shortest, it can be concluded that it is easier for them to achieve the internal pore of PCM than Na^+ and Li^+. As a result, EC-based on aqueous solution of K_2SO_4 have the highest specific capacity at a high scanning rate. From the above it can be concluded that capacity increases in the order $Li^+ < Na^+ < K^+$.

The investigated PCM was used to form EC-cases of standard size "2525". As an electrolyte we used 0.5 M aqueous solution of Li_2SO_4, Na_2SO_4 and K_2SO_4. Than we carried out measurements of capacity and internal resistance for EC.

A sharp voltage drop at a constant discharge current indicates the presence of internal resistance in EC. The technique consists in the oscillographic fixing of voltage drop (ΔU) of the capacitor at the time of its connection to a specific external resistance, and it is the closest method of practical application in EC internal resistance measurement. Fig. 7 shows the dependence of voltage drop of EC on the current applied.

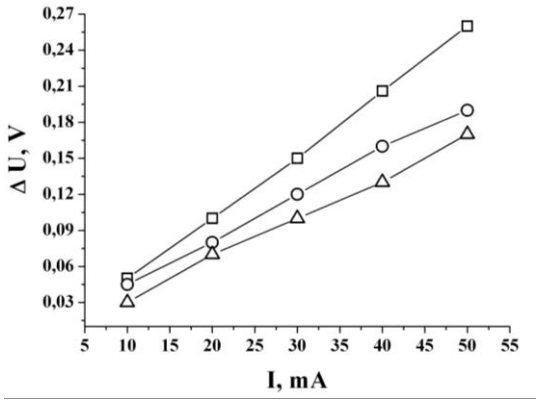

Fig. 7. Dependence of voltage drop of EC in 0.5M aqueous solution of Li_2SO_4 —■—, Na_2SO_4 —○— i K_2SO_4 — Δ — on discharge current

Specific capacity of samples was defined by using a galvanostatic method. The essence of this method is to determine the potential *U* depending on the time *t* at a constant current. As it can be seen in Fig. 8, for all the studied electrochemical systems capacity value decreases with the increase of discharge current. The maximum discharge current is 50 mA as further on its increase voltage drop exceeds 20 % of the maximum voltage during the discharge.

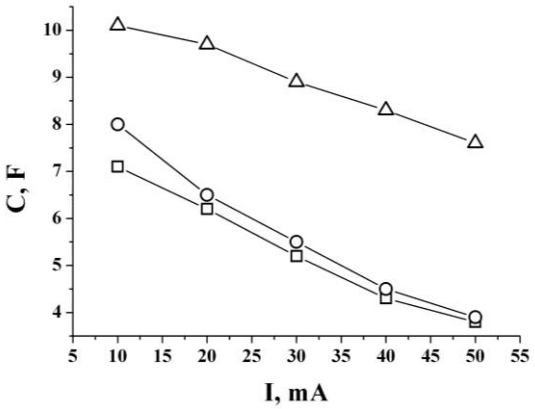

Fig. 8. Dependence of capacity of EC in 0,5M aqueous solution of Li_2SO_4 —■—, Na_2SO_4 —○— i K_2SO_4 — Δ — on discharge current

4. CONCLUSIONS

According to potential dynamic and galvanostatic studies it has been found that the specific capacity of carbon material depends on their electrochemically accessible surface area, involved in the formation of EDLC. The structure of carbon pores and molar ratio of the electrolyte are important factors that affect the value of capacity and total resistance of the electrochemical capacitor. It has been established that optimal is the use of 3M aqueous salt solution of Li_2SO_4 that provides specific capacity of carbon materials within 80-110 $F \cdot g^{-1}$ at discharge current of 10-50 mA.

We have studied electrochemical properties of PCM in 0.5 M aqueous solution of Li_2SO_4, Na_2SO_4 and K_2SO_4 which showed that the velocity of hydrated ions in the bulk electrolyte and within internal pores of the electrode of PCM increases in the order $Li^+ < Na^+ < K^+$, resulting in the improvement of PCM capacitive behavior in three electrolytes in the order $Li_2SO_4 < Na_2SO_4 < K_2SO_4$. Thus it is believed that for making a high power EC with and high energy density K^+- and Na^+-based aqueous electrolytes are more suitable than Li^+-based electrolytes. The results obtained give valuable information for further study of new hybrid supercapacitors.

The research is carried out in the framework of UKX2-9200-IF-08 with financial support from CRDF/USAID and MONMS Ukraine (M/130-2009).

REFERENCES

[1] Aurbach D., Markovsky B., Nimberger A. Electrochemical Li-insertion processes into carbons produced by milling graphitic powders: The impact of the carbons surface chemistry. *Journal of The Electrochemical Society*, **149** (2) (2002), A152-A161. doi:10.1149/1.1430715

[2] Budzyulyak I.M., Ivanichok N.J., Lisovskiy R.P., Mandzyuk V.I., Merena R.I., Rachiy B.I. The application of porous carbon material in hybrid capacitor system. Proc. of the Intern. Conf. "Ukrainian-German symposium on physic and chemistry of nanostructures and on nanobiotechnology", Beregove the Crimea, Ukraine, September 6-10, 2010, 38.

[3] Conway B.E. *Electrochemical supercapacitors. Scientific fundamentals and technological applications*. Kluwer Academic Plenum Publishers, New York, 1999.

[4] Conway B.E., Pell W. Power limitations of supercapacitor operation associated with resistance and capacitance distribution in porous electrode devices. *Journal of Power Sources*, **105** (2) (2002), 169-181. doi: 10.1016/S0378-7753(01)00936-3

[5] Kurzweil P. AC Impedance Spectroscopy – a powerful tool for the characterization of materials and electrochemical power sources. Proceedings The 12-th International Seminar on "Double Layer Capacitors and Similar Energy Storage Devices". Deerfield Beach. Florida. USA. December 9-11, 2004, 14, 18-32.

[6] Lee H.Y., Manivannan V, Goodenough J.B. Electrochemical capacitors with KCl electrolyte. *Comptes Rendus de l'Académie des Sciences - Series IIC - Chemistry*, **2** (11-12) (1999), 565-577. doi: 10.1016/S1387-1609(00)88567-9

[7] Liu H., Zhu G. The electrochemical capacitance of nanoporous carbons in aqueous and ionic liquids. *Journal of Power Sources*, **171** (2) (2007), 1054-1061. doi: 10.1016/j.jpowsour.2007.06.200

[8] Liu P., Verbrugge M.,Soukiazian S. Influence of temperature and electrolyte on the performance of activated-carbon supercapacitors. *Journal of Power Sources*, **156** (2) (2006), 712-718. doi: 10.1016/j.jpowsour.2005.05.055

[9] Ostafiychuk B.K., Budzulyak I.M., Rachiy B.I., Solovko Ya.T., Mandzyuk V.I., Lisovskiy R.P., Merena R.I., Urubkov I.V. The Structural Transformation of Nanoporous Carbon at Thermal and Chemical Modifications. *Physics and Chemistry of Solid State*, **10** (4) (2009), 803-808. (in Ukrainian)

[10] Reddy R.N., Reddy R.G. Sol–gel MnO_2 as an electrode material for electrochemical capacitors. *Journal of Power Sources*, **124** (1) (2003), 330-337. doi: 10.1016/S0378-7753(03)00600-1

[11] Vix-Guterl C., Saadallah S., Jurewicz K., Frackowiak E., Reda M., Parmentier J., Patarin J., Beguin F. Supercapacitor electrodes from new ordered porous carbon materials obtained by a templating procedure. *Materials Science and Engineering: B*, **108** (1-2) (2007), 148-155. doi: 0.1016/j.mseb.2003.10.096

[12] Wang L., Morishita T., Toyoda M., Inagaki M. Asymmetric electric double layer capacitors using carbon electrodes with different pore size distributions. *Electrochimica Acta*, **53** (2) (2007), 882-886. doi: 10.1016/j.electacta.2007.07.069

[13] Wang Y-G., Xia Y-Y. A new concept hybrid electrochemical supercapacitor: Carbon/$LiMn_2O_4$ aqueous system. *Electrochemistry Communications*, **7** (11) (2005), 1138-1142. doi: 10.1016/j.elecom.2005.08.017

[14] Xu B., Wu F., Chen R., Cao G., Chen S., Wang G., Yang Y. Room temperature molten salt as electrolyte for carbon nanotube-based electric double layer capacitors. *Journal of Power Sources*, **158** (1) (2006), 773-778. doi: 10.1016/j.jpowsour.2005.08.043

[15] Yang C.M., Kim Y.J., Endo M., Kanoh H., Yudasaka M., Iijima S., Kaneko K. Nanowindow-Regulated Specific Capacitance of Supercapacitor Electrodes of Single-Wall Carbon Nanohorns. *Journal of the American Chemical Society*, **129** (1) (2007), 20-21. doi: 10.1021/ja065501k

Address: B.K. Ostafiychuk, I.M. Budzulyak, B.I. Rachiy, L.O. Shyyko, R.P. Lisovsky, N.Ya. Ivanichok, V.M. Vashchynsky: Vasyl Stefanyk Precarpathian National University, 57, Shevchenko Str., Ivano-Frankivsk, 76025, Ukraine.

E-mail: bo@pu.if.ua; ivan-budzulyak@rambler.ru; bogdan_rachiy@ukr.net; printempsl@ukr.net; lesrom@rambler.ru; nashata@ukr.net; witalik_wash@mail.ru.

Received: 22.11.2013; **revised:** 24.03.2014

Остафійчук Б.К., Будзуляк І.М., Рачій Б.І., Шийко Л.О., Лісовський Р.П., Іванічок Н.Я., Ващинський В.М. Вплив морфології поверхні на енергетичні характеристики нанопористих вуглецевих матеріалів. *Журнал Прикарпатського університету імені Василя Стефаника*, **1** (1) (2014), 17–25.

В даній роботі досліджено вплив морфології нанопористого вуглецевого матеріалу (НВМ) на його електрохімічну поведінку у водному електроліті. Встановлена оптимальна концентрація водного розчину сульфату літію, яка забезпечує максимальні питомі енергетичні характеристики конденсаторних систем типу C/Li_2SO_4/C. Проведені порівняльні дослідження ємнісних параметрів електрохімічних конденсаторів (ЕК) у водних розчинах сульфатів літію, натрію та калію різної молярності. Циклічні вольтамперограми при різних швидкостях сканування показують, що ємнісна поведінка НВМ в трьох електролітах покращується в порядку Li_2SO_4<Na_2SO_4<K_2SO_4. Це поліпшення може головним чином бути наслідком збільшення швидкості руху гідратованих іонів в об'ємі електроліту і у внутрішніх порах НВМ в порядку Li^+<Na^+<K^+. Отримані результати дають цінну інформацію для вивчення нових гібридних суперконденсаторів.

Ключові слова: активований вуглецевий матеріал, подвійний електричний шар, електроліт, питома ємність, внутрішній опір, електрохімічний конденсатор.

Journal of Vasyl Stefanyk Precarpathian National University
http://jpnu.pu.if.ua
Vol. 1, No. 1 (2014), 27-32

UDC 542.057:538.911+54-3134
PACS numbers: 68.47.Gh, 64.70.Nd
doi: 10.15330/jpnu.1.1.27-32

RUTILE NANORODS: SYNTHESIS, STRUCTURE AND ELECTROCHEMICAL PROPERTIES

V.O. KOTSYUBYNSKY, I.F. MYRONYUK, V.L. CHELYADYN, V.V. MOKLYAK

Abstract: Nanodispersed rutile with rod-like particles was synthesized by hydrolysis of $TiCl_4$ in hydrochloric acid - ethanol alcohol aqueous solution at 40°C. It was found that the specific surface area, crystallite size, degree of agglomeration are determined by molar ratios of ethanol. The obtained material was used as the base of cathode composition for lithium power sources. The maximum values of specific capacity (250 mAh/g) at discharge in galvanostatic conditions are fixed in the case of using material with the maximum agglomeration degree and minimal particle size. Phasic character of Li^+ ions intercalation is set and the diffusion coefficient at different stages of the process is calculated.

Keywords: rutile, crystal structure, lithium intercalation, impedance spectroscopy.

1. INTRODUCTION

Using metal oxides nanodispersed forms as the cathode material is one of the most advanced ways of improving specific energy characteristics of lithium power sources. An increase of capacity for nanostructured cathode materials is caused by the improving of Li^+ ions intercalation efficiency as a result of Li^+ and electrons ions transport path lengths reduction, contact area host-material / electrolyte enlarging, specific surface area and chemical activity of cathode component growing. Crystal structure, surface morphology and electric characteristics of nanodispersed materials are determined by the peculiarities of synthesis, so the possibility of the materials formation with foreseen optimized characteristics is opening. Lithium ion intercalation degree in microcrystal rutile is negligible at room temperature and even for low current densities (C/300) it has kinetic restrictions (Hu et al., 2006). The aim of this paper is to test of nanodispersed rutile for Li-ion electrochemical insertion.

2. EXPERIMENT

Rutile TiO_2 was synthesized by hydrolysis of $TiCl_4$ in hydrochloric acid - ethanol aqueous solution at 40°C. It is known that ethanol is very important in the formation of rutile surface morphology. During the reaction at the conditions of high acidity the formation of 6-fold coordinated complex species $[Ti(OH)_nCl_m(OC_2H_5)_{6-n-m}]^{2-}$ took place where the $[OC_2H_5^-]$ served as a retarding factor for the hydrolysis of $TiCl_4$ (Wang et al., 2007). Low number of OH ligands causes the vertex-shared bonding of $[TiO_6]$ octahedra that results in the formation of a rutile phase. The obtained gel $TiO_2 \cdot H_2O$ was set to age for 3 hours at 40°C. Colloidal solution of TiO_2 was kept for 240 hours at 18°C. After segregation the

material was dried for 3 hours at 150°C. The three systems were synthesized for which the ethanol content in the reaction medium was 0, 10, 20 and 30 vol. % respectively.

3. RESULTS

Accordingly to the XRD data the system were monophase rutile (Fig. 1, Tab. 1) with rod-like particles. For all obtained materials coherent scattering regions have an ellipsoidal form with the main axis oriented along [001] crystallography direction. System №2 (ethanol content 10 vol. %) has the minimal size of coherent scattering regions (9x3 nm), for other systems these sizes are about 12x5 nm. The agglomeration degree depends on the ethanol content at synthesis (Fig. 2). Maximum is the average size of agglomerates for system №2 (500-600 nm), whereas for systems 1 and 3 the size of agglomerates is 150-200 nm. For these systems the size of individual rod-like particles is close to the size of coherent scattering regions, suggesting that their state is close to monocrystal.

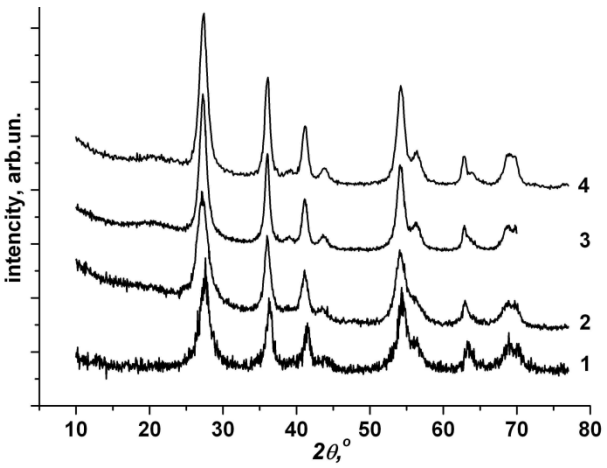

Fig. 1. XRD patterns of rutile obtained for different ethanol content (1- 0 vol. %, 2– 10 vol. %, 3– 20 vol. % 4– 30 vol. %)

System	Etanol content, vol.%	Lattice parameters		Average size of coherent scattering regions, nm	Specific surface area, m²/g	Mass loss (annealing up to 1000°C), %
		a, nm	*c*, nm			
1	0	4.6223	2.9488	12x4	165	15.8
2	10	4.6286	2.9539	9x3	77	6.7
3	20	4.6143	2.9538	12x6	90	7.7
4	30	4.6072	2.9575	12x4	106	11.4

Tab. 1. Structure and morphology characteristics of obtained rutile

The rutile particles of system 4 are weakly aggregated and have linear sizes 20-70 nm at diameter 10 nm and they are polycrystalline formations. Fixed values of specific surface area reflected changes in the morphology of obtained materials. Loss of weight at heating is explained by desorption of surface hydroxyl groups, as evidenced by fixed for all materials a clear linear dependence between mass loss and the value of specific surface area (Tab. 1).

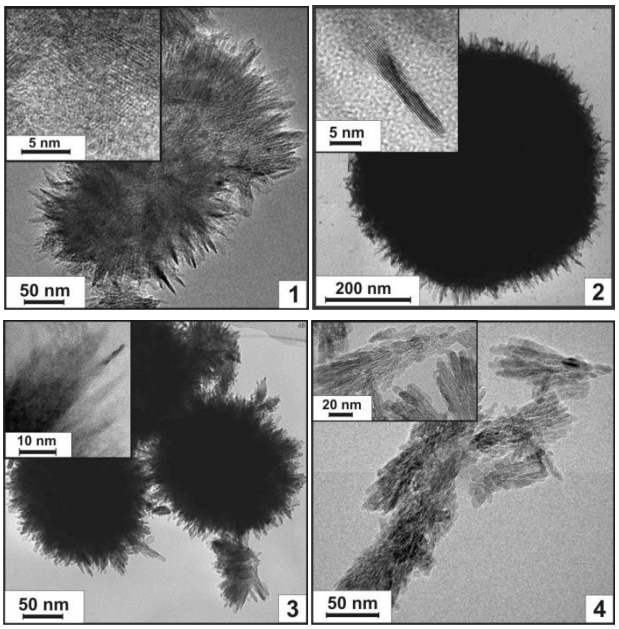

Fig. 2. TEM images of rutile synthesized for different ethanol content (1- 0 vol. %, 2– 10 vol. %, 3– 20 vol. % 4– 30 vol. %)

For checking a possible presence in the material of X-ray amorphous phases of anatase or brookite all the obtained materials were annealed for 1 h at temperatures of 400 and 600° C. Additional phases were not observed. Annealing the materials at 400°C initiated the process of particles growing with the major axis orientation been saved.

The obtained material was used as a base of the cathode for model lithium power sources (LPS). Cathode composition contains obtained rutile (90 mass %) acetylene black (8 mass %) and PVF (2 mass%). The discharge of LPS was carried out in galvanostatic conditions at current density of C/100. The kinetics of the discharge process was studied by measuring an open circuit voltage (OCV) with the use of a three-electrode scheme. Polarizing and comparison electrodes were made from lithium foil; a working electrode was nickel mesh with the pressed film of cathode composition. 1M of $LiBF_4$ γ-butyrolactone was used as an electrolyte. The degree of intercalation x was calculated as the molar amount of Li+ ions transferred through electrolyte per one mole of titanium dioxide in the cathode composition. A character of discharge curve (Fig. 3) is the result of different processes domination at different stages of discharge: intercalation into the rutile structure, formation of a double electric layer on its surface, a change of material phase composition.

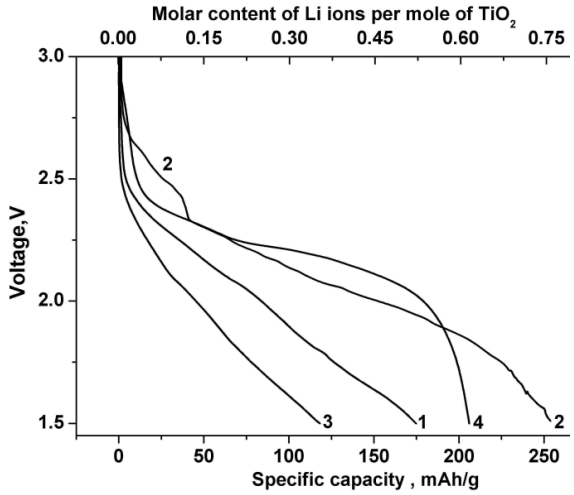

Fig. 3. The discharge curves of the LPS with the cathode based on rutile from different system

Frequency dispersion of complex impedance was studied in the range of 10^{-2}-10^{5}Hz. Based on the impedance-spectroscopic data three stages were found out, which correspond to ranges of the intercalation degree $0< x \leq 0.2$; $0.3 \leq x \leq 0.45$ and $0.55 \leq x \leq 0.75$ respectively. The first stage is characterized by a sharp decrease of the OCV caused by the Li^+ ions localization on the particle surface with the following intercalation into crystal structure. The localization of Li^+ ions is the most probable in the octahedral oxygen vacancies, as well as in the structural channels [001], and the emergence of pair interaction between intercalated lithium ions in the plain (110) can lead to the blockage of the channel and serve as a barrier to subsequent introduction. High specific surface area of the nanodispersed rutile increases the number of channels opened for Li^+ intercalation and neutralizes the influence of their blocking. The other advantage is the possibility of Li^+ ions localization in the form of the sorption layer on the surface of cathode materials. The equivalent scheme (Fig. 4) was used for fitting the Nyquist diagrams that describing the process of cathode polarization at all stages of the discharge.

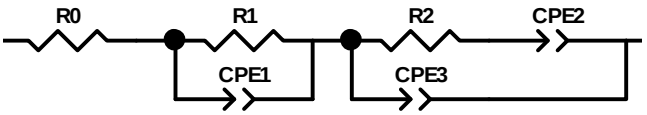

Fig. 4. Equivalent scheme used for fitting the Nyquist diagrams characterizing the process of Li^+ ions intercalation into the LPS cathode based on nanodispersed rutile

This scheme for different values of its component characteristic parameters summarizes the combination of Voigt model and adsorption model ($0 < x \leq 0.45$) and Randle's model ($x \geq 0.55$).

For the model flexibility increasing constant phase elements (CPE) were used at the equivalent scheme selection. Chain R_1–CPE_1 simulates the impedance of the Li^+ ions penetration through the TiO_2 / electrolyte interface and their diffusion in the channels and pores of the material crystal structure for the entire range of the parameter x variation. A type of elements connection (resistance and the Warburg element in parallel) corresponds to a semi-infinite diffusion in the spherical particles. Simultaneously with the intercalation of Li^+ ions in the cathode material their adsorption on the surface of rutile particles and the formation of double electric layer were carried out. This process is reflected at equivalent scheme by the chain (R_2 –CPE_2)-CPE_3. Values of exponent indexes for CPE_2 and CPE_3 are in the range of 0.96 -1.00 so these elements have the physical contents of adsorption capacity and the capacity of surface double electric layer, respectively. The analysis of changes in the values of the equivalent schemes parameters for different intercalation degree was carried out. Diffusion coefficients of Li^+ ions (Fig. 5) were calculated as described in (Liu et al., 2008).

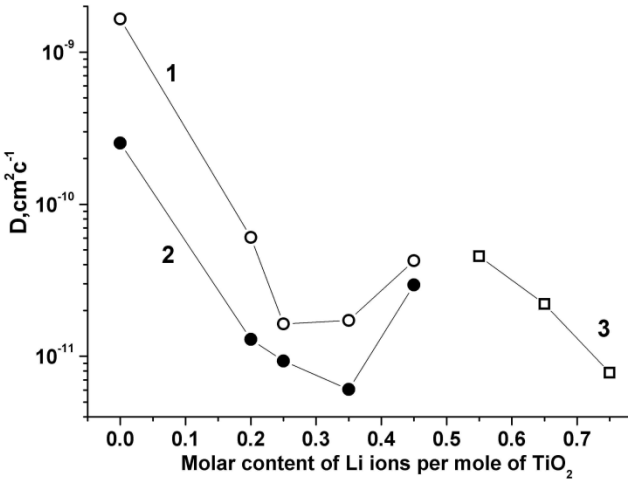

Fig. 5. The dependence of the diffusion coefficients of Li^+ ions in the cathode material based on nanodispersed rutile on the degree of intercalation

The presence of two kinetic processes with different time constants at the first stage of discharge was fixed. Calculated diffusion coefficient values decline up to x=0.3-0.35 changing from 10^{-9} to 10^{-11} cm^2/s. Electric properties of cathode was homogenized at the range $0.35 \le x \le 0.45$ and with the increasing of the rate of charge transfer process. At the final stage Li^+ ions diffusion coefficient decreases from $7 \cdot 10^{-10}$ to $2 \cdot 10^{-11}$ cm^2/s.

4. CONCLUSIONS

The possibility of rutile nanoparticles specific surface area, crystallite size, degree of agglomeration control by ethanol molar content during $TiCl_4$ hydrolysis in the hydrochloric acid-ethanol aqueous solution has been shown. It is found that the value of specific capacity of model lithium power sources with cathodes on the basis of the materials obtained depends on the size of individual particles of material and its agglomeration. The regularities of electrochemical intercalation of Li^+ in rutile nanoparticles have been studied, kinetics of the process analyzed, diffusion coefficients of the Li^+ ions calculated, the predominant role of the surface effects impact fixed.

The research described in this paper was supported by CRDF/USAID (grant UKX 2-9200-IF-08) and Ministry of Science and Education of Ukraine.

REFERENCES

[1] Hu Y.-S., Kienle L., Guo Y.-G., Maier J. High Lithium Electroactivity of Nanometer-Sized Rutile TiO_2. *Adv. Mater*., **18** (2006), 1421-1426. doi: 10.1002/adma.200502723

[2] Liu S., Zhang J., Huang K., Yu J. Improvement of Electrochemical Performance of $LiMn_2O_4$ Composite Cathode by ox-MWCNT addition for Li-ion Battery. *Braz. Chem. Soc.*, **19** (2008), 1078-1083. doi: 10.1590/S0103-50532008000600005

[3] Wang Y., Zhang L., Deng K., Chen X., Zou Z. Low Temperature Synthesis and Photocatalytic Activity of Rutile TiO_2 Nanorod Superstructures. *J. Phys. Chem.*, **111** (2007), 2709-2714. doi: 10.1021/jp066519k

Address: V.O. Kotsyubynsky, I.F. Myronyuk, V.L. Chelyadyn, V.V. Moklyak: Vasyl Stefanyk Precarpathian National University, 57, Shevchenko Str., Ivano – Frankivsk, 76025, Ukraine.
E-mail: v_kotsuybynsky@mail.ru; myrif@rambler.ru; chvl@email.ua; mvvmcv@mail.ru.
Received: 16.10.2013; **revised:** 03.02. 2014

Коцюбинський В.О., Миронюк І.Ф., Челядин В.Л., Мокляк В.В. Синтез структура та електрохімічні властивості наностержнів рутилу. *Журнал Прикарпатського університету імені Василя Стефаника*, **1** (1) (2014), 27–32.

Наночастинки рутилу стержневидної морфології отримано методом гідролізу $TiCl_4$ з застосуванням розчинів хлористоводневої кислоти та етилового спирту при температурі 40°С. Встановлено, що величина питомої площі поверхні, розмір кристалітів, ступінь їх агломерації визначається молярним вмістом етанолу в реакційному середовищі. Отримані матеріали тестувалися в якості катодного матеріалу для літієвих джерел струму. Максимальне значення питомої ємності (250 мА·год/г) при

розряді в гальваностатичних умовах зафіксовано для випадку застосування матеріалу з максимальним ступенем агломерації та мінімальним розміром частинок. Простежено перебіг інтеркаляції іонів літію в катодний матеріал на основі наночастинок рутилу стержневидної морфології та визначено значення коефіцієнтів дифузії Li^+ на різних процесах.

Ключові слова: рутил, кристалічна структура, інтеркаляція іонів літію, імпедансна спектроскопія.

Journal of Vasyl Stefanyk Precarpathian National University
http://jpnu.pu.if.ua
Vol. 1, No. 1 (2014), 33-39

UDC 541.1, 5367, 621.794
PACS numbers: 75.75.Cd, 76.80.+y
doi: 10.15330/jpnu.1.1.33-39

SYNTHESIS AND PROPERTIES OF SUPERPARAMAGNETIC $\gamma - Fe_2O_3$

V.O. KOTSYUBYNSKY, V.V. MOKLYAK, A.B. HRUBIAK

Abstract: Method of nanodispersed γ-Fe_2O_3 synthesis by thermal decomposition of iron citrate is proposed. The investigations of obtained oxides crystalline and magnetic structures are done. Nanodispersed γ-Fe_2O_3 with sizes of coherent scattering regions about 4-7 nm was is only one phase after gel sintering at 200, 250 and 300°C; the particles of synthesized materials are in a state of magnetic ordering and in superparamagnetic state. The influence of magnetic dipole interparticles interaction on parameters of Mossbauer spectra is observed. The phenomenological model of the differences between nanodispersed γ-Fe_2O_3 magnetic microstructures obtained after annealing at different temperatures is presented.

Keywords: γ-Fe_2O_3, mossbauer, superparamagnetic.

1. INTRODUCTION

The sphere of the practical use of nanodispersed iron oxide includes information store devices, magnetic sensors, controlled drag transference, separation biological objects and environment polluting substances (blue-green algae toxins). The use of iron oxide nanopowder in photocatalytic hydrogen generation devices is of great perspective.

2. EXPERIMENTAL

Nanodispersed γ-Fe_2O_3 was synthesized by a sol-gel method: slow drying (60°C) in the air of colloidal solute $Fe(NO_3)_3 \cdot 9H_2O$ and $C_6H_8O_7 \cdot H_2O$ for different molar ratio between precursors. The sedimentated iron citrate hydrate during 12-15 days was dried out in the air at 50-60°C.

Obtained xerogel was sintered at temperatures 100, 150, 200, 250, 300 °C during 1 hour. The systems of samples were investigated by X-ray diffractometry (Cu Kα radiation), Mossbauer spectroscopy (calibration relatively α-Fe), scanning electron microscopy

Sintering at the temperature of 100 and 150°C does not change an X-ray amorphous state of the material but after the sintering at the temperatures of 200, 250 and 300°C the only one X-ray crystal phase in the material is γ-Fe_2O_3 with lattice parameter a =0.83388±0.00015 nm (Fig. 1).

Halos on the XRD patterns are caused by the presence in the samples of X-ray amorphous component.

Average sizes of X-ray coherent scattering areas (CSA) after sintering at temperature of 200°C is 5±1nm and after sintering at 250 and 300°C is about 6±1 nm.

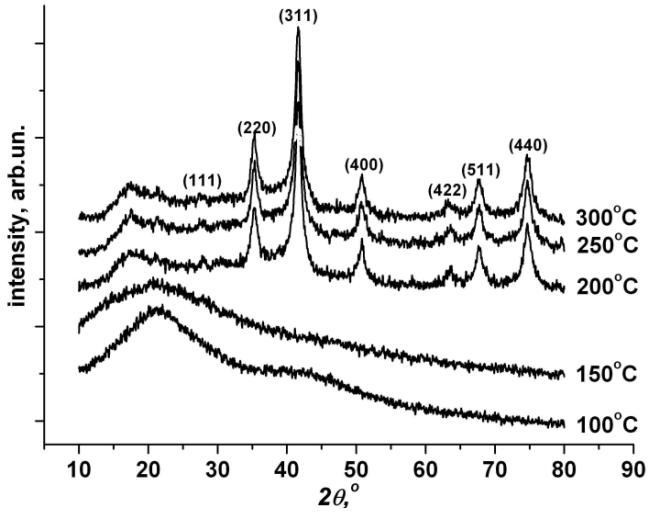

Fig. 1. X-ray diffraction patterns of γ-Fe_2O_3 samples obtained at the different sintering temperatures

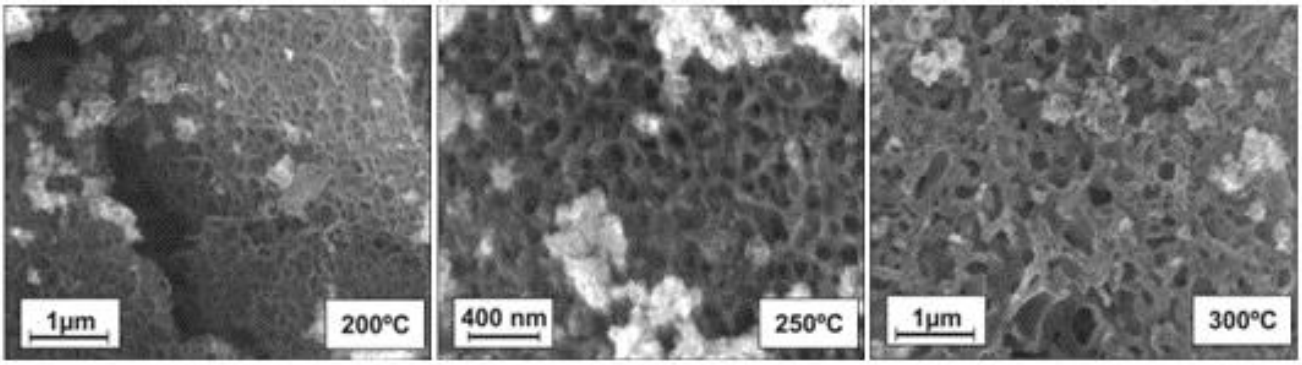

Fig. 2. SEM images of γ-Fe_2O_3 samples obtained at the different sintering temperatures

Accordingly to scanning electron microscopy data all materials obtained by sintering during 1 hour at 200, 250 and 300°C are characterized by porous structures as a result of evaporation of metal-organic precursor decomposition products (Fig. 2).

Mossbauer spectroscopy gave an independent information about phase composition, magnetic microstructure, iron ions valence. At the conditions of partially disordered magnetic system (samples sintered at 200, 250 and 300°C) it was impossible to establish the responsibility between each partial component of Mossbauer spectra and some type of ^{57}Fe magnetic neighborhood. So, we used the suggestion about the formation in these cases non-interrupted distribution of hyperfine magnetic field on the ^{57}Fe nucleus in the γ-Fe_2O_3 structure.based on the methods [2].

3. RESULTS AND DISCUSSION

Mossbauer spectra synthesized materials with the deconvolution on the partial components are presented in the Fig. 3 and 4, generalization of it parameters – in Tab. 1.

Sintering at the 100°C does not cause any substantial changes in the crystal and magnetic microstructure of the origin sample The values of isomeric shift (δ=0.41 mm/s) and quadrupole splitting (Δ=0.50-0.56 mm/s) for doublet component of the origin and sintered at 100°C samples (Fig. 3) are different form the data for iron citrate [8] and are close to the results in the report [3], where the super-paramagnetic (SP) particles γ-Fe_2O_3 with the diameter <10 nm in polymeric matrix are studied

Sample	H, kOe	δ_s, mm/s	Δ_s, mm/s	ω, mm/s	S, %
Origin xerogel	–	0.41	0.55	0.35	100
100°C	–	0.41	0.57	0.37	100
150 °C	–	0.53	0.81	0.34	49.3
	–	0.52	1.33	0.40	43.8
	–	1.37	2.19	0.30	6.9
200 °C	–	0.48	0.80	0.45	27.7
	–	0.48	1.32	0.45	15.1
	–	0.46	-0.08	3.61	21.6
	429.10*	0.44	-0.03	0.43	35.6
250 °C 1 hour	–	0.47	0.73	0.43	18.0
	–	0.47	1.25	0.49	13.6
	–	0.53	0.01	4.20	24.2
	439.50*	0.45	-0.01	0.37	44.1
250 °C 3 hour	–	0.35	0.75	0.38	19.7
	–	0.33	1.20	0.63	80.2
300 °C	–	0.48	0.74	0.40	36.9
	–	0.47	1.24	0.51	43.0
	412.00*	0.48	-0.09	0.36	20.1

*for materials, obtained sintering at 200, 250 and 300°C average most probably values of hyperfine magnetic field H are presented

Tab. 1. Parameters of Mossbauer Spectra for Synthesized Materials

Annealing at 150°C causes an increase of δ and Δ values and spectra is a superposition of the three partial components (Fig. 4). The two doublet components have the isomeric shift 0.52-0.53 mm/s and Δ 0.80 and 1.32 mm/s, respectively, and correspondence to resonance absorption by the nucleus of tetrahedral coordinated ions Fe^{3+} in the highspin state.

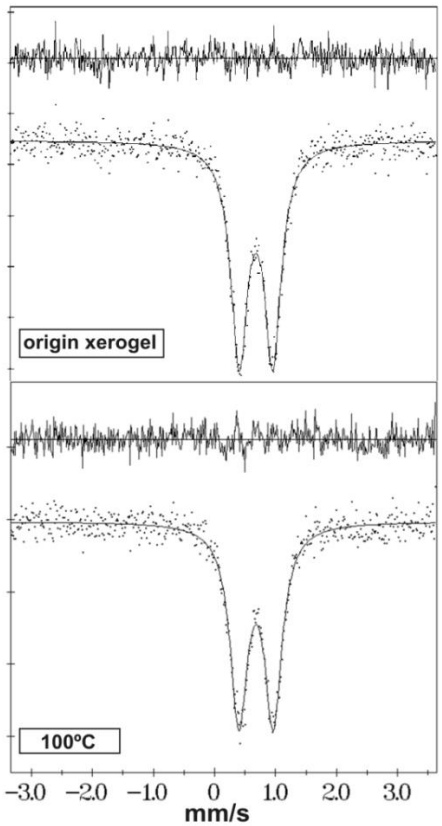

Fig. 3. Mossbauer spectra of synthesized materials: origin xerogel before and after sintering at 100°C during 1 hour

The values of quadrupole splitting depend on the lattice deformation under the Laplace preassure. The third doublet with δ=1.37 mm/s and Δ=2.19 mm/s is formed as a result of resonance absorption by nucleus of Fe^{2+} ions.

Magnetic ordered components of Mossbauer spectra for materials obtained sintering at 200 and 250°C are 35.6 and 44.1% of integral intensity responsively that reflect the particles enlarging with temperature increase. A function of hyperfine field distribution is characterized by one maximum at about 490 kOe. Paramagnetic parts of the spectra contain two components which response to the resonance absorption by ^{57}Fe nucleus in the superficial and inner regions of mesoporous γ-Fe_2O_3 3D-grid. The tendency to decreasing δ and Δ is caused by particle (domain) enlarging and increasing of covalence degree of Fe-O bonds. The presence of wide doublet component with Δ≈0 is the characteristic peculiarity of these spectra. Similar spectra content was observed for iron oxide nanoclasters obtained by ferric oxalate thermal decomposition in [7].

In the spectra of a sample sintered at the 300°C DC with Δ = 0 is absent, a magnetically ordered part does not exceed 20% of integral intensity with the saving of two component composition of the central doublet .

Values of δ and Δ for the materials obtained by sintering at 200, 250 and 300°C are lower as compared to the data for microcrystal γ-Fe_2O_3 [6]. It is caused by attenuation of the superexchange interaction as a result of an increase of the amount of ^{57}Fe nucleus with destroyed bonds (Fig. 2).

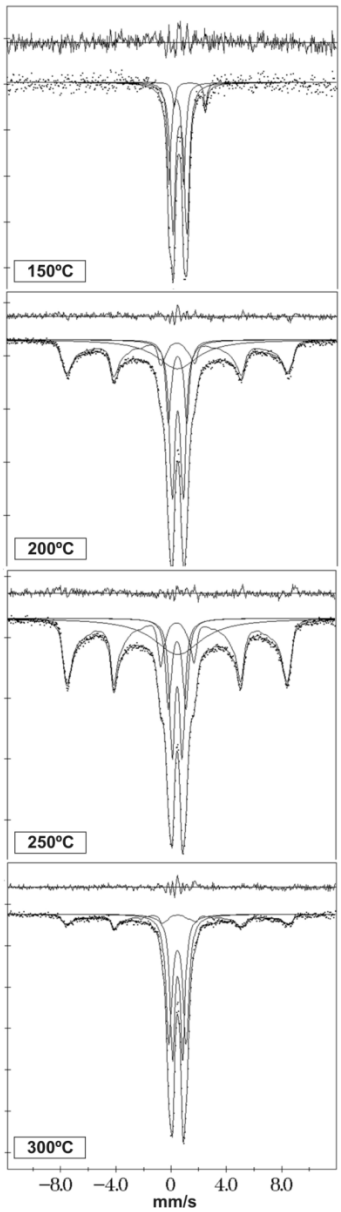

Fig. 4. Mossbauer spectra of materials obtained by sintering at 150, 200, 250 and 300°C during 1 hour

The changes of magnetic microstructures of synthesized material are caused by sizes effects and SP phenomena. The obtained materials are the systems of monodomain clusters with fluctuated magnetic moments This fluctuations cause the broadening of spectra lines and disappearance of magnetic hyperfine structure at a certain value of material magnetic anisotropy which determine the relaxation time τ_r of particle magnetic moment. Relaxation time is calculated as $\tau_r = \tau_0 \exp\left(\frac{KV}{kT}\right)$, where $\tau_r \approx 10^{-9} - 10^{-10} e$, V – particle volume, K – constant of anisotropy, T – temperature. For a particle with the certain values K and V the conversion from superparamagnetic to magnetically ordered state is occurred at the blocking temperature (T_B). For the system of magnetic nanoparticles the variant of magnetic interaction energy (sum of exchange and dipole energies) between two neighbors particles dominance up to anisotropy energy became possible [4]. Influence of exchanged effects on the macroscopic magnetic characteristics of materials is reflected in the appearance of magnetic nanomaterials peculiarities similar to the characteristics of spin glass, the appearance of blocking temperature shift, disagreement of structural and magnetic researches data. Transitions are stimulated by defects, cluster interactions, strains on the interphases boundaries which is typical for nanoclusters system. Oscillation blocking takes place at the effective temperature $T_{ef}=T_B+T^*$ where temperature shift T^* reflects influence of dipole-dipole interaction and determines the value of it energy. Activation of interaction effects will be determined by a module of difference between T_{ef} and temperature of magnetic moment oscillation blocking. Wide doublet component components in the spectra of samples obtained by sintering at 200 and 250 are an intermediate stage between magnetically ordered and SP state of particle in the case of strong dipole-interaction. These systems show SP properties at temperatures higher than TB. At temperatures lower TB these systems are like spin glass and its spectra contains broad doublet. This component is a result of resonance absorption by the ^{57}Fe nucleus for which hyperfine field has the value between a zero and saturation level. Thermal fluctuation of magnetic moment of particles take place however the "temporary hangings up" are possible.

Constant of magnetic anisotropy for the particles of γ-Fe_2O_3 (d≈6.5 nm) is $K=1.2\cdot10^6$ J/m^3 [1]. There are another values $K=(2.1\pm0.3)\cdot10^5$ J/m^3 for γ-Fe_2O_3 particle with size 10 nm [8]. For value $K=5\cdot10^5$ J/m^3 it is obtained that at the T=290 K in SP state there are particles with the sizes less than 4.2-4.8 nm that corresponds to X-ray analysis data.

With sintering at 250°C an increase of treatment time to 3 hours causes the disappearance of magnetic ordered component of Mossbauer spectra. Accordingly to XRD data this sample is amorphous. So, structural and magnetic properties of obtained materials depend on thermal treatment conditions.

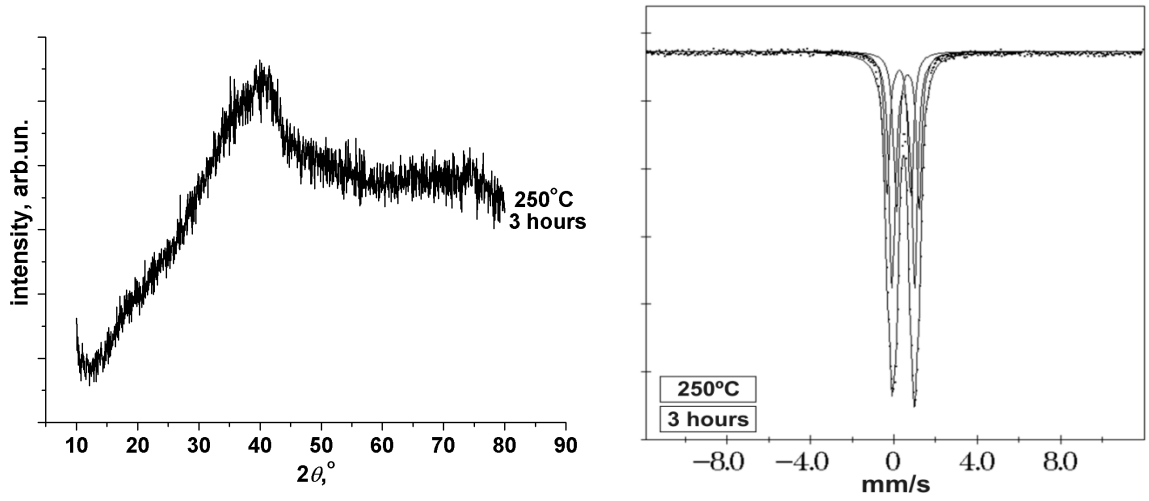

(a) *(b)*

Fig. 5. XRD pattern (a) and Mossbauer spectra (b) of materials obtained by sintering at 250°C during 3 hour

Doublet component characteristic parameters-based comparative analysis of the systems sintered at 250°C during 1 and 3 hours we can take a conclusion about an increase of Fe-O bonding covalence degree without magnetic neighborhood changes.

4. CONCLUSIONS

Generalizing of the experimental data we can build a phenomenological model. As a result of thermal destruction of origin xerogel in the material amorphous regions of γ-Fe_2O_3 phase are nucleated. After sintering at 200°C it is partially crystallized with the forming of mesoporous 3D-grid as the result of NO_2, CO_2 and H_2O evaporation. Particle size distribution causes the coexisting of magnetic ordered and superparamagnetic state of a different part of the grid. Sintering temperature increase (up to 250 and 300°C) leads to the intensification of these processes with an increase of pore sizes and chain thickness. Interparticle dipole-dipole magnetic interaction has been fixed for the materials obtained by xerogel sintering at 200 and 250°C. Sintering at 250°C during 3 hours lead to full dehydration of the material with the bridges destroyed between particles and fragmentation of grid structure with the formation of paramagnetic amorphous product.

This work was supported in part by the CRDF / USAID Grant UKX 2-9200-IF-08

REFERENCES

[1] Coey I.M., Khalafalla D. Superparamagnetic γ-Fe_2O_3. *Phys. State Solids*, **11** (1) (1972), 229–239. doi: 10.1002/pssa.2210110125

[2] Hesse J., Rübartsch A. Model independent evaluation of overlapped Mössbauer spectra. *J. Phys. E: Sci. Instrum.*, **7** (1974), 526−532. doi: 10.1088/0022-3735/7/7/012

[3] Malini K.A., Anantharaman M.R., Gupta A. Low temperature Mossbauer studies on magnetic nanocomposites. *Bull. Mater. Sci. (Indian Academy of Sciences)*, **27** (4) (2004), 361–366. doi: 10.1007/BF02704773

[4] Morup S., Topsoe H., Clausen B.S. Magnetic properties of microcrystals studied by Mossbauer spectroscopy. *Phys. Scr*., **25** (1982), 713-719. doi: 10.1088/0031-8949/25/6A/015

[5] Predoi D., Kuncser V., Filoti G. Magnetic Behaviour Of Maghemite Nanoparticles Studied By Mössbauer Spectroscopy. *Romanian Reports in Physics*, **56** (3) (2004), 373–378.

[6] Serna C.J., Morales M.P. Maghemite: A Versatile Magnetic Colloidal Material. *Surf. Coll. Science*, **17** (2004), 27-63. doi: 10.1007/978-1-4419-9122-5_2

[7] Suzdalev I.P., Maksimov Yu.V., Imshennic V.K. at al Hierarchy structure and magnetic properties of nanodispersed iron oxides. *Russian Nanotechnologies*, **1** (1-2) (2006), 134-141. (in Russian)

[8] Takashima Y., Tateishi Y. Mössbauer Spectra of Various Organic Iron Chelates. *Bull. Chem. Soc. Jpn.*, **38** (10) (1965), 1688-1693. doi: 10.1246/bcsj.38.1688

Address: V.O. Kotsyubynsky, V.V. Moklyak, A.B. Hrubiak: Vasyl Stefanyk Precarpathian National University, 57, Shevchenko Str., Ivano – Frankivsk, 76025, Ukraine.

E-mail: v_kotsuybynsky@mail.ru; mvvmcv@rambler.ru; andrii_grubiak@mail.ru.

Received: 14.10.2013; **revised:** 19.03.2014

Коцюбинський В.О., Мокляк В.В., Груб'як А.Б. Синтез та властивості суперпарамагнітного γ-Fe_2O_3. *Журнал Прикарпатського університету імені Василя Стефаника*, **1** (1) (2014), 33–39.

Запропоновано спосіб одержання нанодисперсного γ-Fe_2O_3 шляхом термічного розкладу цитрату заліза. Проведено комплексні дослідження кристалічної та магнітної мікроструктури отриманого оксиду заліза. Виявлено, що після відпалу при температурі 200, 250 та 300 °С єдиною рентгенокристалічною фазою в матеріалі є нанодисперсний γ-Fe_2O_3 з розміром областей когерентного розсіювання 4-7 нм , частинки якого перебувають в магнітовпорядкованому та в суперпарамагнітному станах. Спостерігався вплив магнітної дипольної міжчастинкової взаємодії на параметри месбауерівських спектрів отриманих матеріалів. Пропонується модель, що пояснює відмінності магнітної мікроструктури нанодисперсного γ-Fe_2O_3, отриманого після відпалу при різних температурах.

Ключові слова: γ-Fe_2O_3 , магнітні наноматеріали, суперпарамагнетизм, месбауерівська спектроскопія.

Journal of Vasyl Stefanyk Precarpathian National University
http://jpnu.pu.if.ua
Vol. 1, No. 1 (2014), 41-53

UDC 531.731.43
PACS numbers: 61.43.Gt, 82.45.Jn, 84.60.Ve
doi: 10.15330/jpnu.1.1.41-53

THE EFFECT OF THERMAL MODIFICATION ON THE DEVELOPMENT OF CARBON MATERIAL MICROPOROUS STRUCTURE

B.K. OSTAFIYCHUK, I.M. BUDZULYAK, N.YA. IVANICHOK, B.I. RACHIY, R.P. LISOVSKY

Abstract: A research is done to characterize the microporous structure of outgoing and thermally modified (673 K, 180 min) plant-extracted carbon material. The porous system characteristics are worked out by different methods on low temperature (77K) N_2 adsorption-desorption based isotherm. It is stated that thermal modification contributes to the enlargement of specific surface (from 361 m^2/g to 673 m^2/g), an increase in total pore volume (from 0,166 cm^3/g to 0,477 cm^3/g) and an increase in micropore volume (from 0,127 cm^3/g to 0,173 cm^3/g). Most effectively thermal modification is apt to form nanopores with diameters of 0,75; 1,25 and 4 nm.

Keywords: porous carbon material, thermal modification, low temperature porometry, structural and adsorptive characteristics.

1. INTRODUCTION

Porous carbon material (PCM) possesses unique physical and mechanical properties and is widely used – from nanoelectronics and supercapacitors to composite material [26, 5]. Providing carbon material with necessary electrical and physical properties, apart from those which are defining for the material-based electrochemical capacitors, is carried out both in the course of its obtaining and by way of chemical and thermal treatment of carbonized material [4]. Traditional raw materials for the production of quality PCM is hardwood, fruit seeds, coconut peel, coal, and resins with high- content coal and natural micro- and mesoporosity [10].

From the point of view of its practical use the conspicuous characteristics PCM are internal pore volume, the specific surface and volume of micropores.The simplest and most reliable method of measuring these characteristics is gas sorption. Gas sorption measurement is easy to install and use.

The goal of figuring out the specifics of application of N_2 adsorption- desorption to characteristics of PCM porous structure is to assess the impact of its thermal characteristic versions to the carbon material, obtained from apricot pits; and to analyze applicability of different methods of calculation for the characteristics of carbon material porous structure.

2. EXPERIMENT AND DISCUSSION

The object of research is the process of forming carbon material porous structure in the course of its obtaining and further thermal modification. The subject of research is the PCM, obtained by

hydrothermal carbonization of apricot pits-extracted material under the pressure of water vapour (12-15)·10^5 Pa. The temperature range of carbonization activation totalled 873-1273 K. Thermal activation is carried out 3 h at temperature 673 ± 3 K that leads to obtaining the samples, the symbols being listed in Tab. 1.

Temperature carbonating activation, K	**Samples after carbonation activation**	**Samples after thermal activation at 673 K**
873	*CA- 1*	*CTA - 1*
973	*CA - 2*	*CTA - 2*
1073	*CA - 3*	*CTA - 3*
1173	*CA - 4*	*CTA - 4*
1273	*CA - 5*	*CTA - 5*

Tab. 1. Marking of PCM samples

A microscopic research is done by means of the e- microscope Zeiss Supra 40 VP (Carl Zeiss Group Germany) with a field cathode (Field Emission), e-microscope GEMINI and a fully oil-free vacuum system with the mode of operation on low vacuum (VP).

Determination of PCM structural and adsorptive characteristic is carried out by means of Ni sorption at temperature T = 77 K on the automatic sorptometer Quantachrome Autosorb (Nova 2200 e). The samples have been degased at 453 K during 20 hours.

The following methods are employed to calculate the parameters of CA and CTA porous structure : 1) proposed by Brunauer, Emmett, Teller [3] BET method in boxes, with a limited range of relative pressure P/P_0 = 0.05-0.035; 2) the method of Langmuir (method L) [13], which is based on the assumption that the adsorbent saturation limit corresponds to the formation of a monolayer of nitrogen, and 3) the method of BJH, proposed by Barret, Joyner and Halenda [1], and 4) the method of DH, the proposed Dollimore and Heal [7]; 5) t-method [6] and its modification MR method [21] to determine the micropore size distribution; 6) α_s-method [11]; 7) the method of DR- method [8]; 8) HK-method proposed by Horvath and Kawazoe, which calculates the size of the region of small micropores relative pressure adsorption isotherm and is designed for materials, which is dominated by slit-like pores [12]; 9) method SF, developed by Saito and Foley for cylindrical micropores [27]; 10) method DFT (Density functional Theory), which is based on density functional theory [9].

Here are the parameters that characterize carbon material porous structure: S (m^2/g) – specific surface volume; V_Σ (cm^3/g) – the total volume calculated by the volume of adsorbed nitrogen at. P/P_0>0,995; the volume of micropores V_m (cm^3/g) is calculated by a t-method, external surface area S_{ext} (m^2/g) and micropore surface S_m (m^2/g) by the formula $S_m = S_{BET} - S_{ext}$; d (nm) – an average diameter or width of the pores.

In the study of PCM structural properties important is the shape and size of micro- and nanopores formed in the material as a result of technological operations in the course of their obtaining and further treatment. In Fig. 1 is a SEM-image of BK-3 carbon material surface at different scales. When considering the PCM surface (Fig. 1) one can see surface microgaps, round and oval transport pores, which in most cases are filled with fragments of coal fractures. The entire surface observes white inclusions which are the main source of metal, oxygen , and the remnants of burnt cinder [24].

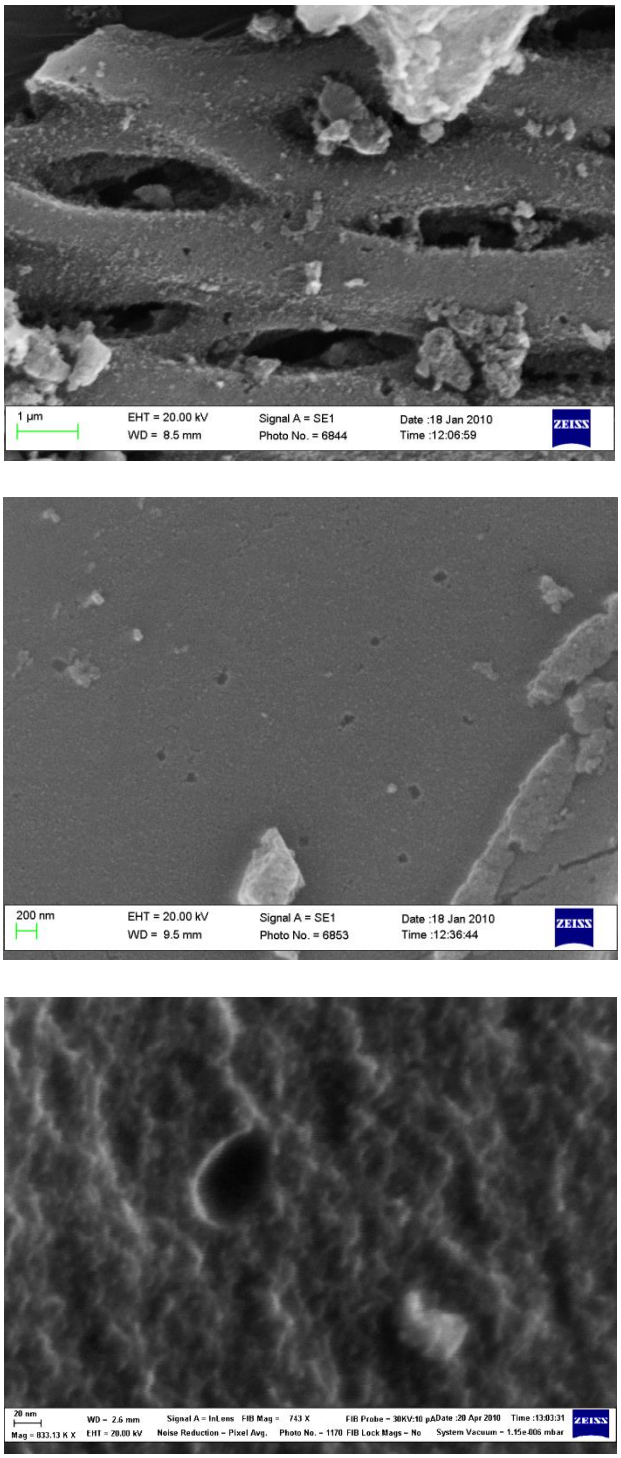

Fig. 1. The microstructure of the surface of carbonated PCM

For uncovering internal pores and making new ones thermal activation of carbonized carbon material is done at temperature (673 K, 180 min), followed by the opening of porous structure (Fig. 2) which has been invisible before treatment in contrast to the outgoing material surface with separate outputs of pores. The reason for this structure is that organic substance of the material surface is burned in the course of obtaining carbon from a plant-extracted material, but the remnants rise along the channels (pores) from grains onto the surface under vapour pressure. Thus, thermal activation makes it possible to cleanse coal surface from organic and adsorbed remnants that result in new pores and an increase of porosity.

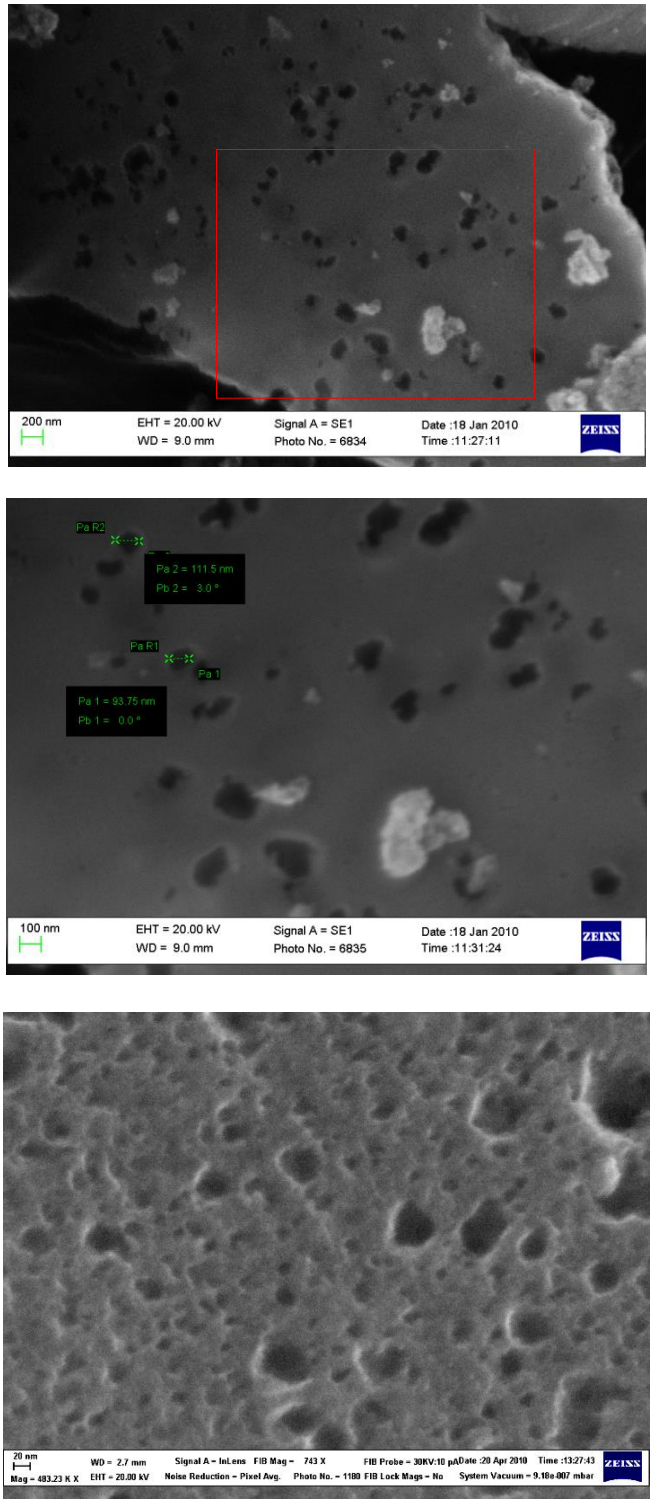

Fig. 2. SEM-surface image of CTA-3 samples

Fig. 3 shows typical isotherms of N_2 adsorption for CA-3 and CTA-3 samples which belong to the isotherms of type II and can be observed in polymolecular adsorption [20]. It is hysteresis that is observed in CTA-3 samples (type H4 by IUPAC classification [11]) which is usually associated with capillary condensation in mesopores. The point of branching adsorption and desorption curve is observed at $p/p_0 \approx 0.42$, where p and p_0 – vapour pressure of N_2 adsorbate and pressure of its saturated pore at 77 K, respectively. Hysteresis as wells as another phenomenon can be observed in CA-3 samples which is manifested as the discrepancy between the branches of adsorption and desorption in a relatively low pressure and is called the hysteresis of low pressure. There are several possible reasons

for its manifestation: swelling of spatial highly molecular frame of adsorbent, permanent retention of adsorbent molecules in pores, the size of which is close to adsorbate molecules; permanent chemical interaction of adsorbate and adsorbent [11].

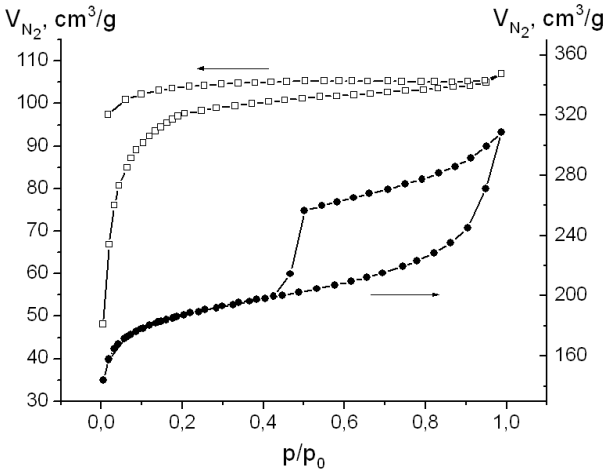

Fig. 3. Isotherms of N_2 sorption (77 K) for CA-3 (–□–) and CTA-3 (–●–)

As the isotherms of carbonized PCM adsorption -desorption samples (samples CA) are similar, they are not shown in this work.

Fig. 4 shows the isotherms of carbon material N_2 adsorption after its thermal activation (samples CTA). For all the samples the isotherms belong to those that are characterized by the presence of hysteresis loops. The analysis of the isotherms makes it possible to trace the impact of thermal activation on the development of activated carbon porous structure.

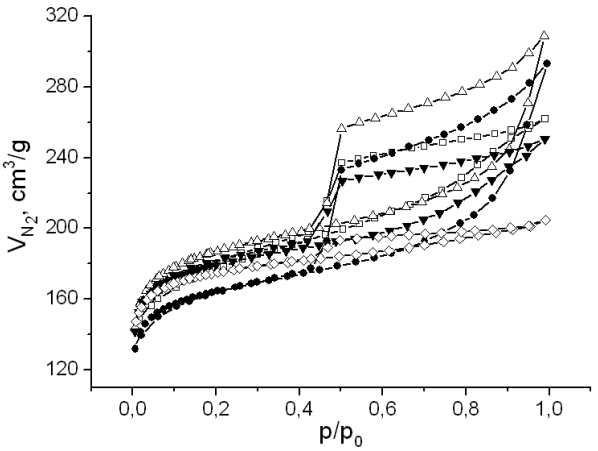

Fig. 4. A N_2 sorption isotherm (77) for thermally modified PCM: –□– CTA-1; –●– CTA-2; – Δ – CTA-3; –▼– CTA-4; –◊– CTA-5

As a quantitative measure of hysteresis (ΔV_H) the difference of N_2 adsorbed volume is taken from isotherms of desorption (V_{de}) and adsorption (V_{ad}) at $p/p_0 = 0.7$: $\Delta V_H = V_{de} - V_{ad}$. Estimates of low pressure hysteresis (ΔV_{LPH}) held at $p/p_0 = 0.2$: $\Delta V_{LPH} = V_{de} - V_{ad}$.

In Fig. 5 is the dependence of hysteresis temperature on PCM temperature obtained. It can be seen in the Figure that carbonized coal material structural properties responsible for hysteresis phenomenon all over the range of temperatures, and in the interval 973-1073 K do not substantially change ($\Delta V_{LPH} \approx 6$ cm^3/g, $\Delta V_H \approx 3$ cm^3/g). Hysteresis in low pressure for CTA samples is actually not manifested, and values of ΔV_{LPH} are to close to nil. Hysteresis in high relative pressure ($p/p_0 = 0.42$-1.0) is manifested for all the samples, but value ΔV_H for CTA samples is lower than for CA samples.

Besides, the ΔV_H parameter for CTA samples rapidly changes with a temperature rise maximum at ~973 K that testifies to the maximum development of mesopores at this temperature (Tab. 2).

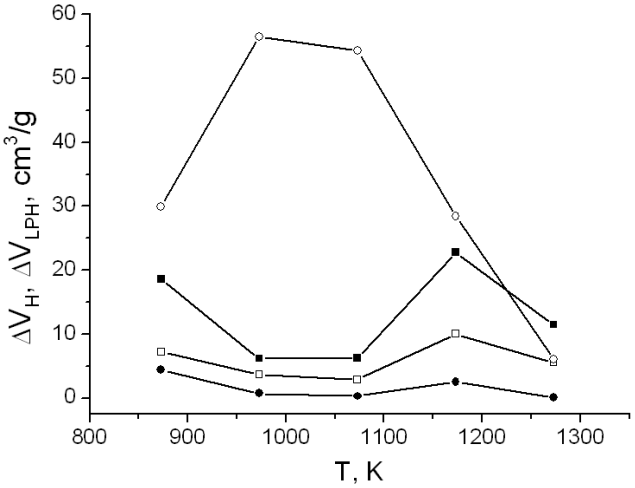

Fig. 5. Dependence of hysteresis effect for PCM on obtained temperature: ΔV_{LPH} for CA (–■–); ΔV_H for CA (–□–); ΔV_{LPH} for CTA (–●–); ΔV_H for CTA (–○–)

As is seen in Tab.2, with temperature rise up to 1073 K the specific surface of S_{BET} increases both for CA samples and CTA ones and reaches 673 m^2/g (*CTA-3*). At this value of specific surface of micropores S_{micro} equals 406 m^2/g and their relative V_{micro}/V_Σ content makes up 36% of the total volume of pores. For thermally activated material obtained at temperatures 1173-1273 K, the specific surface of S_{BET} decreases to 626 m^2/g.

Parameters	Sample	Temperature, K				
		873 *(1)*	973 *(2)*	1073 *(3)*	1173 *(4)*	1273 *(5)*
S_{BET}, m^2/g	*CA*	337	342	361	206	46
	CTA	535	592	673	646	626
S_{micro}, m^2/g	*CA*	274	271	314	131	31
	CTA	307	327	406	460	535
S_{meso}, m^2/g	*CA*	83	42	43	75	15
	CTA	228	265	261	186	91
V_Σ, cm^3/g	*CA*	0.186	0.149	0.166	0.122	0.033
	CTA	0.405	0.454	0.477	0.388	0.317
V_{micro}, cm^3/g	*CA*	0.114	0.112	0.127	0.056	0.016
	CTA	0.176	0.137	0.173	0.195	0.227
V_{micro}/V_Σ, %	*CA*	61	75	77	46	49
	CTA	44	30	36	50	71

Tab. 2. Parameters of carbon material porous structure

In Fig. 6 is the distribution of pores by the size for CTA samples calculated in the therms of desorption with the BJH method. The distribution curves show that for all the thermo modified samples the major share in the total volume of pores is made up of pores with the radius 1.8-2.0 nm.

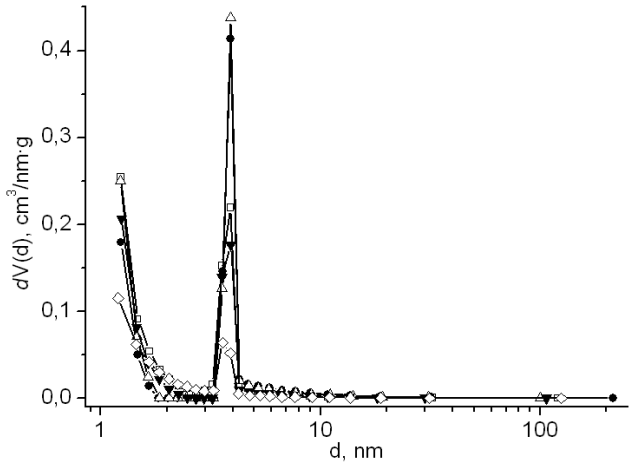

Fig. 6. The distribution of pore volume by the size for thermally activated PCM: –□– CTA-1; –●– CTA-2; – Δ – CTA-3; –▼– CTA-4; –◊– CTA-5

For these studies, to compare the parameters of porous structure and their influence on the specific characteristics of PCM have been selected samples of CA-3 and CTA-3.

The outgoing experimental basis for all theoretical calculations and interpretation is a sorption isotherm (Fig. 3) of samples of a given mass, i.e. the dependence of the number of evenly sorbed by the sample N_2 (under normal conditions) on the relative pressure of gaseous N_2 p/p_0. The characteristics of carbon material porous structure are defined by these isotherms, the values of which are calculated through different methods (Tab. 3).

Parameter	**PCM**	**Method of calculation**									
		BET	L	BJH	DH	t–method	α_s–method	DR	DA	HK	SF
S, m^2/g	*CA-3*	361	442	–	–	–	–	–	–	–	–
	CTA-3	673	829	–	–	–	–	–	–	–	–
S_{micro}, m^2/g	*CA-3*	–	–	–	–	318	–	452	–	–	–
	CTA-3	–	–	–	–	413	–	835	–	–	–
S_{ext}, m^2/g	*CA-3*	–	–	1.98	2.16	43.1	–	–	–	–	–
	CTA-3	–	–	232	237	261	–	–	–	–	–
V_Σ, cm^3/g	*CA-3*	0.166	–	0.005	0.005	–	–	–	–	–	–
	CTA-3	0.477	–	0.286	0.279	–	–	–	–	–	–
V_{micro}, cm^3/g	*CA-3*	–	–	–	–	0.127	0.130	0.161	0.162	0.148	0.148
	CTA-3	–	–	–	–	0.173	0.188	0.297	0.322	0.284	0.285
V_{micro}/V_Σ, %	*CA-3*	–	–	–	–	77	78	97	98	89	89
	CTA-3	–	–	–	–	36	39	62	68	60	60
d, nm	*CA-3*	1.84	–	3.22	3.22	–	–	2.55	1.74	0.37	0.45
	CTA-3	2.84	–	3.89	3.89	–	–	1.86	1.22	0.37	0.45

Tab. 3. The parameters of porous structure in CA and CTA samples, calculated by different methods

The specific surface area of S calculated by means of multipoint BET in the linear schedule of dependence $1/[W(p_0/p)-1]$ on p_0/p in the range of an adsorption isotherm for the relationship p_0/p within 0.05-0.35 equals 361 m^2/g and 673 m^2/g for CA-3 and CTA-3 samples, respectively. In CTA-3 sample the magnitude of the surface area and the total volume of pores is about 3 times greater than the corresponding values CTA-3 (0.477 cm^3/g and 0.166 cm^3/g, calculated under $p/p_0 = 0.99$ in assumption

that all the pores have been filled with liquid adsorbate). From the data obtained one can conclude that the porous structure of CTA-3 is developed better than that of CA-3.

The researches [14, 19, 22, 23] read that it is incorrect to apply the BET method for the study of microporous samples as its use is limited while defining the specific surface of pores of the sample under study, micropores are taken out of account.This is why in commercial devices (Autosorb-type and other analogues) L-, DR-, t-, and α_s-methods are widely used in the investigation of micropore-content objects, in particular, in defining the surface area of microporous material the L-method is applied which in contrast to the BET method gives for CA-3 and CTA-3 samples higher values of the specific area of surface (~440 m^2/g and 820 m^2/g , respectively).

To assess the volume of micropores in the presence of meso-, and macropores the t-method is oftener applied, in which the outgoing sorption isotherm is rebuilt as the function of a new variable t. The latter value is called the statistical thickness of the adsorption film and is determined by the following expression: $t = (W/W_{mono})\sigma$, where W – amount of adsorbed vapor, depending on the relative pressure p/p_0; W_{mono} – the capacity of a monolayer on the surface of the sample; σ –monomolecular thickness adsorption film (for nitrogen at T = 77 K is assumed to be 0.354 nm [11]). Calculated like this values for t. are a good match even to the samples different by the chemical nature of the surface [17, 18]. For carbon adsorbents, first of all, soot, the authors [18] recommend to make use of an equation for the statistical thickness of adsorbed film proposed in ASTM D-6556-01 [28] standards.

For microporous samples a dependence plot of the volume of gas absorbed in normal conditions on t is a straight line which cuts off the segment of the vertical axis for calculation of micropore volume V_{micro}. According to the slope of the line calculated value of the external specific surface area of the sample S_{ext} (Fig. 7).

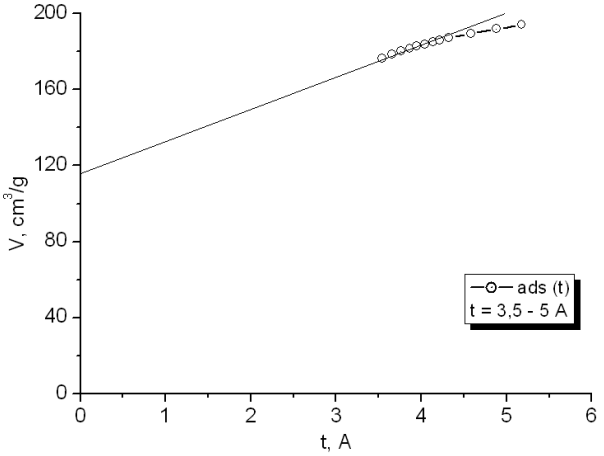

Fig. 7. t-method for N_2 adsorption in CTA-3 sample

The volume filling of micropores is completely neglected in the theory of t-method, as it is assumed that it happens at considerably smaller relative pressures of gaseous N_2 on condition the statistical thickness of adsorptive layer remains small. To check the correctness of applying the t-method, the data obtained are compared with the results received from α_s -method, and the DR-method which is based on the theory of volume filling of micropores [8].

The comparison of different methods for porous structure parameters is carried out for thermally activated carbon CTA-3 sample. Defined by BET-, DR-, DFT- and t-methods the specific surface values are pretty close and are in the interval S = 609-674 m^2/g, which means these methods can be applied for defining the surface area of plant-extracted activated carbon.

There is a good for microporous materials co-ordination of the parameters of standard t-method with BET-method that has also been observed for CTA-3 sample under study,for one of the known ways to define external surfaces in microporous samples lies in the initial filling of some substance with the following definition of the sample specific surface by BET-method [11]. Quite different are the results obtained after correction of sorption isotherms on the volume of micropores calvulated according to DR-method. These isotherms by the shape markedly deviate from classical, and BET is not

a straight line in the coordinates; and the values of specific surface differ considerably (Tab. 3) from the values of external specific surface defined by the t-method or BET-method.

The values of specific area defined by BJH- and DH methods are smaller because a micropore area is not counted in calculation and the methods are used in defining the volume of meso- and macropores with their distribution by the size.

A similar pattern is observed when determining the total volume of pores and the volume of micropores. BJH-,and DH methods give a lower value V_Σ (0.286-0.279 cm^3/g), than the value of the total pore volume calculated at $p/p_0 = 0.99$ (Tab. 3). Methods HK and SF give a close value $V_{micro} \approx 0.28$ cm^3/g though the former provides the presence in the material of Z-shaped pores,and the SF-method cylindrical. This value is close to the volume of micropores defined by DR- and DA-methods (Tab. 3). The proportion of micropores defined by DR-, DA-, HK- and SF-methods is 60-68% of the total volume of pores V_Σ. The ratio V_{micro}/V_Σ for the value V_{micro} obtained by t- and α_s-method give lower results. It should be noted that the listed methods are often applied for defining the parameters of activated carbon materials porous system and carbon nanotubes [15, 16].

The obtained difference in micropore volumes for one and the same sample by t-method (α_s-method) and DR (DA)-method is probably that in addition to micropores, mesopores also contribute to the defined volume by DR-method increasing the obtained value V_{micro}. A similar pattern is described in the works by the authors [2, 15, 25] who conduct a comparison of micropore volumes obtained by different methods for several samples of activated coal. For most coal volume value of micropores defined by t- and α_s-method exceeds the corresponding magnitudes calculated by the DR-method. These samples contain micropores but do not have mesopores. At the same time there is a reverse ratio for PCM with both micropores and mesopores: the volume of micropores,defined by the DR-method, is larger than the values calculated by t- and α_s-method and are observed for our PCM samples. This can be explained by the fact that the DR-method takes into account both micropores and mesopores.

The average diameter of pores for CTA-samples defined by BJH and DH methods is the same and equal to 3.89 nm, though the diameter obtained by the DR-method has substantially less value (1.86 nm). The HK method leads to low values (d = 0.3 nm) which by metric order approach to the defects of three-dimensional structure of solids, vacancies, in particular.The SF method gives average values of the diameter which are smaller than those for ultra micropores ($d \leq 1.4$ nm). However, it is unlikely that the porous system of our samples has only represented those pores.

Thermal activation significantly changes the dependence character of the total volume of pores on the diameter of pores (Fig. 8) calculated by the isotherms of desorption through the BJH method which is usually used for estimation of pore distribution by the size [16]. Thermal activation of the original raw material contributes to the increase in the volume of pores of all sizes and develops the pore diameter in the vicinity of 4 nm.

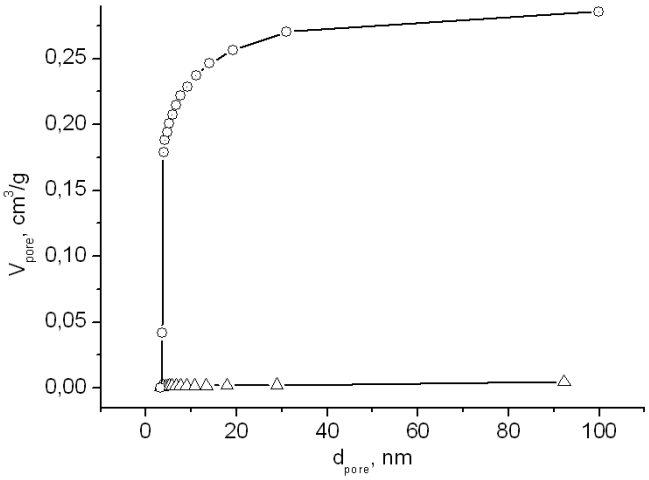

Fig. 8. Dependence of pore volume on their diameter (BJH method) for samples: 1 - outgoing (CA-3); 2 - thermally activated (CTA-3)

The investigation of micropore distribution by the size was carried according to MP- and DFT methods. One can conclude from the MP method of distribution that thermal modification initiates formation of diameter pores < 2 nm with maximum in the vicinity of 0.75 nm (Fig. 9).

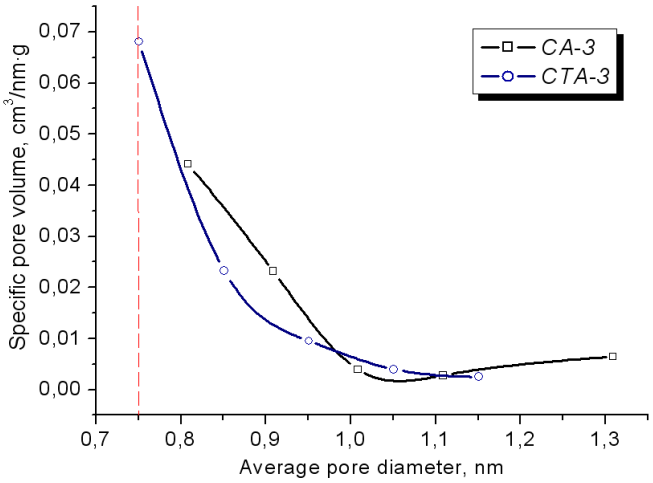

Fig. 9. Distribution of micropores by the size (MP method)

Classical theories such as DR and DA and half empirical approaches, HK and SF in particular, do not fully describe the filling of micropores and narrow mesopores. This leads to an understatement of the true size and error in calculation.A modern approach to the description of adsorption isotherms and pore distribution by the size for microporous materials is based on quantum-mechanical calculation. The essense of the approach is to construct theoretical isotherms for different pores of microporous adsorbent-adsorbate. Calculation is carried out according to the Density Functional Theory (DFT). The DFT method was used to get the distribution of PCM micro- and mesopores. The method takes into account the fundamental molecular parameters that characterize the interaction of gas-gas and gas-solid in the adsorptive system. The results obtained are presented as a set of bar charts in Fig. 10.

The DFT method makes it possible to determine the specific surface , the total pore volume, and their distribution both by the size and by the volume (Tab. 4). The obtained data (Fig. 10, Tab. 4) show that for CA-3 sample the contribution to the specific surface area and total pore volume is made only by micropores. Thermal activation of the CA-3 sample contributes to the development of micropore diameter ~ 1.25 nm and pore diameter ~ 4 nm.

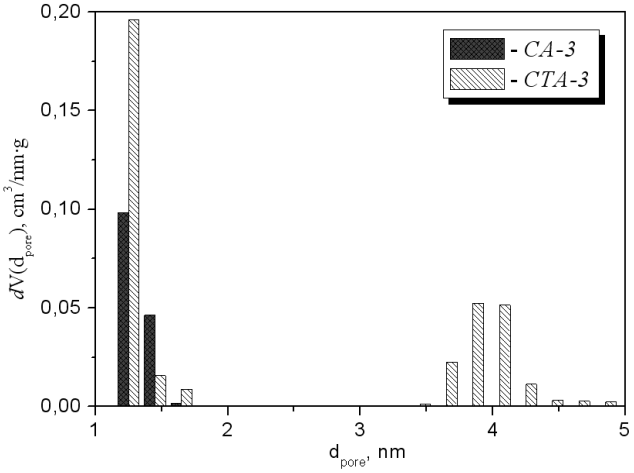

Fig. 10. Distribution of pores by the size (DFT method)

Parameter	*CA-3*	*CTA-3*
Specific surface area, m^2/g	295	609
Total pore volume, cm^3/g	0.146	0.426
Micropore volume (d < 2 nm), cm^3/g	0.146	0.221
Surface area of micropores (d < 2 nm), m^2/g	295	522
Average pore diameter, nm	1.29	3.97

Tab. 4. Structural and adsorptive characteristics of carbon material (DFT method)

Obtained by the methods MP (Fig. 9) and DFT (Fig. 10) dependencies for CA-3 and CTA-3 samples are quantitatively different due to differences in the physical models assigned at the core of these methods. But qualitatively both methods confirm that thermal activation contributes to the development of pores of a certain size.

3. CONCLUSIONS

Thus the temperature of synthesis is an important control of porosity that allows you to receive PCM with adjustable porous structure. Hydrothermal carbonization of apricot pits and further thermal activation of origin raw material forms a high specific surface and porous structure of carbon material. The optimal temperature synthesis of PCM from the enlarged area of micro- and mesopores is 1073 K. Under the conditions of thermal versions of origin raw material enlarges the specific surface area and porous structure of activated carbon, so do the diameter pores up to 5 nm. The most noticeable effect is observed for pores with diameters of 0.75, 1.25 and 4 nm.

To determine the specific surface of plant-extracted porous carbon material the BET-, *t*- and α_s - methods are most correct. The DR method gives inflated values of the specific surface of micropores as compared to the *t*- and α_s - methods. A possible reason for it that the DR method takes into account both micropores and mesopores.

REFERENCES

[1] Barret E.P., Joyner L.C., Halenda P.P. The determination of pore volume and area distributions in porous substances. I. Computations from nitrogen isotherms. *J. Am. Chem. Soc.*, **73** (1) (1951), 373-380. doi: 10.1021/ja01145a126

[2] Bauvan L.A., Tsyba N.N., Tamarkina Y.V., Kucharenko V.A. The effect of potassium hydroxide to the porous system of solid thermolysis products of lignite. *Chemistry and Chemical Engineering. Donetsk: Donetsk National Technical University*, **152** (2009), 99-105. (in Ukrainian)

[3] Brunauer S., Emmett P.H., Teller E. Adsorption of gases in multimolecular layers. *J. Am. Chem. Soc.*, **60** (2) (1938), 309-319. doi: 10.1021/ja01269a023

[4] Burchell T.D. *Carbon Materials for Advanced Technologies*. Pergamon, Amsterdam, 1999.

[5] Butyrin G.M. *Highlyporous materials.* Chemistry, Moscow, 1976. (in Russian)

[6] de Boer J.H., Lippens B.C., Lippens B.G., Broekhoff J.C.P., van der Heuvel A., Osinga Th. J. The t-curve of multimolecular N_2-adsorption. *J. Colloid Interface Sci.*, **21** (4) (1966), 405-414.

[7] Dollimore D., Heal G.R. Pore size distribution in a system considered as an ordered packing of spherical particles. *Journal of Applied Chemistry of the USSR*, **14** (1) (1964), 109.

[8] Dubinin M.M., Radushkevich L.V. On the equation of the characteristic curve for the active carbon. *Reports of the USSR*, **55** (4) (1947), 331-334. (in Russian)

[9] Evans R., Marconi U.M.B., Tarazona P.J. Capillary condensation and adsorption in cylindrical and slit-like pores. *Journal of the Chemical Society, Faraday Transactions 2: Molecular and Chemical Physics*, **82** (1986), 1763-1787.

[10] Fenelonov V.B. *Porous carbon*. Institute of Catalysis SB RAS, Novosibirsk, 1995. (in Russian)
[11] Greg S., Sing K. *Adsorption, Surface Adsorption, Surface, Porosity*. Mir, Moscow, 1984. (in Russian)
[12] Horvath G., Kawazoe K. Method for the calculation of effective pore size distribution in molecular sieve carbon. *J. Chem. Eng. Jpn*., **16** (5) (1983), 470-475. doi: 10.1252/jcej.16.470
[13] Jacobs P., Tompkins F. *Chemistry of the solid state*. Foreign Literature Publishing House, Moscow, 1961. (in Russian)
[14] Karnaukhov A.P. *Supported metal catalysts converting carbon hydrogens.* Novosibirsk, Institute of Catalysis, 1978. (in Russian)
[15] Knerelman E.I., Zvereva G.I., Kislov M.B. Characterization of the products on the basis of single-walled carbon nanotubes by nitrogen adsorption. *Russian Nanotechnology*, **5** (11) (2010), 80-87. (in Russian)
[16] Kurosaki F., Koyanaka H., Tsujimoto M., Imamura Y. Shape-controlled multi-porous carbon with hierarchical micro-meso-macro pores synthesized by flash heating of wood biomass. *Carbon*, **46** (6) (2008), 850−856. doi: 10.1016/j.carbon.2008.02.014
[17] Lippens B.C., de Boer J. H. Studies on pore systems in catalysts: V. The t method. *Journal of Catalysis*, **4** (3) (1965), 319-323. doi: 10.1016/0021-9517(65)90307-6
[18] Lowell S., Shields J. E., Thomas M. A., Thommes M. *Characterization of porous solids and powders: surface area, pore size, and density*. Springer, Dordrecht, Netherlands, 2006.
[19] Lundquist E., Parker G., Rohm Jr. Engineered carbons for ultracapacitor applications. Proceedings of the 14-th International Seminar on Double Layer Capacitors and Similar Energy Storage Devices. Deerfield Beach, Florida (USA) 2004, 14, 69–83.
[20] Marsh H. *Activated Carbon*. Amsterdam, Eslevier, 2006.
[21] Mikhail R.S., Brunauer S., Bodor E.E. Investigations of a complete pore structure analysis: i. Analysis of micropores. *J. Colloid Interface Sci*., **26** (1) (1968), 45-53. doi: 10.1016/0021-9797(68)90270-1
[22] Neymark I.E. *Adsorption and Porosity*. Nauka, Moscow, 1976. (in Russian)
[23] NOVA operating manual, «Quantachrome Instruments», 2010.
[24] Rachiy B.I. Morphology and electrochemical properties of thermally modified nanoporous carbon: published summary of the dissertation on competition of a scientific degree of Candidate of Physical and Mathematical Sciences: specialty 01.04.18 "Physics and Surface Chemistry", Ivano-Frankivsk, 2010.
[25] Rodrigues-Reinoso F. An overview of methods for the characterization of activated carbons. *Pure Appl. Chem.*, **81** (11) (1989), 1859-1866. doi: 10.1351/pac198961111859
[26] Saito R., Dresselhaus M.S., Dresselhaus G. *Physical properties of carbon nanotubes*. World Scientific, New-York, 1998.
[27] Saito A., Foley H.C. Curvature and parametric sensitivity in models for adsorption in micropores. *American Institute of Chemical Engineers Journal*, **37** (1991), 429-436. doi: 10.1002/aic.690370312
[28] Standard Test Method for Carbon Black – Total and external surface area by nitrogen adsorption. D-6556-01. ASTM International, West Conshohocken, Pennsylvania.

Address: B.K. Ostafiychuk, I.M. Budzulyak, N.Ya. Ivanichok, B.I. Rachiy, R.P. Lisovsky: Vasyl Stefanyk Precarpathian National University, 57, Shevchenko Str., Ivano-Frankivsk, 76025, Ukraine.
E-mail: bo@pu.if.ua; ivan-budzulyak@rambler.ru; nashata@ukr.net; bogdan_rachiy@ukr.net; lesrom@rambler.ru.
Received: 21.10.2013; **revised:** 26.03.2014

———————————

Остафійчук Б.К., Будзуляк І.М., Іванічок Н.Я., Лісовський Р.П., Рачій Б.І. Вплив термічної модифікації на розвиток мікропористої структури вуглецевого матеріалу. *Журнал Прикарпатського університету імені Василя Стефаника*, **1** (1) (2014), 41–53.

Проведено порівняння характеристик мікропористої структури вихідного та термічно модифікованого (673 K, 180 хв) вуглецевого матеріалу із сировини рослинного походження. Дані характеристики пористої системи розраховані різними методами на підставі ізотерм низькотемпературної (77 K) адсорбції-десорбції азоту. Встановлено, що термічна модифікація сприяє розвитку питомої поверхні (з 361 $м^2/г$ до 673 $м^2/г$), збільшенню загального об'єму пор (з 0,166 $см^3/г$ до 0,477 $см^3/г$) і об'єму мікропор (з 0,127 $см^3/г$ до 0,173 $см^3/г$). Найбільш ефективно термічна модифікація сприяє утворенню нанопор діаметром 0,75; 1,25 і 4 нм.

Ключові слова: Ключові слова: пористий вуглецевий матеріал, термічна модифікація, низькотемпературна порометрія, структурно-адсорбційні характеристики.

Journal of Vasyl Stefanyk Precarpathian National University
http://jpnu.pu.if.ua
Vol. 1, No. 1 (2014), 55-63

UDC 535.3, 535.51
PACS numbers: 68.37.Hk, 78.66.Hf, 81.15.Ef
doi: 10.15330/jpnu.1.1.55-63

CRYSTAL-QUASICHEMICAL ANALYSIS OF DEFECT SUBSYSTEM OF DOPED PbTe: Sb CRYSTALS AND Pb-Sb-Te SOLID SOLUTIONS

D.M. FREIK, L.V. TUROVSKA

Abstract: Within crystalquasichemical formalism models of point defects of crystals in the Pb-Sb-Te system were specified. Based on proposed crystalquasichemical formulae of antimony doped crystals PbTe:Sb amphoteric dopant effect was explained. Mechanisms of solid solution formation for PbTe-Sb_2Te_3: replacement of antimony ions lead sites Sb_{Pb}^{1+} with the formation of cation vacancies V_{Pb}^{2-} (I) or neutral interstitial tellurium atoms Te_i^0 (II) were examined. Dominant point defects in doped crystals PbTe:Sb and PbTe-Sb_2Te_3 solid solutions based on p-PbTe were defined. Dependences of concentration of dominant point defects, current carriers and Hall concentration on content of dopant compound and the initial deviation from stoichiometry in the basic matrix were calculated.

Keywords: lead telluride, antimony, dopant, solid solution, point defects, crystalquasichemical formulae.

1. INTRODUCTION

IV-VI compounds and solid solutions on basis of them are basic materials for making thermoelectric energy converters in high temperature region (500-750) K, as well photodetectors and radiating structures of infrared optical spectrum [1].

Among them, lead telluride has an important place due to its properties: multivalley nature of its energy spectrum (N = 4), low lattice thermal conductivity ($\chi = 2.09\ 10\ W \cdot K^{-1}\ cm^{-1}$), relatively high current carrier mobility ($\mu \approx 10^3\ cm^{-2}\ V^{-1} \cdot s^{-1}$), the largest value of $\mu\chi^{-1}$, which causes a significant thermoelectric figure of merit (Z_{max}) $Z = \alpha^2\sigma/\chi$, where α – coefficient of thermo-emf, σ – electrical conductivity , χ – coefficient of thermal conductivity. Clearly, large Z (which determined commercial use of thermoelectric material) depends on α and σ, which are sensitive to the nature of electronic states. Thermal conductivity is defined by phonon spectrum of the crystal (χ_l) and the concentration of current carriers (χ_e). Decrease of thermal conductivity components ($\chi = \chi_l + \chi_e$) is one of the effective ways of increase of the thermoelectric figure of merit. In this regard, the search for new compounds with complex crystal structures, which have low thermal conductivity is an urgent problem. Among them are quasi-binary systems (A^{IV} –Ge, Sn, Pb; C^{V} – Bi, Sb; B^{VI} - Te) [17].

Lead telluride crystallizes in NaCl structure, which is a characteristic of ionic crystals. Chemical bond is complex and close to the ion-covalent-metallic. PbTe is characterized by significant deviations from the stoichiometric composition and bilateral homogeneity region and can have both n-type (with

excess metal) and p-type (with excess chalcogen) conduction, causing significant concentration (10^{18}-10^{19}cm^{-3}) of electrically active intrinsic defects [7].

The type of PbTe-Sb diagram is eutectic. The solubility of Sb in PbTe at 820 K is 1.5 at. % [16]. Antimony, acting as a donor, moves homogeneity region limits toward higher equilibrium concentrations [14]. Solubility of Sb_2Te_3 in PbTe for PbTe-Sb_2Te_3 is defined in [9, 10, 15]. At lower temperatures (573-823) K solubility is about (2-4) at. % of Sb [9, 15]. The maximum solubility (~6 at. % Sb) obtained in the research of crystallization of PbTe-Sb_2Te_3 [8] is higher than the solubility at lower temperatures. According to [2], the boundary region of Sb_2Te_3 solubility in PbTe is approximately 2 mole %, and in [13, 15] – (4.5-5) mole %.

Performance device structures are largely determined by defect subsystem of used crystals, which depends on the homogeneity region of compounds, the chemical composition of solid solutions based on them, and technological factors of their synthesis and subsequent treatments of the material. Analyzing the current state of the problem, it should be noted that the ambiguity of the experimental data and theoretical interpretation of the nature and type of point defects and their charge states and energy parameters in crystals based on lead telluride greatly complicates the interpretation of their physical and chemical properties. Therefore, further development of theoretical approaches to the study of the defect subsystem and explanation of existing as well as new experimental data obtained from one standpoint remains an urgent problem.

2. MATERIALS AND METHODS

2.1. DOPED CRYSTALS P-PBTE:SB

2.1.1. ANALYSIS OF DOPANT BEHAVIOR. Taking into account that the valence shell of atoms of V group elements has s^2p^3 configuration, Sb atoms can give (s^2p^0 configuration, valence +3) or accept (s^2p^6 configuration, valence –3) 3 electrons from *p*-state. So dopant in PbTe can be in two charge states Sb^{3+} and Sb^{3-}. In doped crystals PbTe:Sb fraction of electrically active impurity atoms is significantly less than 1, and it evidences that impurity atoms are distributed between the cationic and anionic sublattices [12]. Thus, in doped crystals PbTe:Sb dopant, replacing lead in its sublattice, ionizes from state $Sb^0(s^2p^3)$ in the state $Sb^{3+}(s^2p^0)+3e^-$ and relatively Pb^{2+} sublattice it is in a state $Sb^{3+} \rightarrow Sb_{Pb}^{1+}$ (where it is a donor). In tellurium sublattice dopant ionizes $Sb^0(s^2p^3) \rightarrow Sb^{3-}(s^2p^6) + 3h^+$ and is an acceptor, while relatively Te^{2-} sublattice dopant is in state $Sb^{3-} \rightarrow Sb_{Te}^{1-}$. The fact that the dopant can occupy lead and tellurium sites in PbTe crystal structure and disproportionation of its charge state can be described by the following reaction:

$$Sb^0 \rightarrow Sb_{1-z}^{3+} + Sb_z^{3-} + 3(1-z)e^- + 3zh^+. \qquad (1)$$

Here $z = \frac{[Sb_{Te}^{1-}]}{[Sb_{Pb}^{1+}]+[Sb_{Te}^{1-}]}$ – the value of disproportionation of dopant charge state ($0 \le z \le 1$), e^- – electrons, h^+ – holes.

The relation between $[Sb^{3+}]$ and $[Sb^{3-}]$ determine donor or acceptor dopant effect.

2.1.2. CRYSTALQUASICHEMICAL FORMULAE. For the analysis of the defect subsystem in investigated crystals crystalquasichemical approach was used, It is based on the concept of antistructure [13], which has the form of $\mathbf{V_{Pb}^{//}V_{Te}^{\cdot\cdot}}$ for lead telluride, where $\mathbf{V_{Pb}^{//}}$ and $\mathbf{V_{Te}^{\cdot\cdot}}$ – double-charged lead and tellurium vacancies, respectively; "/" and "•" – negative and positive charges, respectively. Crystalquasichemical formula is written as a superposition of alloying cluster formed on the basis of antistructure of basic matrix and crystal formula of basic compound.

Taking into account the amphoteric effect of Sb dopant in lead telluride crystals (1), alloying cluster can be written as follows:

$$V_{Pb}^{//}V_{Te}^{\cdot\cdot} + Sb^0 \rightarrow \left[V_z^{//}Sb_{1-z}^{\bullet}\right]_{Pb}\left[V_{1-z}^{\cdot\cdot}Sb_z^{/}\right]_{Te} + 3(1-z)e^- + 3zh^+. \qquad (2)$$

Crystalquasichemical formula of p-PbTe with the complex range of point defects in the cation sublattice (single and double-charged Pb vacancies) is represented as [4]:

$$\left[\mathrm{Pb}^{x}_{1-\beta}V^{//}_{\beta(1-\delta)}V^{/}_{\beta\delta}\right]_{\mathrm{Pb}}\left[\mathrm{Te}^{x}_{1-\beta\gamma}V^{\cdot\cdot}_{\beta\gamma}\right]_{\mathrm{Te}}\left(\mathrm{Te}^{x}_{\beta\gamma}\right)_{i}+\beta(2-2\gamma-\delta)h^{+}. \tag{3}$$

Superposition of crystalquasichemical formula of p-PbTe (3) and the alloying cluster (2) presents the crystal-quasichemical formula of p-PbTe:Sb:

$$\begin{aligned}&\left[\mathrm{Pb}^{x}_{(1-\beta)(1-x)}\mathrm{Sb}^{\cdot}_{(1-z)x}V^{//}_{\beta(1-\delta)(1-x)+zx}V^{/}_{\beta\delta(1-x)}\right]_{\mathrm{Pb}}\left[\mathrm{Te}^{x}_{(1-\beta\gamma)(1-x)}\mathrm{Sb}^{/}_{zx}V^{\cdot\cdot}_{\beta\gamma(1-x)+(1-z)x}\right]_{\mathrm{Te}}\left(\mathrm{Te}^{x}_{\beta\gamma(1-x)}\right)_{i}+\\&+\left(\beta(2-2\gamma-\delta)(1-x)+3zx\right)h^{+}+3(1-z)xe^{-},\end{aligned} \tag{4}$$

where x – atomic fraction of dopant (Sb), β– the value of the initial deviation from stoichiometry on the side of Te, δ – coefficient of disproportionation of cationic vacancies charge state, γ –fraction of interstitial tellurium, Te^{x}_{i} – interstitial tellurium, $\mathrm{Pb}^{x}_{\mathrm{Pb}}$, $\mathrm{Te}^{x}_{\mathrm{Te}}$ – lead and tellurium atoms in lattice sites.

2.2. Solid Solutions p-PbTe-Sb$_2$Te$_3$

The possible mechanisms of PbTe-Sb$_2$Te$_3$ solid solution formation are substitution of Sb ions Pb sites with the formation of cation vacancies (mechanism I) or the substitution of Sb ions Pb site with the formation of interstitial tellurium (mechanism II).

2.2.1. Mechanism I. At calculation per 1 tellurium atom and subject to charge state of Sb^{3+} and Te^{2-} ions chemical formula for alloying component is: $\mathrm{Sb}^{3+}_{2/3}\mathrm{Te}^{2-}$. Alloying cluster in this case is:

$$V^{//}_{\mathrm{Pb}}V^{\cdot\cdot}_{\mathrm{Te}}+\mathrm{Sb}^{\cdot\cdot\cdot}_{\frac{2}{3}}\mathrm{Te}^{//}\rightarrow\left[\mathrm{Sb}^{\cdot}_{\frac{2}{3}}V^{//}_{\frac{1}{3}}\right]_{\mathrm{Pb}}\mathrm{Te}^{x}_{\mathrm{Te}}.. \tag{5}$$

Then crystalquasichemical formula of p-PbTe-Sb$_2$Te$_3$ is:

$$\left[\mathrm{Pb}^{x}_{(1-\beta)(1-x)}\mathrm{Sb}^{\cdot}_{\frac{2}{3}x}V^{//}_{\beta(1-\delta)(1-x)+\frac{1}{3}x}V^{/}_{\beta\delta(1-x)}\right]_{\mathrm{Pb}}\left[\mathrm{Te}^{x}_{(1-\beta\gamma)(1-x)+x}V^{\cdot\cdot}_{\beta\gamma(1-x)}\right]_{\mathrm{Te}}\left(\mathrm{Te}^{x}_{\beta\gamma(1-x)}\right)_{i}+\beta(2-2\gamma-\delta)(1-x)h^{+}, \tag{6}$$

where x – molar fraction of Sb$_2$Te$_3$.

2.2.2. Mechanism II. At calculation per 1 Sb atom and subject to charge state of Sb^{3+} and Te^{2-} ions chemical formula for alloying components is written as: $\mathrm{Sb}^{3+}\mathrm{Te}^{2-}_{3/2}$, and its cluster is:

$$V^{//}_{\mathrm{Pb}}V^{\cdot\cdot}_{\mathrm{Te}}+\mathrm{Sb}^{\cdot\cdot\cdot}\mathrm{Te}^{//}_{\frac{3}{2}}\rightarrow\mathrm{Sb}^{\cdot}_{\mathrm{Pb}}\mathrm{Te}^{x}_{\mathrm{Te}}\left(\mathrm{Te}^{\times}_{\frac{1}{2}}\right)_{i}+e^{-}. \tag{7}$$

Then crystalquasichemical formula of p-PbTe-Sb$_2$Te$_3$ is:

$$\left[\mathrm{Pb}^{x}_{(1-\beta)(1-x)}\mathrm{Sb}^{\cdot}_{x}V^{//}_{\beta(1-\delta)(1-x)}V^{/}_{\beta\delta(1-x)}\right]_{\mathrm{Pb}}\left[\mathrm{Te}^{x}_{(1-\beta\gamma)(1-x)+x}V^{\cdot\cdot}_{\beta\gamma(1-x)}\right]_{\mathrm{Te}}\left(\mathrm{Te}^{x}_{\beta\gamma(1-x)+\frac{1}{2}x}\right)_{i}+\beta(2-2\gamma-\delta)(1-x)h^{+}+xe^{-}. \tag{8}$$

2.3. Electric Balance Equation

Proposed mechanisms of doping and crystal formulae (4), (6), (8) make it possible to find analytical expressions of the concentration of individual point defects and current carriers on the magnitude of deviation from stoichiometric composition in the base compound (α, β) and dopant content (x).

In particular for p-PbTe:Sb according to crystalquasichemical formula (4), total electroneutrality equation is written as follows:

$$n + \left|q_{V''_{Pb}}\right|[V''_{Pb}] + \left|q_{V'_{Pb}}\right|[V'_{Pb}] + \left|q_{Sb'_{Te}}\right|[Sb'_{Te}] = p + \left|q_{V^{\cdot\cdot}_{Te}}\right|[V^{\cdot\cdot}_{Te}] + \left|q_{Sb^{\cdot}_{Pb}}\right|[Sb^{\cdot}_{Pb}], \quad (9)$$

where

$$p = A\left(\beta(2-2\gamma-\delta)(1-x)+3zx\right),$$
$$n = 3A(1-z)x,$$
$$[Sb'_{Cd}] = Azx,$$
$$[V'_{Pb}] = A\beta\delta(1-x),$$
$$[V''_{Pb}] = A\left(\beta(1-\delta)(1-x)+zx\right),$$
$$[Sb^{\cdot}_{Pb}] = A(1-z)x,$$
$$[V^{\cdot\cdot}_{Te}] = A\left(\beta\gamma(1-x)+(1-z)x\right),$$
$$\left|q_{V'_{Pb}}\right| = \left|q_{Sb^{\cdot}_{Pb}}\right| = \left|q_{Sb'_{Cd}}\right| = 1,$$
$$\left|q_{V''_{Pb}}\right| = \left|q_{V^{\cdot\cdot}_{Te}}\right| = 2$$

Here $A = \frac{2Z}{a^3}$, Z – number of structural units per unit cell (Z = 4), a – lattice parameter.

Hall concentration of current carriers n_H in this case is defined as:

$$n_H = A\left|3(1-z)x - \beta(2-2\gamma-\delta)(1-x) - 3zx\right|. \quad (10)$$

Similar analysis was done for PbTe-Sb_2Te_3 solid solution.

3. Results and Discussion

3.1. Doped Crystals p-PbTe:Sb

In doped PbTe:Sb crystals when the value of $z < 0.5$ admixture does donor action ($[Sb^{1+}_{Pb}] > [Sb^{1-}_{Te}]$): decrease of hole concentration, thermodynamic p-n-conversion and the subsequent increase of the electron concentration. With the predominance of impurity ions in tellurium sites $z > 0.5$ ($[Sb^{1+}_{Pb}] < [Sb^{1-}_{Te}]$) there is the opposite dependence: significant increase of the concentration of majority carriers. If $z = 0.5$ there is complete self-compensation of dopant ($[Sb^{1+}_{Pb}] = [Sb^{1-}_{Te}]$), and Hall concentration in both cases decreases slightly. Above-mentioned specific behavior of Hall concentration depending on the content of dopant and its charge state is well illustrated on 3d-diagram n_H-x-z (Fig. 1).

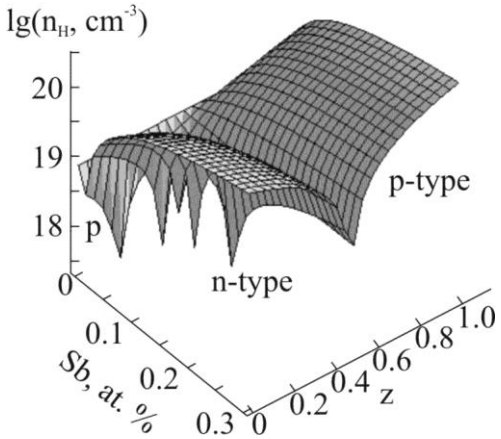

Fig. 1. Dependence of Hall concentration (n_H) in p-PbTe:Sb crystals on dopant content and the value of disproportionation of its charge state (z)

Change of Hall concentration is associated with redistribution of dominant point defects concentration. Thus, dominant defects are antimony ions rooted in lead sublattice Sb_{Pb}^{1+} and tellurium sublattice Sb_{Te}^{1-} of lead telluride crystal lattice, which concentration increases with dopant content increase (Fig. 2 – curves 2, 3). Doubly ionized vacancies of lead $[V_{Pb}^{2-}]$ and doubly charged vacancies of tellurium $[V_{Te}^{2+}]$ also give significant contribution to the conductivity. Concentrations of V_{Pb}^{2-} and V_{Te}^{2+} increases with dopant content increase (Fig. 2 – curves 4, 6). It should be noted that the concentration of V_{Pb}^{1-}, Te_i^0 vary slightly with antimony content increase (Fig. 2 – curves 5, 7).

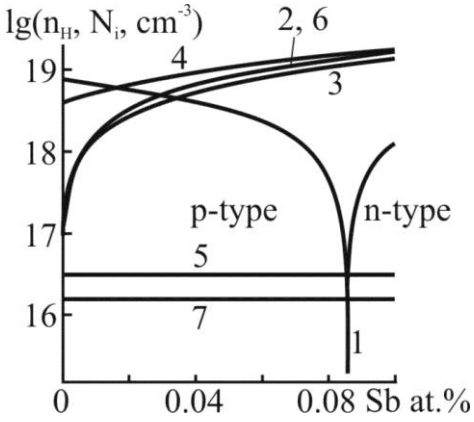

Fig. 2. Dependence of Hall concentration (1 – n_H) and the concentration of point defects (2-7 – N_i) in p-PbTe:Sb crystals on dopant content. N_i: 2 – Sb_{Pb}^{1+}; 3 – Sb_{Te}^{1-}; 4 – V_{Pb}^{2-}; 5 – V_{Pb}^{1-}; 6 – V_{Te}^{2+}; 7 – Te_i^0 ($z = 0.45$)

The proposed mechanism of doping satisfactorily explains the experimentally observed behavior of thermoelectric parameters on dopant content. Thus, based on the data of [3, 5, 11] we can conclude that, in practice, there is realization of condition: $z < 0.5$, ie the concentration of impurity ions $[Sb_{Pb}^{1+}]$ overrides $[Sb_{Te}^{1-}]$. Specifically, comparing the experimental data [5] on the active donor action of antimony (Fig. 3) with the calculation for p-PbTe:Sb (Fig. 1), it was found the value of disproportionation of dopant charge state: $z \approx 0.45$ at the maximum value of the initial deviation from stoichiometry on the side of tellurium. The observed decrease of the concentration of current carriers in PbTe:Sb (Fig. 3 – curve 2) in the content of Sb over ~0.3 at. % can be explained by certain predominance of concentrations of impurity ions in tellurium sites ($[Sb_{Pb}^{1+}] < [Sb_{Te}^{1-}]$).

3.2. Solid Solutions p-PbTe-Sb_2Te_3

Thermoelectric parameters of PbTe-Sb_2Te_3 were studied in several papers [10, 13, 15, 17, 18]. In [15] it was found that the increase of Sb_2Te_3 content in solid solution leads to donor effect with microhardness increase (H) (Fig. 4 – curve 1) and decrease of the coefficient of thermo-emf (α) (Fig. 4 – curve 3). In alloys containing Sb_2Te_3 more (1.5-2) mole % Hall concentration n_H (Fig. 4 – curve 2) and thermo-emf α (Fig. 4 – curve 3) practically do not change. Issues associated with the decrease of the value of thermal conductivity of PbTe-Sb_2Te_3 solid solutions with Sb_2Te_3 content increase were studied in [14, 18]. The value of χ for alloy of PbTe with 1.02 mole % Sb_2Te_3 is $1.25 \cdot 10^{-2}$ $WK^{-1}cm^{-1}$ at 500 K, which confirms the idea of the good thermoelectric efficiency of these solid solutions. The observed phenomenon associated with relation between lattice (χ_l) and electron (χ_e) components of thermal conductivity [17].

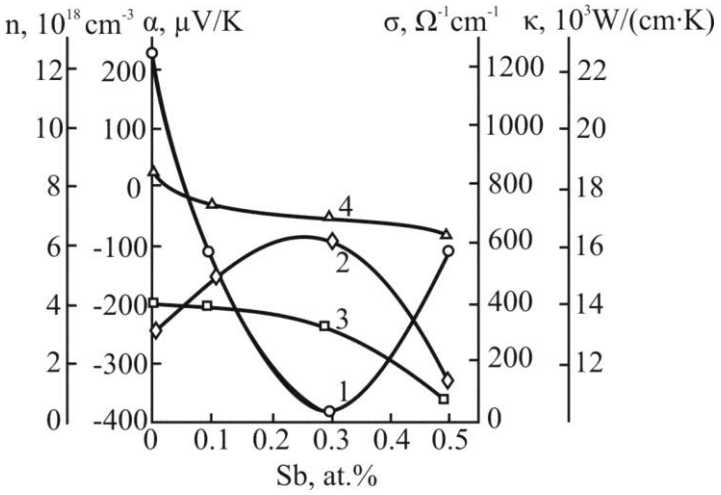

Fig. 3. Dependence of thermoelectric parameters of PbTe:Sb crystals: coefficient of thermo-emf (1 – α), current carrier concentration (2 – n), electrical conductivity (3 – σ) and thermal conductivity (4 – κ) on antimony content [5]

Consider in detail the mechanisms of defect formation in PbTe-Sb_2Te_3 solid solutions. When realization of mechanism I (stoichiometry for chalcogen) there is slight decrease of concentration of major current carriers with Sb_2Te_3 fraction increase (Fig. 5, a – curve 1). With realization of mechanism II (stoichiometry for antimony) in p-PbTe-Sb_2Te_3 (Fig. 5, b – curve 1) with Sb_2Te_3 fraction increase there is decrease of the concentration of current carriers, change of the conductivity type with low dopant content and further increase of electron concentration. Comparing the results of calculations with experimental data on the active donor effect of Sb_2Te_3 (Fig. 4 – curve 2), we can conclude that when the dopant content to 2 mole % of Sb_2Te_3 mechanism II is dominant, and with more of its contents (up to the limit of solubility) mechanism I is dominant.

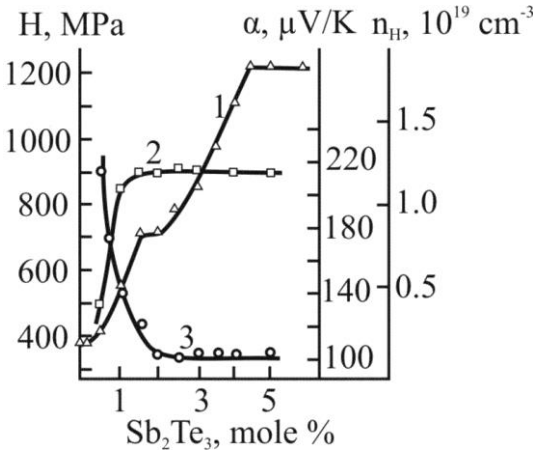

Fig. 4. Dependence of microhardness (1 – H), Hall concentration (2 – n_H) and coefficient of thermo-emf (3 – α) of PbTe-Sb_2Te_3 solid solutions on Sb_2Te_3 content [15]

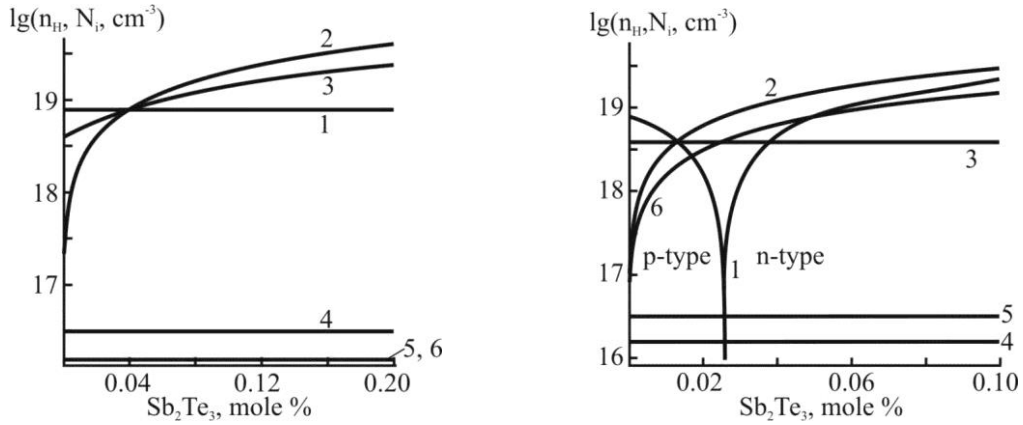

Fig. 5. Dependence of Hall concentration ($1 - n_H$) and the concentrations of point defects (2-6 – N_i) in p-PbTe-Sb_2Te_3 solid solutions on Sb_2Te_3 content at mechanism I (a) and mechanism II (b) realization. N_i: 2 – Sb_{Pb}^{1+}; 3 – V_{Pb}^{2-}; 4 – V_{Pb}^{1-}; 5 – V_{Te}^{2+}; 6 – Te_i^0

Features observed in the change of current carrier concentration are associated with typical correlations between individual point defects (Fig. 5). Thus, for the mechanism I in p-PbTe-Sb_2Te_3 crystals with Sb_2Te_3 content increase there is significant increase of the concentration of ionized antimony in lead sites Sb_{Pb}^{1+} (Fig. 5, a – curve 2) and doubly charged cation vacancies V_{Pb}^{2-} (Fig. 5, a – curve 3). Concentrations of V_{Pb}^{1-}, V_{Te}^{2+}, Te_i^0 decrease slightly (Fig. 5, a – curves 4, 5, 7). For mechanism II in p-PbTe-Sb_2Te_3 crystals the dominant defects are Sb_{Pb}^{1+}, Te_i^0, V_{Pb}^{2-} (Fig. 5, b). Concentrations $[Sb_{Pb}^{1+}]$ and $[Te_i^0]$ increase with dopant content increase (Fig. 5, b – curves 2, 7), and $[V_{Pb}^{2-}]$ decreases slightly (Fig. 5, b – curve 3). Point defects V_{Pb}^{1-} and V_{Te}^{2+} do not significantly affect the conductivity. Concentration of V_{Pb}^{1-} and V_{Te}^{2+} does not change with Sb_2Te_3 content increase (Fig. 5, b – curves 4, 5). Thus, the contribution to the conductivity of substitution defects Sb_{Pb}^{1+} increases, and V_{Pb}^{2-} decreases with dopant content increase.

4. CONCLUSIONS

Based on first proposed crystalquasichemical formulae that take into account the amphoteric behavior of Sb in PbTe crystals, it has been found that with prevalence of antimony in cation sites $[Sb_{Pb}^{1+}] > [Sb_{Te}^{1-}]$, dopant is the donor, and with prevalence of Sb in anion sites ($[Sb_{Pb}^{1+}] < [Sb_{Te}^{1-}]$) dopant is the acceptor, and when $[Sb_{Pb}^{1+}] = [Sb_{Te}^{1-}]$ there is a complete self-compensation of influence of dopant.

It has been shown that in doped crystals PbTe:Sb experimental results are explained satisfactorily provided $[Sb_{Pb}^{1+}] > [Sb_{Te}^{1-}]$. Thus the dominant defects are impurity defects Sb_{Pb}^{1+}, Sb_{Te}^{1-} and vacancies of lead V_{Pb}^{2-} and tellurium V_{Te}^{2+}, which concentration increases with dopant content increase, and the ratio between them determines the type of conductivity of the material.

It has been determined that the value of disproportionation of charge state of dopant in PbTe:Sb is $z \approx 0.45$.

It has been shown that with increasing content of alloying compound in PbTe-Sb_2Te_3 solid solutions to 2 mole % of Sb_2Te_3 substitutions of cation sites and the formation of interstitial tellurium predominant. With more dopant content (up to the limit of solubility) there is a replacement of Pb sites and formation of cation vacancies. In the first case there is thermodynamic p-n-conversion in crystals with the initial p-type conductivity. For the second case there is decrease of Hall concentration in p-PbTe-Sb_2Te_3.

It has been shown that new crystal approaches deepen the possibility of a scientific analysis of the defect subsystem in semiconductor crystals, and determine the technological aspects of the property control.

Work is implemented within the framework of state budget № 0107U006768 of Ministry of Education and Science of Ukraine.

REFERENCES

[1] Abrikosov N.Kh., Shelimova L.Ye. *Semiconductor materials based on $A^{IV}B^{VI}$ compounds*. Nauka, Moscow, 1975. (in Russian)

[2] Abrikosov N.Kh., Yelahina Ye.I., Popova M.A. Research of the PbTe-Sb_2Te_3 system. *Inorganic Materials*, **1** (12) (1965), 2151-2154. (in Russian)

[3] Atakulov Sh.B., Otazhonov S.M., Rasulov R.T., Roziokhunova N., Ilkhomkhuzhaieva Kh. Thermoelectric efficiency of lead telluride films doped by elements of V group. *Physical Surface Engineering*, **7** (1-2) (2009), 119-122. (in Russian)

[4] Boichuk V.M., Tkachyk O.V., Turovska L.V., Dykun N.I. Crystalquasichemical formulae of nonstoichiometric lead telluride with a complex spectrum of point defects and self-doping processes. *Physics and Chemistry of Solids*, **8** (2) (2007), 366-373. (in Ukrainian)

[5] Borisova L.D. Thermoelectric properties of impurity doped PbTe. *Phys. Stat. Sol*., **53** (1) (1979), K19–K22. doi: 10.1002/pssa.2210530157

[6] Bytenskii L.N., Kaidanov V.I., Maksenko V.P., Melnik R.B., Nemov S.A. Self-compensation of the donor action of bismuth in lead telluride. *Physics and Chemistry of Semiconductor*, **18** (3) (1984), 489-492. (in Russian)

[7] Freik D.M., Prokopiv V.V., Halushchak M.O., Pyts M.V., Mateik H.D. *Crystal chemistry and thermodynamics of atomic defects in $A^{IV}B^{VI}$ compounds.* Plai, Ivano-Frankivsk, 1999. (in Ukrainian)

[8] Ikeda T, Haile S.M., Ravi V. A., Azizgolshani H., Gascoin F., Snyder G.J. Solidification processing of alloys in the pseudo-binary PbTe–Sb_2Te_3 system. *Acta Materialia*, **55** (4) (2007), 1227–1239. doi: 10.1016/j.actamat.2006.09.036

[9] Ikeda T., Ravi V.A., Collins L.A., Haile S.M., Snyder G.J. Development and evolution of nanostructure in bulk thermoelectric Pb-Te-Sb alloys. *J. Elect. Mat*., **36** (7) (2007), 716-720. doi: 10.1007/s11664-007-0175-8

[10] Ikeda T., Ravi V.A., Snyder G.J. Formation of Sb_2Te_3 Widmanstätten precipitates in thermoelectric PbTe. *Acta Materialia*, **57** (2009), 666–672. doi: 10.1016/j.actamat.2008.10.005

[11] Kovalchik T.L., Maslakovets Yu.P. The influence of impurities on the electrical properties of lead telluride. *Technical Physics*, **26** (11) (1956), 2417-2431. (in Russian)

[12] Lisniak S.S. Crystal-chemical model of research in solid state chemistry. *Inorganic Materials*, **29** (9) (1992), 1913-1917. (in Russian)

[13] Reynolds R.A. Phase relations and thermoelectric properties of the alloy system SnTe-Bi_2Te_3 and PbTe-Sb_2Te_3. *J. Electrochem. Soc*., **114** (1967), 526-529. doi: 10.1149/1.2426641

[14] Rogacheva E.I. Non-stoichiometry and properties of ternary semiconductor phases of variable composition based on IV–VI compounds. *Journal of Physics and Chemistry of Solids*, **66** (11) (2005), 2104–2111. doi: 10.1016/j.jpcs.2005.10.066

[15] Rogacheva E.I., Laptiev S.A. Homogeneity region of lead monotelluride in Pb-Sb-Te system. *Inorganic Materials*, **20** (8) (1984), 1347-1349. (in Russian)

[16] Shelimova L.Ye., Tomashyk V.N., Hrytsyv V.I. *Phase diagrams of the semiconductor material science: systems based on Si, Ge, Sn, Pb chalcogenide compounds*. Nauka, Moscow, 1991. (in Russian)

[17] Zhu P., Imal Y., Isoda Y., Shinohara Y., Jia X., Zou G. Enhanced thermoelectric properties of PbTe alloyed with Sb_2Te_3. *Journal of Physics Condensed Mater*., **17** (46) (2005), 7319-7326. doi: 10.1088/0953-8984/17/46/015

[18] Zhu P.-W., Imai Y., Isoda Y, Shinohara Y., Jia X.-P., Zou G.-T. High thermoelectric properties of PbTe doped with Bi_2Te_3 and Sb_2Te_3. *Chin. Phys. Lett.*, **22** (8) (2005), 2103-2105. doi: 10.1088/0256-307X/22/8/077

Address: D.M. Freik, Vasyl Stefanyk Precarpathian National University, 57, Shevchenko Str., Ivano-Frankivsk, 76025, Ukraine;
L.V. Turovska, Ivano-Frankivsk National Medical University, 2, Galytska Str., Ivano-Frankivsk, 76018, Ukraine.
E-mail: freik@pu.if.ua; LTurovska@gmail.com.
Received: 14.10.2013; **revised:** 10.02.2014

Фреїк Д.М., Туровська Л.В. Кристалоквазіхімічний аналіз дефектної підсистеми легованих кристалів PbTe:Sb та твердих розчинів Pb-Sb-Te. *Журнал Прикарпатського університету імені Василя Стефаника*, **1** (1) (2014), 55–63.

У рамках кристалоквазіхімічного формалізму уточнено моделі точкових дефектів у кристалах системи Pb-Sb-Te. На основі запропонованих кристалоквазіхімічних формул пояснено амфотерну дію домішки у легованих сурмою кристалах PbTe:Sb. Досліджено механізми утворення твердого розчину $PbTe-Sb_2Te_3$: заміщення йонами стибію позицій плюмбуму Sb_{Pb}^{1+} з утворенням катіонних вакансій V_{Pb}^{2-} (I) або нейтральних атомів телуру в міжвузлі (II). Визначені домінуючі точкові дефекти у легованих кристалах PbTe:Sb і твердих розчинах $PbTe-Sb_2Te_3$ на основі p-PbTe. Розраховано залежності концентрації домінуючих точкових дефектів, носіїв заряду і холлівської концентрації від вмісту легуючої сполуки та величини початкового відхилення від стехіометрії в основний матриці. .

Ключові слова: телурид свинцю, сурми, домішка, твердий розчин, точкові дефекти, кристалоквазіхімічна формула.

Journal of Vasyl Stefanyk Precarpathian National University
http://jpnu.pu.if.ua
Vol. 1, No. 1 (2014), 65-72

UDC 538.9:530.145+537.32:546.4:546.25
PACS numbers: 75.50.Lw, 73.63.Hs, 73.61.Ey
doi: 10.15330/jpnu.1.1.65-72

QUANTUM-DIMENSIONAL EFFECTS IN THERMOELECTRIC CHARACTERISTICS OF LEAD CHALCOGENIDES NANOSTRUCTURES

D.M. FREIK, I.K. YURCHYSHYN, V.YU. POTYAK

Abstract: On the basis of theoretical model of quantum well (QW) with infinitely high walls it was investigated thermoelectric parameters depending on the thickness of the layer of nanostructures IV-VI (PbS, PbSe, PbTe) in the approximation of changing Fermi energy. There have been shown that the dependences of the Seebeck coefficient, electrical conductivity and thermoelectric power factor on well width for lead chalcogenides nanofilms are in good agreement with the experimental data. So, that proves the correctness of used model.

Keywords: lead chalcogenides, nanostructures, quantum size effects.

1. INTRODUCTION

The ability of nanostructured materials to improve thermoelectric (TE) figure of merit has received increasing attention [3, 5]. Reducing the dimension of the material creates conditions for quantum size effect, which leads to an increase in the density of states near the Fermi energy. This allows to maintain high conductivity σ at relatively low Fermi energy E_F, where there are high values of Seebeck coefficient S. Tangible influence of quantum effects on the thermoelectric properties is possible only if the size of the structure in the direction of confinement is comparable with the de Broglie wavelength of carriers. This condition, in particular, holds for structures in the form of quantum wells [7, 8, 9].

The aim of this work was the theoretical explanation of the behavior of a number of thermoelectric (TE) parameters on the width of quantum wells (QW) for lead chalcogenides (PbS, PbSe, PbTe) [7, 8, 9].

2. THEORETICAL MODEL

For quantum well (QW) with high walls, electrons are limited in the direction OZ, and in the OX- and OY-directions their movement is free. Electronic wave function and energy eigenvalue, provided by parabolic energy bands, are defined by expressions [10]:

$$\psi = (\frac{2}{\Omega})^{\frac{1}{2}} \exp(ik_x x + jk_y y)\sin(\frac{n\pi z}{d}), \quad (1)$$

$$E = \frac{\pi^2\hbar^2}{2m_z^* d^2} n^2 + \frac{\hbar^2 k^2}{2m_p^*}, \tag{2}$$

where $k^2 = k_x^2 + k_y^2$, m_z^* - effective mass of the electron along the direction of limitation; $m_p^* = \sqrt{m_x^* m_y^*}$, m_x^*, m_y^* - effective mass of the electron along the axes *ox* and *oy*, Ω – total volume of the layer, *d* – well width, *n* – quantum number which takes integer values.

Number of quantized levels that are below a given energy, is defined by the first part of (2):

$$E_n = \frac{\pi^2\hbar^2}{2m_z^* d^2} n^2 \tag{3}$$

Substituting the value of the Fermi energy (E_F) in (3), we can find the width *d*, where below the Fermi level there is the specified number of levels *n*. The difference between the values of this width for the next two levels will determine the period of oscillations Δd, which is equal to the width d_{min}, where the bottom of the lowest subband coincides with the energy E_F. Thus, from (3) it follows:

$$\Delta d = d_{мін} = \frac{\lambda_F}{2} = \frac{h}{\sqrt{8m_z^* E_F}} \tag{4}$$

From (4) we can see, that the change of the Fermi level value leads to the change of the oscillation period. The Fermi energy value can be expressed through the well width (*d*) and the concentration of carriers in the conduction band [2]:

$$E_F = \varepsilon_1 \frac{(n_0+1)(2n_0+1)}{6} + \frac{\pi\hbar^2}{m^*}\frac{n_{el}}{n_0} d, \tag{5}$$

where ε_1 – the first quantized level, which is determined by the formula (3), when $n = 1$; $n_0 = [(E_F/\varepsilon_1)^{1/2}]$ – the integer part of number $(E_F/\varepsilon_1)^{1/2}$; m^* – carriers effective mass, which is defined as $m^* = (m_\perp^2 m_\parallel)^{1/3}$ [2]; n_{el} – electronic concentration.

If the Fermi level coincides with the bottom of the band n_0, then $E_F(d_0) = \varepsilon_1 n_0^2$. At such the width $(E_F(d_0)/\varepsilon_1)^{1/2}$ – integer. Substituting this value in (5) for d_{n0} is obtained:

$$d_{n_0} = d_0 n_0 \left[1 - \varepsilon_1 \frac{(n_0+1)(2n_0+1)}{6n_0^2}\right]^{1/3}, \tag{6}$$

where $d_0 = (\pi/2n_{el})^{1/3}$. The number n_0 at a given width *d* is the integer part from the solution of equation (6) relatively to n_0, when $d_{n0} = d$.

Thus, the substitution of the integer part from the solution of equation (6) relatively to n_0, when $d_{n0} = d$, in (5) makes it possible to build the ratio $E_F(d)$. Based on the directly proportional dependence of the perpendicular component of the effective mass on energy [2]:

$$m_z^* = m_{z0}^* \left(1 + 2 E_F / \varepsilon_g\right), \tag{7}$$

where m_{z0}^*, ε_g – *z*-component of the effective mass at low concentrations and bandgap, it can be argued that near the Fermi energy the ratio between m_z^* and *d* has the same character as $E_F(d)$.

In the case of quantum well thermoelectric transport coefficients may be obtained from the Boltzmann equation, which is written under the assumption that the electron distribution function in the steady state is stable and may be changed only by the action of external forces and fields. Then the system of electrons comes back to equilibrium due to different relaxation processes with characteristic relaxation times. For quasi-two-dimensional system it can be written [4]:

$$\sigma = \frac{e^2}{T}\Gamma^1, \tag{8}$$

$$S = \frac{E_F}{eT} + \frac{1}{eT}\frac{\Gamma^2}{\Gamma^1}, \tag{9}$$

where σ – conductivity, S – Seebeck coefficient, E_F – the Fermi energy, e – electron charge, T – absolute temperature.

The transport coefficient Γ is defined by the semiclassical approach, whereby particles are limited in potential well. The temperature gradient and electric field are directed along the axis *OX*. Then:

$$\Gamma^1 = -\zeta^{(0)}, \tag{10}$$

$$\Gamma^2 = \zeta^{(1)}, \tag{11}$$

where :

$$\zeta^{(s)} = \frac{2T}{\pi a}\sqrt{\frac{m_y^*}{m_x^*}}\frac{1}{\hbar^2}\sum_{n=1}^{E_n \le E_F}\int_0^\infty E^s \tau\varepsilon\left(\frac{\partial f}{\partial \varepsilon}\right)d\varepsilon\,. \tag{12}$$

Here f – Fermi distribution function, $\varepsilon = E\text{-}E_n$, τ – relaxation time, which in the case of scattering on acoustic phonons is independent from energy [4] ($\tau = \tau_0$), so it can be taken outside the integral.

Under this condition the expressions for the Seebeck coefficient S and electrical conductivity σ can be written as:

$$S = \frac{k_B}{e}\left[\frac{E_F}{k_B T} - \frac{A_1 + A_2}{A_3}\right], \tag{13}$$

$$\sigma = \frac{1}{2\pi d}\frac{2k_B T}{\hbar^2}\sqrt{\frac{m_x^*}{m_y^*}}e^2\tau_0 A_3, \tag{14}$$

where:

$$A_1 = \left(\sum_{n=1}^{En \le E_F}\int_0^\infty x^2\left(-\frac{\partial f_n}{\partial x}\right)dx\right), \tag{15}$$

$$A_2 = \left(\sum_{n=1}^{En \le E_F} E'\int_0^\infty x\left(-\frac{\partial f_n}{\partial x}\right)dx\right), \tag{16}$$

$$A_3 = \left(\sum_{n=1}^{En \le E_F}\int_0^\infty x\left(-\frac{\partial f_n}{\partial x}\right)dx\right) \tag{17}$$

Fermi distribution function has the known form:

$$f_n = \frac{1}{e^{x-\eta_n}+1}, \tag{18}$$

where $x = \varepsilon / k_B T$ – reduced carrier energy and $\eta_n = \xi - E_n'$. Here $\xi = E_F / k_B T$ and $E_n' = E_n / k_B T$, k_B – Boltzmann constant.

The relaxation time in (15) can be estimated based on the mobility μ of *n*-type carriers in the bulk samples [1]:

$$\mu = e\tau_0 / m . \tag{19}$$

3. RESULTS AND DISCUSSION

Based on the experimental dependences [7-9], which show nonmonotonic, oscillatory character of the TE parameters change with changing the thickness of the condensate (Fig. 1), is natural to assume that such behavior is due to the quantization of energy carriers by restricting their movement in the potential well.

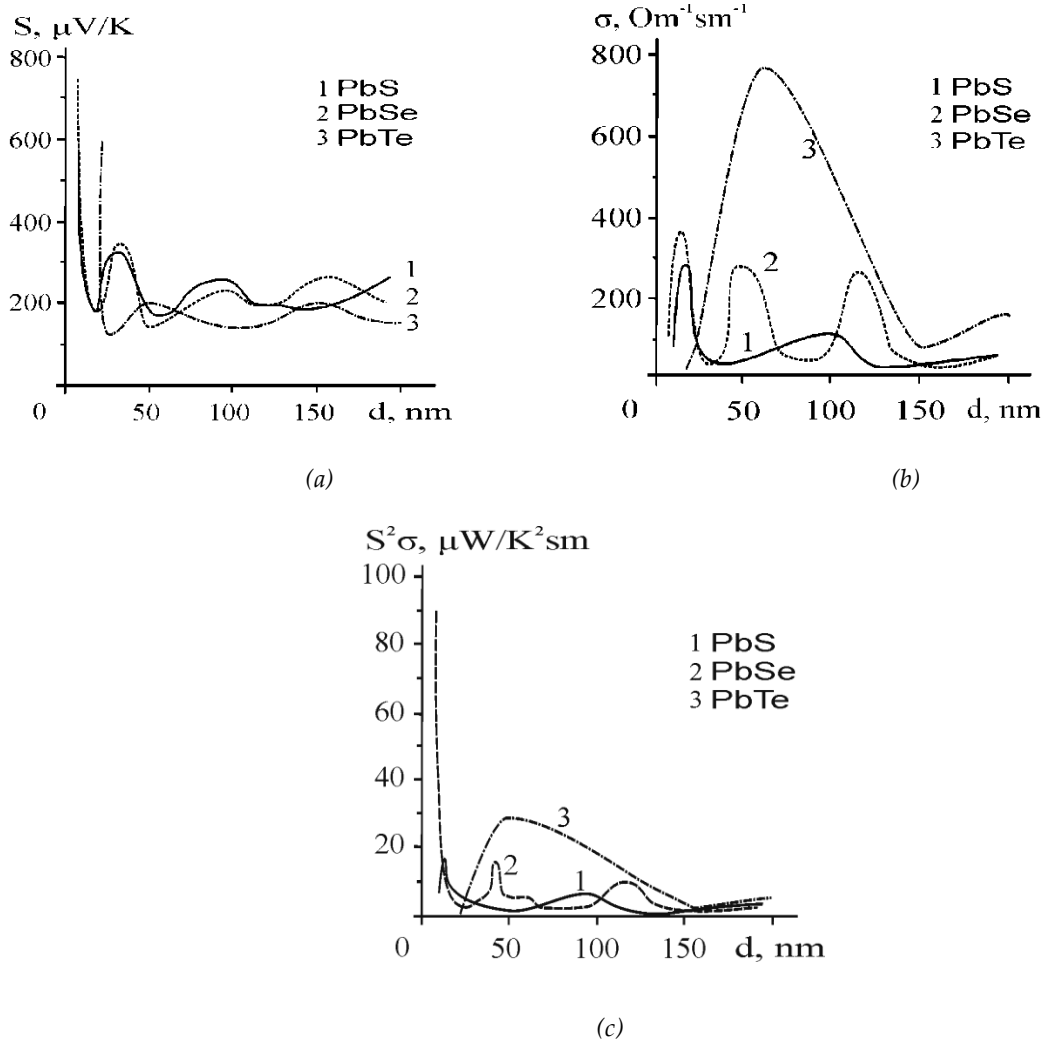

Fig. 1. Experimental dependences of the Seebeck coefficient S (a), electric conductivity σ (b) and TE power factor $S^2\sigma$ (c) on the thickness of the nanofilms PbS, PbSe, PbTe on substrates KCl, covered with a layer of EuS, at T=300 K [7-9]

Increasing the well width on the value of Fermi half-wave leads to new subband below the Fermi energy. At the width of the new band filling in the density of states it is observed the jump, which leads to oscillating behavior.

Consideration of the Fermi energy d-dependence (Fig. 2) in formulas (13)-(18) and z-component of the effective mass in the ratios (16)-(19) allowed us to obtain the corresponding dependences of the Seebeck coefficient S and electrical conductivity σ on the well width for nanofilms of lead

chalcogenides (Fig. 3, a, b). The formula (3) shows that the number of levels below the Fermi energy is determined by d-dependence of the effective mass and actually by E_F, as well as by the well width d. The calculations take into account a change of the Fermi energy, and change of the number of levels below it, depending on the well width. Calculating the electrical conductivity σ by (15) it was assumed that $m_x^* = m_y^*$. In the theoretical model the quantum well width was considered to be equal to the thickness of the condensate in the experimental dependences of relevant parameters. The calculation was carried out in the approximation of constant concentration and carrier mobility across all the range of well width. The values of the last were selected based on relevant experimental measurements (table, according to the data in Fig.1). The resulting dependences of TE coefficients on the width of lead chalcogenides QW are characterized by nonmonotonic oscillating behavior (Fig. 2, 3).

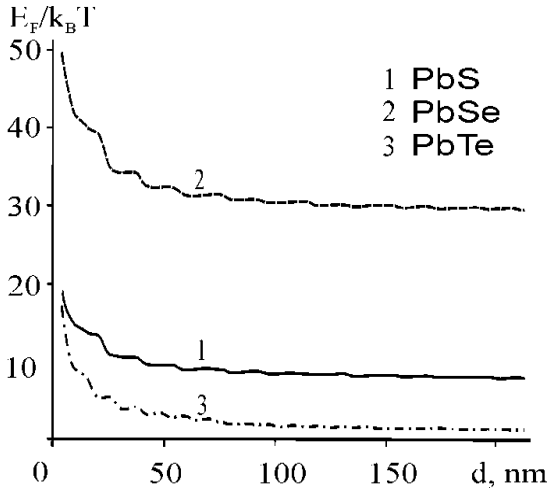

Fig. 2. Calculated values of the Fermi energy E_F in units of k_BT on the width of QW PbS, PbSe, PbTe at T=300 K

	PbS	**PbSe**	**PbTe**
μ, $cm^2/V{\cdot}s$	70	200	1096
n, cm^{-3}	$2{,}5{\cdot}10^{18}$	$4{\cdot}10^{18}$	$0{,}72{\cdot}10^{18}$

Tab. 1. The values of carriers mobility (μ) and concentration (n) for films of n-type lead chalcogenides, which were used in the calculations of thermoelectric coefficients

The dependences of TE parameters on the well width for films of different compounds of lead chalcogenides distinguish by average value of TE parameters throughout the studied range of thicknesses as well as by size and position of extrema (Fig. 3). However, the change character of the curves is identical. So, for all structures at small values of the well width (less than 20 nm) there was revealed the high values of Seebeck coefficient and very low values of conductivity. Increasing the well width leads to a decrease of the value of the Seebeck coefficient and to increase of the value of electrical conductivity. Thus, all these dependencies go to saturation. Note, that this character of theoretical curves change (Fig. 3) is fully consistent with the experimental data (Fig. 1) [7-9], what proves the correctness of the chosen calculation model.

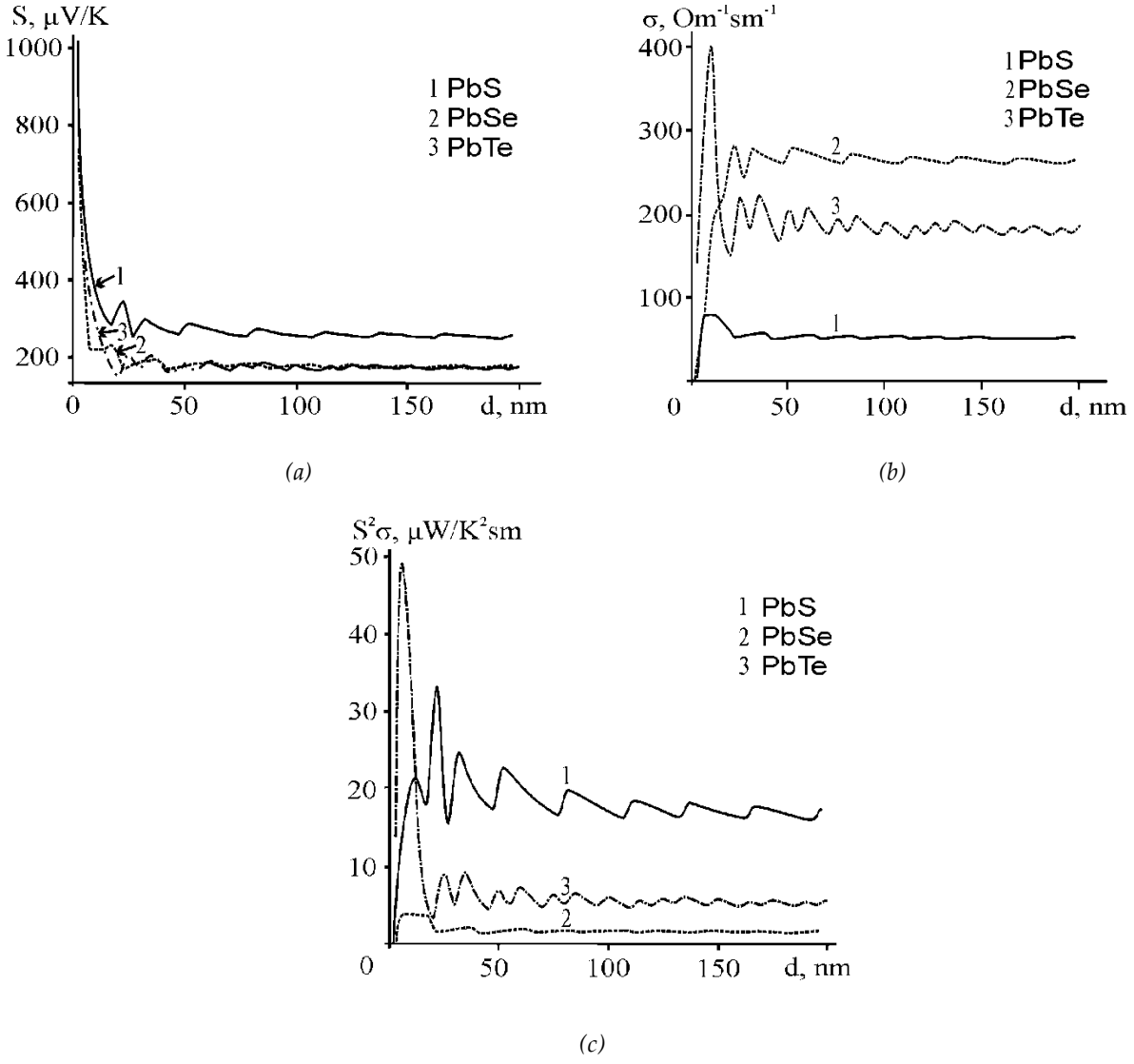

(a) *(b)* *(c)*

Fig. 3. Theoretical dependences of the Seebeck coefficient S (a), electric conductivity σ (b) and TE power factor $S^2\sigma$ (c) on the width of QW for films PbS (1), PbSe (2), PbTe (3) in the model of infinitely deep potential well at T = 300 K

As it is seen from the relation (4) the period of oscillation is inversely proportional to the value of the Fermi energy. Descending character of the Fermi energy (Fig. 2) indicates that with increasing the well width it has place a growth of oscillation period of d-dependences for TE parameters (Fig. 3). The lowest average Fermi energy was obtained for lead telluride (Fig. 2, curve 3). Therefore, PbTe should be characterized by the largest average oscillations period Δd, what is also fully confirmed by experiment (Fig. 1, curve 3) [7-9].

Fig. 3 shows the d-dependences of thermoelectric power factor $S^2\sigma$. In general we can say that the maximum meanings $S^2\sigma$ are smaller than the experimental ones (Fig. 1, c) [6]. Only for compound PbTe the maximum value $S^2\sigma$ is higher than experimental, but this value corresponds to a very small well width, for which no experiment was carried out. On the one hand the cause of this mismatch may be not taking into consideration the limited height of the potential barrier, and on the other hand - the availability of additional experimental factors, which, along with the phenomenon of quantum size effect, influence on the oscillation amplitude of d-dependences of thermoelectric characteristics.

Taking into account the limited height of the potential barriers and calculation the thermal conductivities for lead chalcogenides nanostructures, to determine the d-dependences of thermoelectric figures of merit for relevant structures, will be accomplished in our subsequent works.

4. CONCLUSIONS

For the model of quantum well (QW) with infinitely high walls there were presented the expressions for the Fermi energy and effective mass on the QW width. On this basis, the character of change of oscillation period for the density of states with increasing the well width was defined.

There have been calculated and built the dependences of the Seebeck coefficient, electrical conductivity and thermoelectric power factor for lead chalcogenides nanofilms on their thickness. It was shown that the resulting oscillation character of their profiles are in good agreement with the experimental data.

Work performed under the financing to state budget №0111U001766 (2010-2012) of the Ministry of Education, Youth and Sports of Ukraine, №0110U007674 (2010-2012) of the State Fund of Fundamental Research and №0110U006281 (2010-2013) of the National Academy of Sciences of Ukraine.

REFERENCES

[1] Anselm A.I. *Introduction to Semiconductors Physics*. Science, Moscow, 1978.

[2] Askerov B.M. *Electronic Transport Phenomena in Semiconductors. Home edition of Physical and Technical Literature*. Science, Moscow, 1985.

[3] Davies J.H. *The physics of low-dimensional semiconductors. An introduction*. Cambridge University Press, 1998.

[4] Drabble J.R., Coldsmid H.J. *Thermal Conduction in Semiconductors*. Pergaman Press, London, 1961.

[5] Dresselhaus M.S., Ghen G., Rang M.I., Yang R., Lee H., Wang D., Ren Z., Fleurial J-P., Gogna P. New Directions for Low-Dimensional Thermoelectric Materials. *Adv. Mater*., **19** (8) (2007), 1043-1053. doi: 10.1002/adma.200600527

[6] Freik D.M., Yurchyshyn I.K., Chobaniuk V.M., Nykyrui R.I., Lysiuk Yu.V. Nanostructures on the base of compositions IV-VI for thermoelectric energy converters (overview). *Physical Sensors*, **2** (8) (2011), 41-54. (in Ukrainian)

[7] Rogacheva E.I, Nashchekina O.N, Grigorov S.N., Dresselhaus M.S., Cronin S.B. Oscillatory behaviour of the transport properties in PbTe quantum wells. *Nanotechnology*, **14** (1) (2002), 53–59. doi: 10.1088/0957-4484/14/1/313

[8] Rogacheva E.I., Nashchekina O.N., Vekhov Y.O., Dresselhaus M.S., Cronin S.B. Effect of thickness on the thermoelectric properties of PbS thin films. *Thin Solid Films*, **423** (1) (2003), 115-118. doi: 10.1016/S0040-6090(02)00968-9

[9] Rogacheva E.I., Tavrina T.V., Nashchekina O.N., Grigorov, S.N., Nasedkin K.A., Dresselhaus M.S., Cronin S.B. Quantum size effects in PbSe quantum wells. *Appl. Phys. Lett*., **80** (15) (2002), 2690-2692.

[10] Singh M.P., Bhandari C.M. Non-monotonic thermoelectric behavior of lead telluride in quantum-well-like structures. *Solid State Communications*, **133** (1) (2005), 29-34. doi: 10.1016/j.ssc.2004.09.052

Address: D.M. Freik, I.K. Yurchyshyn, Vasyl Stefanyk Precarpathian National University, 57, Shevchenko Str., Ivano- Frankivsk, 76025, Ukraine;
V.Yu. Potyak, State Enterprise "Center for scientific, Technical and Economic Information", head, 1, Bandera Str., Ivano-Frankivsk, Ukraine.

E-mail: freik@pu.if.ua; i.yurchyshyn@ukr.net; gucul19@gmail.com.

Received: 21.10.2013; **revised:** 03.03.2014

Фреїк Д.М., Юрчишин І.К., Потяк В.Ю. Квантово-розмірні ефекти термоелектричних параметрів наноструктур халькогенідів свинцю. *Журнал Прикарпатського університету імені Василя Стефаника*, **1** (1) (2014), 65–72.

На основі теоретичної моделі квантової ями (КЯ) з нескінченно високими стінками досліджено залежності термоелектричних параметрів від товщини шару наноструктур IV-VI (PbS, PbSe, PbTe) в наближенні змінної енергії Фермі. Показано, що залежності коефіцієнта Зеєбека, електропровідності і термоелектричного коефіцієнта потужності від ширини ями для наноплівок халькогенідів свинцю добре узгоджуються з експериментальними даними, що доводить правильність використаної моделі.

Ключові слова: халькогеніди свинцю, наноструктури, квантово-розмірні ефекти

Journal of Vasyl Stefanyk Precarpathian National University
http://jpnu.pu.if.ua
Vol. 1, No. 1 (2014), 73-79

UDC 547.791.8, 546.01.05+541.1363 548.736
PACS numbers: 75.50.Gg, 75.50.Tt, 75.70.Rf
doi: 10.15330/jpnu.1.1.73-79

TEMPERATURE FREQUENCY CHARACTERISTICS OF CHARGE TRANSITION IN THE $Li_{0.5}Fe_{2.4}Ti_{0.1}O_4$ NON-STOICHIOMETRIC SYSTEM

I.M. GASYUK, V.V. UGORCHUK, L.S. KAYKAN, B.J. DEPUTAT

Abstract: A study of conductivity temperature frequency dependence of $Li_{0.5}Fe_{2.4}Ti_{0.1}O_4$ non-stoichiometric spinel has exhibited frequency dispersion conductivity presence. The time of relaxation (τ) proved to make $2 \cdot 10^{-6}$s within the limits of dispersion. The conductivity size was found to be dependant upon the amount of Fe^{2+} ions in the structure.
Keywords: spinel, energy of activation, Koops' model, conductivity.

1. INTRODUCTION

Stoichiometric lithium ferrospinel $Li_{0.5}Fe_{2.5}O_4$ was studied as a long-range composition of the magnetoactive systems.

These chemical agents possess the rectangular hysteresis loop and the specific phase transformation at the Koori point [2, 7, 8] that allows them to be used in a data storing device. The progress in the digital recording and electronic devices downsizing made the lithium ferric ferrite, the so-called solids, unpopular for research. The special features of a crystalline composition like spinel, natural for these systems, are particularly available through a crystallographic vacancy. This allows us to use them in prospect with a level of other spinels as the cathode active composition of the electrochemical sources of current with the lithium anode. The micro measured crystallites' intercalative characteristics are like popular nanoporous and tabular systems as TiO_2, CoO_2, *GaAs* etc. [3, 12].

Nevertheless, the cathode formation technology provides for the electro conductive additive like graphite, carbon, or any other conductor. Concentration of this component increases in case of crystal grains, which reduces the operating characteristics of lithium current sources.

The problem can be solved in different ways, one of which is spinel synthesis modification in the forming stage of composition by adding different valency ions to the structure [15]. Not only does this method help to change the electronic or p-type conductivity in the composition, it also provides it with specific dielectric properties.

Thus, fair quantity of the modified lithium containing spinels has ion conductivity that lets use them as the solid state electrolyte in the high-temperature current sources [1, 6, 20]. In both cases of spinel alloys' practical application one of the determinative manageable indicators are the conductive and dielectric properties of the composition. They stipulate both electronic spectrum and crystalline structure which is formed in the process of synthesis, and microstructure determined by polycrystalline

grain composition characteristics and intergrain interface [1, 21]. Synthesis adding of metal ions is one of the primary methods of influencing the oxide spinel physical chemical characteristics.

This work has focused on investigation of changing physical properties and spinel *Li-Fe* structure by way of adding univalent, bivalent, trivalent and tetravalent ions. However, analysis of related literature showed that there are no integrated studies in the lithium ferrospinel electroconductive and dielectric characteristics, added with Ti ions, yet the very systems are rather valuable for the lithium source of current in the cathode system aspect [14]. The study [10] presents only the low-frequency dielectric ferrites' qualities of $Li_{0.5+0.5a}Fe_{2.5-1.5a}Ti_aO_4$ *(a = 0, 0.1, 0.2, ...0.7)* composition and analysis of infrared spectra of substance absorption. Frequency temperature dependence of conducting properties of a $Li_{0.5}Fe_{2.4}Ti_{0.1}O_4$ non-stoichiometric system composition has been studied by the method of complex impedance. This composition in regarded to be a long-range active material of the lithium current source cathodes for wide use [18].

2. EXPERIMENTAL PROCEDURE

Polycrystalline samples were obtained according to the traditional ceramic method [23] from Fe_2O_3, TiO_2 (rutile) powder and *LiOH.* Complete synthesis was done by the air sintering method at 1473 K temperature for 8 hours and slow cooling together with a kiln. The process details are described in work [15]. Impedance locus $Z' = f(Z'')$, where Z', Z'' – real and ideal parts of the system complex resistance ($Z = Z' - jZ''$, j – ideal unity) was obtained with the help of impedance spectrometer Autolab PGSTAT 12/FRA- 2 in frequency range 0.01–10^5Hz. The electroconductive dope, which had been applied on the flat perform – sample, was used as an electrode. Under these conditions the ion conductance formed a block and the charge was transferred by the electrons. The sinusoidal voltage amplitude amounted 100mV. The temperature was measured from room temperature to 673 K in increments of 50 K with the help of the SNOL 7.2/1100 kiln that provides temperature control and measurement ~1K.

3. RESULTS AND DISCUSSION

The impedance spectra of the $Li_{0.5}Fe_{2.4}Ti_{0.1}O_4$ system are shown in Fig. 1 in the Nyquist coordinates for different temperatures.

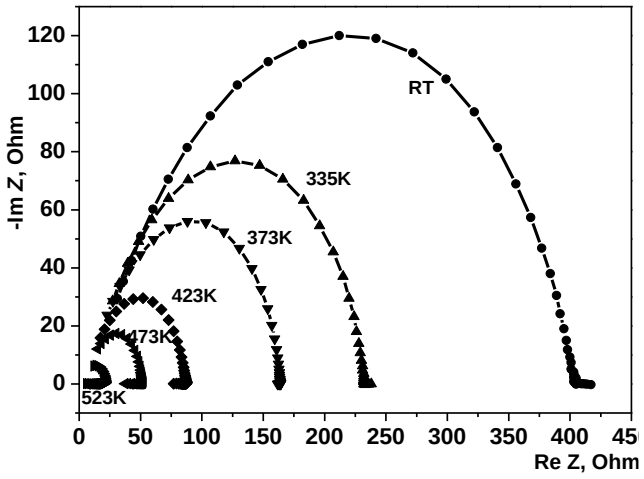

Fig. 1. Impedance temperature dependence locus diagram for $Li_{0.5}$ $Fe_{2.4}Ti_{0.1}O_4$ system

The parametric dependence diagrams $Z' = f(Z'')$, where Z', Z'' – are frequency functions and have an arch shape for all temperature limits of the sample composition under research.

One of the main criteria for the electroconductivity measuring technique is its external electric field frequency dependence. In case of the intermittent mechanism the conductivity increases compared to zone conductivity, which does not depend upon the external field frequency up to $f = 10^9 \ldots 10^{11}$ *Hz* frequency [4, 19].

Frequency dependence of the specific conductivity $\sigma(f)$ (AC – conductivity) for different temperatures is shown in Fig. 2. The $\sigma(f)$ level weakly depends upon the frequency in the $f = 0.01 - 10^3$ *Hz* range. Increasing f upwards of 10^3 Hz abrupt growth of conductivity up to the researched frequency range is observed. At a lower temperature σ dependence is more expressed.

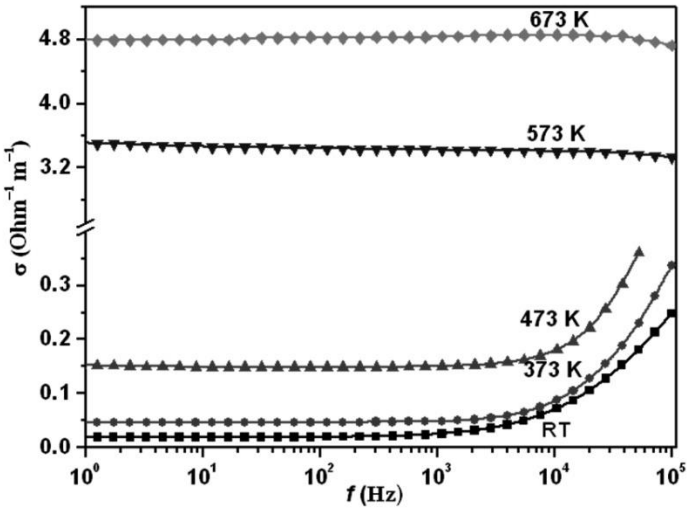

Fig. 2. Frequency and temperature σ dependence graphic chart

In the ferrite physics the most known sample part, first examined in the works of Wagner, Koops etc. [5, 10, 11, 17], can exemplify the obtained results of the AC frequency dependent conductivity. According to that sample part, the spinel is the molded multilayer condenser, grains and grain boundaries of which have different conducting properties. The polycrystalline spinel is supposed to contain large, comparatively high conductivity range with the resistivity constant ρ_g and dielectric penetration ε_g, which are divided with the thin layers of comparatively low conductivity substance with the ρ_b and ε_b amount, that is low-resistance grains and high-resistance grain boundaries. The impedance of such sample part can be shown by the equivalent electric circuit (Fig. 3), where R_1, C_1 and R_2, C_2 are respectively active resistance and capacity reactance of the grains and grain boundaries. The conductivity growth at frequency becomes clear in consideration of the fact that the high-resistance polycrystalline intergrain boundaries “bridging" takes place on the ac field at a certain signal frequency [9].

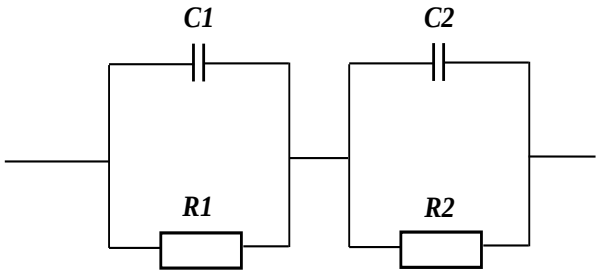

Fig. 3. Equivalent circuit of the grain – layer segment

In the high-frequency range the capacity reactance gets less than active resistance. As a result the whole polycrystalline conductivity is rated by the grains properties whereas the intergrain potential barrier influence at the “grain – boundary” range can be neglected. The distinctive feature of such an

effect is the increasing amount of the spinel specific conductivity σ and the decreasing of electrical transit activation energy at the electric field frequency growth. The frequency dispersion σ can be described with the help of the relaxation composition [10, 22],

$$\sigma(f) = \sigma_{lf} + \frac{\sigma_{lf} - \sigma_{hf}}{1 + (2\pi f \tau)^2} \tag{1}$$

where *lf* and *hf* indicate the limitation level at low (approximately 10^3 Hz) and high (approximately 10^5 Hz), respectively. Relaxation time τ is the qualitative scratch constant for spinels and it has been calculated according to the equation (1). Magnitude τ was revealed to be within the limit (2-6)·10^{-6}s. The generic magnitude τ has been used for approaching the curves $\sigma(f)$, the trends of which coordinate with the experiment (Fig. 4).

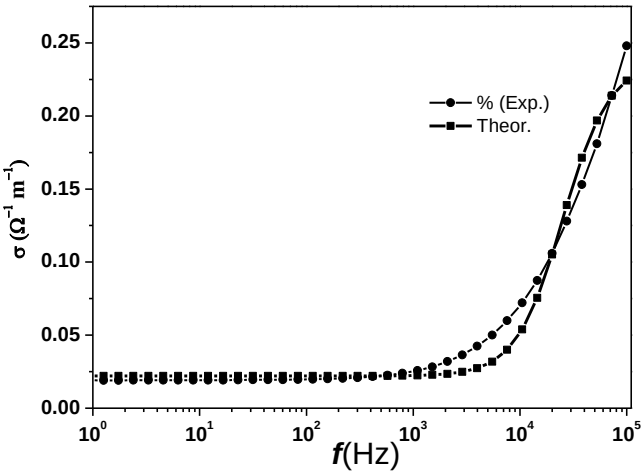

Fig. 4. Experimental and theoretical AC conductivity dependence upon frequency

The electric conductivity mode of behaviour can be explained by the electronic overshooting model $Fe^{2+} \rightarrow Fe^{3+} + e^-$, realized by the electron exchange among certain octahedral positions (B-positions) in the spinel grate [16]. It means that frequency in the range of $10^3 – 10^5$ Hz, fits the electronic overshooting frequency, and influences the electron exchange as far as the frequencies less than 10^3 Hz. The external field does not facilitate the exchange technique. The mode of conductivity behaviour at high frequency of applied electric field $f > 5 \cdot 10^2$ Hz results from electron exchange among Fe^{2+} i Fe^{3+} and does not depend upon this frequency.

Let us consider temperature – frequency dependence of the substance conductivity in question (Fig. 5).

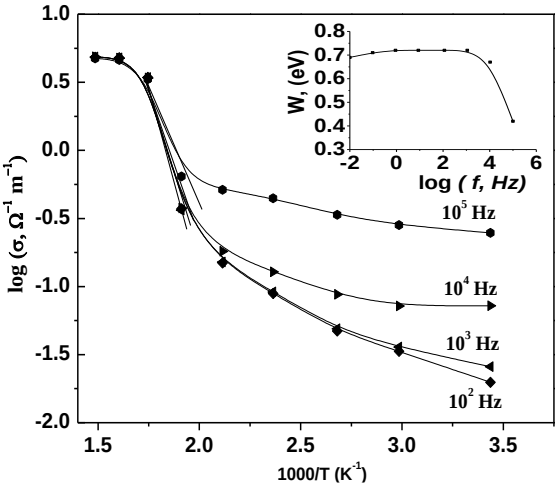

Fig. 5. *Dependence of log σ as function of T^{-1} at different frequencies*

Whereas the spinel oxide is considered to be the semiconductors with the low charge carrier mobility, conductivity dependence upon temperature as a rule is of semiconducting nature and can be expressed by:

$$\sigma = \sigma_0 \exp\left(-\frac{W}{kT}\right) \quad (2)$$

where σ_0 is a pre-exponent multiplier, which does not depend upon temperature and possesses the semiconductor properties, W is activation conductivity energy, T is absolute temperature, k is Boltzmann constant.

The dominant factor in the conductivity process is the charge carrier mobility. Its influence increases at the temperature according to the exponential law and can be determined by the thermal activation energy of W order that exceeds the overshooting potential barrier activation between two B-positions. The barrier negotiation at grain boundary is also obvious. On dependence σ (T^{-1}), modified in Arrhenius coordinates for different frequencies at temperature ~ 500 K, the faintly expressed hump is retraced. It denotes the conversion from the semiconducting nature of conductivity to the metallic one [24].

The conductivity activation energy magnitude W, was calculated for the rectilinear range (intrinsic zone [17] log $\sigma(T^{-1})$ dependence) at a high magnitude of temperature T (about 420 K) graphic of fig. 5. Magnitude W tends toward decreasing in frequency increasing and increases at the Fe^{2+} ion number reduction. Obviously, it can be explained by the exaggeration of the overshooting electron flow conditions.

4. CONCLUSIONS

1. For the first time for non-stoichiometric $Li_{0.5}Fe_{2.4}Ti_{0.1}O_4$ spinel, the temperature frequency dependence of the specific conductance has been fixed while studying the impedance spectra locus curves in the frequency range of 0.01 – 10^5 Hz and temperature range from room to 673 K.

2. Using the classical Debby formulae for the stereotyped dipoles, the specific conductivity experimental dependence upon the external electric field at non-stoichiometric composition sample has been approximated. The qualitative time of the relaxation charging has been inserted to be within (2-6) $\cdot 10^{-6}$ s and is not dependant upon the sample composition and temperature.

3. By measuring the results of spinel conductivity, dependence of electric conductivity activation energy upon the applied electric field frequency has been set. The conductivity activation energy level is determined to decrease with the applied external electric field increase and is rated by the Fe^{2+} ions concentration at the spinel phase of the sample.

4. At temperatures of 500 K the system under study changes the conductivity nature from semiconducting to metallic.

5. The non-stoichiometric spinel of $Li_{0.5}Fe_{2.4}Ti_{0.1}O_4$ composition, obtained by the ceramic method, possesses high conductivity that makes it a prospective cathode system for electrochemical lithium source of current.

REFERENCES

[1] Arillo M.A., Lopez M.L., Perez-Cappe E. at el. Crystal structure and electrical properties of $LiFeTiO_4$ spinel. *Solid State Ionics*, **107** (1998), 307-312.

[2] Blyasse Zh. *Crystallochemistry of Ferrospinell*. Metallurgy, Moscow, 1968. (in Russian)

[3] Gasyuk I.M., Budzulyak I.M., Ugorchuk V.V., Kotsyubynski V.O., Galiguzova S.A. Intercalation Processes in laser irradiation rutile, modify α-Fe and Fe_3O_4. *Electrochemical Power Engineering*, **6** (2) (2006), 86-91. (in Ukrainian)

[4] Katsnelson E.Z. *Structure and Properties of Ferrites.* Science and Engineering, Minsk, 1974. (in Russian)
[5] Koops C.G. On the Dispersion of Resistivity and Dielectric Constant of Some Semiconductors at Audiofrequencies. *Phys. Rev*., **83** (1) (1951), 121-124.
[6] Leonidov L., Leonidova O. at el. Structure, ionic conduction, and phase transformations in lithium titanate $Li_4Ti_5O_{12}$. *Solid State Physics*, **45** (11) (2003), 2183-2188. doi: 10.1134/1.1626760
[7] Letyuk L., Kostyshyn V., Gonchar A. *Technology of Ferrite Materials in Magnetoelectronics*. MISIS, Yekaterinburg, 2005. (in Russian)
[8] Levin B., Tretyakov Y., Letyuk L. *Physical and Chemical Fundamentals of Getting Ferrites, their Properties and Application*. Metallurgy, Moscow, 1979. (in Russian)
[9] Malyshev A.V., Peshev V.V., Pritulov A.M. Dielectric Properties of Lithium–Titanium Ferrite Ceramics. *Russian Physics Journal*, **46** (7) (2003), 691-696. doi: 10.1023/B:RUPJ.0000008199.29313.28
[10] Mazen S.A., Metawe F., Mansour S.F. IR absorption and dielectric properties of Li–Ti ferrite. *J. Phys. D: Appl. Phys.*, **30** (1997), 1799-1808. doi: 10.1088/0022-3727/30/12/018
[11] Mazen S.A., Zaki H.M. AC conductivity of Li-Ge ferrite. *J. Phys. D: Appl. Phys*., **28** (6) (1995), 609-613. doi: 10.1088/0022-3727/28/4/002
[12] Olshanska L.O. The positive electrodes for lithium batteries: problems direction selection. *Electrochemical Power Engineering*, **2** (2) (2002), 66-78. (in Ukrainian)
[13] Ostafiychuk B.J., Gasyuk I.M., Ugorchuk V.V., Sichka M.J. Temperature-frequency characteristics transferred charge at nonstehiometrichri system $Li_{0.5}Fe_{2.4}Ti_{0.1}O_4$. *Physics of Metals and Current Technologies*, **30** (7) (2008), 889-897. (in Ukrainian)
[14] Ostafiychuk B.K., Gasyuk I.M., Kaykan L.S., Deputat B.J., Morushko O.V. Mg-doped $Li_{0.5}Fe_{2.5}O_4$-based spinels. Electrical and Electrochemical Characterization. *Solid State Physics and Chemistry*, **7** (2) (2006), 202-206. (in Ukrainian)
[15] Reddy M.B., Reddy P.V. Low-frequency dielectric behavior of mixed Li-Ti ferrites. *J. Phys. D: Appl. Phys.*, **24** (1991), 975-980. doi: 10.1088/0022-3727/24/6/025
[16] Riabkin L.I, Soskin S.A, Epstein B.S. *Ferrites*. Energy, Moscow, 1968. (in Russian)
[17] Sealy B.J. The temperature dependence of dielectric dispersion in polycrystalline chromites. *Brit. J. Appl. Phys.*, **2** (2) (1969), 447-483. doi: 10.1088/0022-3727/2/4/301
[18] Singhal S., Chandra K. Cation Distribution in Lithium Ferrite $Li_{0.5}Fe_{2.5}O_4$ Prepared via Aerosol Route. *J. Electromagnetic Analysis & Applications*, **2** (1) (2010), 51-55. doi: 10.4236/jemaa.2010.21008
[19] Svirina Y.P. Hall effect magnetoresistance and electrical conductivity in the spinel ferrite. *The Proceedings of the USSR Academy of Sciences, Physical series*, **34** (6) (1970), 1162-1175. (in Russian)
[20] Ugorchuk V.V, Deputat B.J. Impedance characteristics Cathode systems obtained using ceramic synthesis Li-Ti-Fe spinels. In: Ugorchuk V.V, Deputat B.J., Kaikan L.S. Materials of the IXth international conference "Basic Problems of Energy Conversion in the Lithium Electrochemical System", Ufa, Russia, August 14-18, 2006, Reaktiv, Ufa, 2006, 104-106.
[21] Vasiliev R.B., Rumyantseva M.N., Ryabova L.I., Gaskov A.M. Conductivity of SnO_2 ultradisperse ceramics in strong electric fields. *Semiconductors*, **43** (2) (2009), 156-157. doi: 10.1134/S1063782609020067
[22] Wart Ch., Tomson R. *Solid State Physics*. Mir, Moscow, 1966. (in Russian)
[23] Zhuravliov G. I. *Chemistry and Technology of Ferrites*. Chemistry, Leningrad, 1970. (in Russian)
[24] Zyatkov I.I., Miroshkin V. P., Panova Ya.I. Conductivity of single-crystal manganese-zinc ferrites. *Inorganic Materials*, **21** (129) (1985). 2096-2098. (in Russian)

Address: I.M. Gasyuk, V.V. Ugorchuk, L.S. Kaykan, B.J. Deputat: Vasyl Stefanyk Precarpathian National University, 57, Shevchenko Str., Ivano- Frankivsk, 76025, Ukraine.
E-mail: gasyukim@pu.if.ua**;** uhorchuk@rambler.ru.
Received: 18.11.2013; **revised:** 03.02.2014

Гасюк І.М., Угорчук В.В., Кайкан Л.С., Депутат В.Ю. Температурно-частотні характеристики перенесення заряду у нестехіометричній системі $Li_{0,5}Fe_{2,4}Ti_{0,1}O_4$. *Журнал Прикарпатського університету імені Василя Стефаника*, **1** (1) (2014), 73–79.

Вивчалися температурно-частотні залежності провідності нестехіометричної шпінелі $Li_{0,5}Fe_{2,4}Ti_{0,1}O_4$; виявлено існування частотної дисперсії провідності. У межах дисперсії показано, що час релаксації (τ) становить $2 \cdot 10^{-6}$ с. Експериментально встановлено, що величина провідності залежить від кількості іонів Fe^{2+} у структурі.

Ключові слова: шпінель, енергія активації, модель Вагнера-Купса, провідність.

Journal of Vasyl Stefanyk Precarpathian National University
http://jpnu.pu.if.ua
Vol. 1, No. 1 (2014), 81-86

UDC 548.73/.75+621.315.592
PACS numbers: 71.18.+y
doi: 10.15330/jpnu.1.1.81-86

MOSSBAUER STUDY OF YTTRIUM IRON GARNET EPITAXIAL FILMS MAGNETIC MICROSTRUCTURE

V.O. KOTSYUBYNSKY, V.V. MOKLYAK, B.K. OSTAFIYCHUK

Abstract: The magnetic microstructure of the yttrium iron garnet epitaxial films surface layer were studied by conversion electronic Mossbauer spectroscopy method. The presence of two magnetically non-equvivalent positions of Fe^{3+} ions in tetrahedral sites of garnet structure and a paramagnetic phase formed by Fe^{2+} ions were fixed. Using the model of mixed magnetic and quadrupole interaction by the diagonalization of the nuclear Hamiltonian matrix the information about the spatial orientation of the cation sublattices magnetic moments was obtained and the components of electric field gradient tensor at ^{57}Fe nuclei in different crystal non-equvivalent positions were calculated.

Keywords: yttrium iron garnet epitaxial films, conversion electron Mossbauer spectroscopy, effective magnetic field, magnetic moment orientation, electric field gradient.

1. INTRODUCTION

Yttrium iron garnet $Y_3Fe_5O_{12}$ with the traditional practical application in magneto-optical devices and microwave electronics is a convenient model for the study of the ferromagnetic ordering. The crystal structure of $Y_3Fe_5O_{12}$ are assigned to space group Ia3d (O_h^{10}) and is formed by oxygen coordination polyhedra. There are cavities of three types – 24 tetrahedral and 16 octahedral are occupied by Fe^{3+} ions (*d*- and *a*-positions respectively) and 24 dodecahedral which are occupied by Y^{3+} (c-position). Magnetic ordering in Yttrium iron garnet is the result of indirect exchange interaction between Fe^{3+} from different sublattice through the oxygen ions. Magnetic moments of Fe^{3+} ions in *a*-and *d*-positions (M_a and M_d respectively) for an infinite perfect crystal are antiparallel (Neel model). For ferrite-garnet films with the substitutions of Y^{3+} ions by rare earth elements (Sm^{3+}, Lu^{3+}, Eu^{3+}) the large growth uniaxial anisotropy is appeared and the total magnetization is directed along the axis [111]. $Y_3Fe_5O_{12}$ epitaxial films due to the effect of surface demagnetization are characterized by the presence of additional planar magnetization component so the magnetization deviate from the [111] direction to the film plane. The aim of this work is the experimental setting of the spatial orientation of iron ions magnetic moments in the yttrium iron garnet epitaxial films grown on (111) plane and its relationship with parameters intracrystalline electric and magnetic fields.

2. EXPERIMENTAL DETAILS

Yttrium iron garnet films were grown by liquid phase epitaxy method from Y_2O_3-Fe_2O_3-PbO-B_2O_3 melt on nonmagnetic substrate gallium gadolinium garnet $Gd_3Ga_5O_{12}$ with (111) surface plane. For Mossbauer effect probability increasing was used Fe_2O_3 enriched by isotope ^{57}Fe to 14 at.%. Films crystallographic disorientation not exceeds 1°. Films thickness was 2.85 mm. For conversion electrons registration gas proportional counter was used. The activity of Mossbauer isotope ^{57}Co was about 70mKu. Velocity zero instability and registration error were less than 0.5 channel from 256, width of the resonance lines of α-Fe was 0.30 mm/s. The external magnetic fields were formed by system of permanent magnets.

3. RESULTS AND DISCUSSION

Ferrimagnetic ordering of the $Y_3Fe_5O_{12}$ structure is associated with the magnitude of electrostatic fields directed on the nucleus of iron ions by ions of the lattice and their own electron shell. With the simultaneous existence of electric quadrupole and magnetic dipole interactions of approximately equal intensity $|e^2QU_{zz}| \approx |\mu H_{e\phi}|$ an important parameter in the formation of iron magnetically position is the angle θ between the direction of an effective magnetic field on the nucleus Fe^{57} and a direction of the electric field gradient (EFG). The crystal symmetry the EFG tensor is axially symmetric since the tetrahedral positions have symmetry axis of the 4th order and octahedral the third order. So the tensor components have to satisfy the condition (coordinate system is chosen so that the EFG tensor is diagonal): $|U_{xx}| = |U_{yy}| \le |U_{zz}|$; $\eta = (U_{xx} - U_{yy})/U_{zz} = 0$.

Symmetry axes of octahedral positions are corresponding to four possible axes <111> and can be divided into four groups of four atoms in each direction with the same value of EFG. Symmetry axes of tetrahedral positions correspond to the axes <100>. Thus, in general, the garnet structure contains 7 crystal-, and thus magnetically equivalent positions for ions Fe^{3+}, which correspond to the 7 partial components of mossbauer spectrum. In single-crystal ferrite-garnet films (FGF), grown on a substrate with a cut plane (111), there are three possible EFG directions for Fe^{3+} ions in d-sublattice with polar angle $\theta^a_{1,2,3} = 54°44'$; for 1/4 of Fe^{3+} ions in the a-sublattice $\theta^a_4 = 0°$ (EFG direction on the nuclei coincides with the direction [111]), and 3/4 ions $\theta^d_{5,6,7} = 70°32'$. As a result measured experimental values of the quadrupole splitting Δ_{exp} differs from the true quadrupole splitting Δ_{real} of nuclear spin $I = 3/2$: $\Delta_{exp} = \Delta_{real}\dfrac{3\cos^2\theta - 1}{2}$.

As already mentioned, for samples $|e^2QU_{zz}| \approx |\mu H_{e\phi}|$, ie simplified equation [1] to determine the hyperfine structure levels of the nucleus is nonapplicable; generally it is necessary to use a Hamiltonian of mixed hyperfine interaction [2]. In our work, the model of a mixed quadrupole and magnetic interaction issues by diagonalization of the matrix of the nuclear Hamiltonian . Coordinate system is chosen so that the zi axis is parallel to U_{zz}^i, β^i angles are polar and α^i are azimuthal angles between the directions of the effective magnetic field and zi axes . We used a methodical approach proposed in [3]. Diagonalizing the Hamiltonian of hyperfine interactions we established the position of the γ- sextet partial resonance lines in the form of a Lorentzian combination. The parameters that are changed in the approximation process are: the amplitude, the isomer shift δ, the magnetic field H_{ef} , the value of the axial components of the EFG U_{zz}, the β polar angle relative to the orientation of H_{ef} U_{zz} EFG (z axis of the laboratory coordinate system); the polar angle of γ-quantum beam orientation relative to U_{zz} EFG (range of changes is ±2°, calculated with respect to the values geometrically considered). Approximation results of the CEM spectra are shown in the table 1 and in Fig. 1.

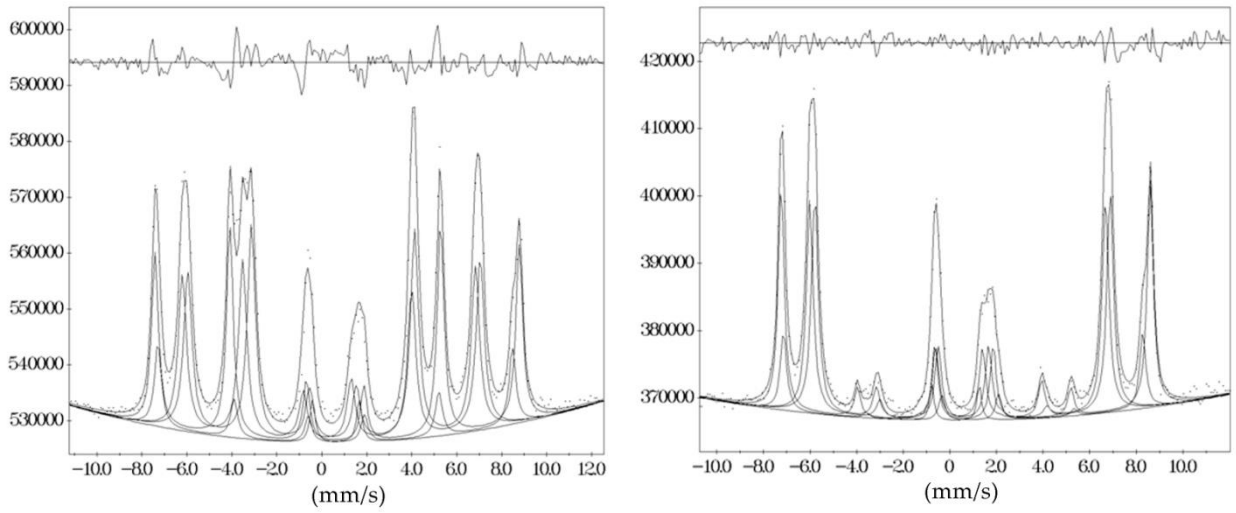

(a) *(b)*

Fig. 1. Conversion electron Mossbauer spectra of the single-crystal film of $Y_3Fe_5O_{12}$, cut plane (111): a) without the external magnetic field; б) within the external magnetic field of 2.8 kOe

To simplify the problem and to find the absolute values of U_{zz} components for different nonequivalent positions the survey the external magnetic field $H_{ext} \approx 2.8$ kOe was applied perpendicularly to the sample surface. In this case the individual magnetic moments of the iron ions were oriented along the direction of the external magnetic field. As shown in Fig. 1 in the partial sextet the intensities of lines 2 and 5 are <8%. These values do not change with increasing of the H_{ext} and are defined by the divergence of γ- quantum beam and experiment geometry. Although, as shown above on the basis of crystallographic assumptions the experimental spectrum must be a superposition of three partial sextet, the nature of the obtained spectra allowed to make an acceptable conclusions about approximations only assuming the presence of two d-positions with different orientations and values of effective magnetic field H_{ef} on iron nuclei.

Crystallographic position	**β°**	**γ°**	**U_{zz}, x10^{21} V/m²**	**H, kOe**	**δ_s, mm/s**	**ω, mm/s**	**S, %**
single-crystal film of $Y_3Fe_5O_{12}$, orientation plane (111)							
a_1	2.9 ± 0.7	70.9	0.60 ± 0.02	503.0 ± 0.1	0.64	0.34	26.7
a_2	61.4 ± 1.6	0.0	0.59 ± 0.02	487.4 ± 0.4	0.63	0.34	8.9
d_1	168.2 ± 0.8	54.7	1.32 ± 0.03	409.2 ± 0.2	0.32	0.43	28.5
d_2	150.2 ± 1.6	54.7	-0.36 ± 0.04	394.4 ± 0.2	0.47	0.47	33.4
D	-	-	-	-	0.61	0.34	2.5
single-crystal film of $Y_3Fe_5O_{12}$, orientation plane (111) in the magnetic field of 2.8 kE							
a_1	46.0 ± 0.8	70.9	0.51 ± 0.10	491.5 ± 0.1	0.67	0.31	28.5
a_2	6.6 ± 5.8	0.0	0.50 ± 0.11	478.2 ± 0.4	0.53	0.31	9.5
d_1	248.7 ± 1.4	54.7	2.09 ± 0.21	400.3 ± 0.2	0.48	0.32	24.7
d_2	261.0 ± 0.8	54.7	-1.52 ± 0.08	387.3 ± 0.2	0.38	0.36	35.2
D	-	-	-	-	0.72	0.31	2.2

Tab. 1. Measurements of the partial components of the experimental mossbauer spectra

The two variant of iron atoms neighbor surrondings in d-positions is defined by stoichiometry distortion of anionic sublattice and uncontrolled entry into garnet structure of impurity atoms from solution - melt in the final stages of epitaxy. It is known [4] that ions Pb^{2+} and Pb^{4+} occupy the octahedral positions displacing the Fe^{3+} with probability of 0.4 and 0.3 respectively. Another uncontrolled impurity is the ions of Pt^{4+} which occupy only a-position. According to [5] from the surface layer of the film thickness of 65 nm more than 2/3 of the conversion electrons are obtained. Low-energy region of the amplitude spectrum (photoelectrons, conversion electrons from the depths of > 85-95 nm) is cut by hardware discriminator and thus the experimental spectrum is formed by an integrated registration of conversion electrons from the depths of < 90 nm. According to [6] the thickness of the transition layer, which is characterized by cationic heterogeneity is < 80 nm. Cationic distribution of the transition layer is largely determined by technological conditions of epitaxy-supercooling temperature of melt and substrate rotation speed. The varies of these factors cause the formation of nonequilibrium surface layer with a concentration of atomic defects ≤ 0.005 per formula unit. These concentrations did not significantly affect the crystalline order, but even slight distortion of the local environment results in changes in the direction of EFG and absolute values of its axial component with the distortions of superexchange interaction. All these factors lead to the emergence of two crystal and magnetic nonequivalent d-positions with noncollinear magnetic moments. Fig. 2. shows the diagram of the effective magnetic fields spatial orientation at the nuclei of ^{57}Fe and the electric fields gradients of individual sublattices. It is known [2] that the effective magnetic field at the core of iron ion and its magnetic moment are antiparallel to each other. Thus, our studies made it possible to establish the magnetic moments spatial orientation of the individual sublattices . We found noncollinearity of magnetic moments of magnetic and crystal nonequivalent iron positions, which is ≈5÷25°, ie there is violation of antiferromagnetic order. It has established that the imposition of an external magnetic field ≈2.8 kOe does not eliminate noncollinearity of magnetic moments.

The above mentioned defects are confirmed by the values of the d- and a-positions populations ratio (n_d/n_a). This parameter is very close to the crystallographic stoichiometric. A significant narrowing of lines in an external magnetic field confirms the presence of magnetically nonequivalent positions of iron in each of the crystallographic nonequivalent sublattices . Reducing the effective magnetic fields at the nuclei of Fe^{3+} in an external magnetic field is almost the same for all selected crystallographic positions. The change of the isomer shift value in an external magnetic field can be caused by a redistribution of the density of s-electrons in Mossbauer nuclei locations and the symmetry of dipped surroundings makes the decisive influence. The values of the axial tensor components for a EFG position are identical within experimental error due to uniformity of dipped surroundings symmetry of Mossbauer nucleus for a_1 and a_2 positions.

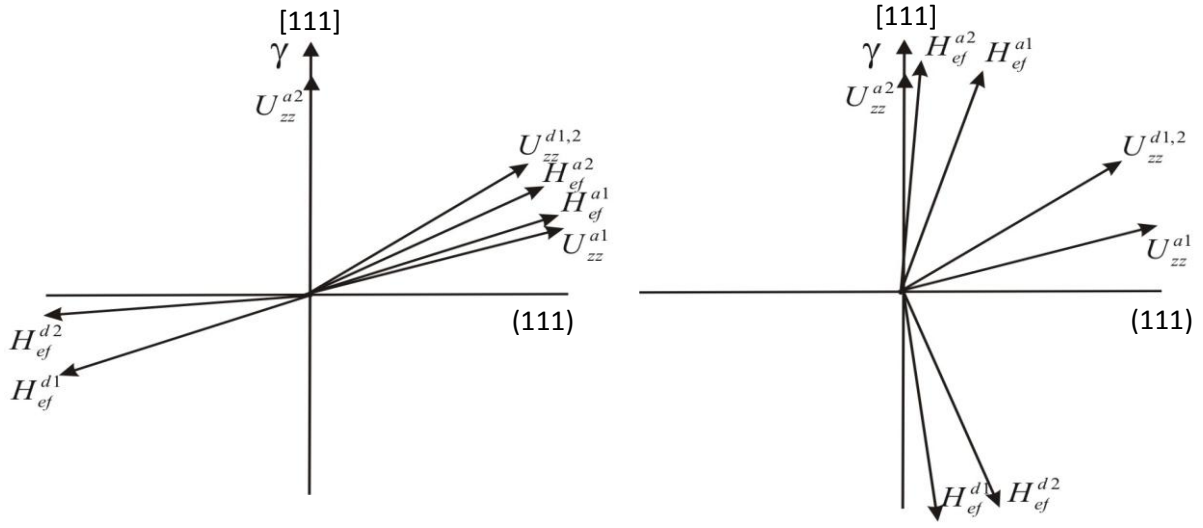

Fig. 2. Diagrams of the effective magnetic fields spatial orientation at the ^{57}Fe nuclei and the electric fields gradients of an individual sublattices

The presence of doublet components corresponding to Fe^{3+} ions in the paramagnetic state in the spectrums of all samples was revealed. The fixation of this part is beyond the error limits. Quadrupole splitting of these doublet components does not depend on the external field and is about 2.05± 0.05 mm/s which can be explained by the presence of a surface layer of iron ions whose valence is reduced from 3+ to 2+. This is result of a large concentration of point defects in the anion sublattice in the surface area and the increasing covalence of the chemical bond in the transition layer film-air. The presence of ferrous iron in the surface layer of the film is confirmed by the values of isomer shift for the paramagnetic component.

4. CONCLUSION

The magnetic microstructure of iron-yttrium garnet epitaxial films is studied. The presence of two magnetically non-equivalent positions of Fe^{3+} which occupy tetrahedral sites are established in the surface layer of the YIG film of orientation (111). The information about the spatial orientation of the magnetic moments of the individual sublattices, experimental values of the parameters of hyperfine interaction and tensor components of the electric field gradient at the nucleus are obtained. The presence of ferrous iron in the surface layer YIG due to the non-stoichiometry of anionic lattice of transition layer film – air has been revealed.

REFERENCES

[1] Bashkirov S., Ivoylov N., Monakhov A., Chistyakov V. Local magnetic field at the iron nuclei in yttrium iron garnet induced by an external magnetic field. *Solid State Physics*, **15** (4) (1973), 1058-1061. (in Russian)

[2] Belozerskii G. , Gittsovich V., Murin A., Khimich Yu., Yakovlev M. Mossbauer effect in oriented cuts of yttrium iron garnet. *Solid State Physics*, **12** (10) (1970), 2878-2881. (in Russian)

[3] Evtiheev N. The elements and devices based on cylindrical domains. *Radio and communication*. Moscow, 1987. (in Russian)

[4] Kundig W. Evaluation of Mössbauer spectra for ^{57}Fe. *Nuclear Instruments and Methods*, **48** (2) (1967), 219–228. doi: 10.1016/0029-554X(67)90320-5

[5] Ostafiychuk B., Tkachuk V., Tkachuk O., Fedoriv V. Mossbauer study of single-crystal YIG films in an external magnetic field. *Metallofyzyka and noveyshye technology*, **22** (11) (2000), 11-16. (in Russian)

[6] Yushchuk S. Layered structure of yttrium iron garnet epitaxial films. *Journal of technical Physics*, **69** (12) (1999), 62-64.

Address: V.O.Kotsyubynsky, V.V. Moklyak, B.K. Ostafiychuk: Vasyl Stefanyk Precarpathian National University, 57, Shevchenko Str., Ivano- Frankivsk, 76025, Ukraine.

E-mail: v_kotsuybynsky@mail.ru.

Received: 04.11.2013; **revised:** 24.03.2014

———————————

Коцюбинський В.О., Мокляк В.В., Остафійчук Б.К. Мессбауерівські дослідження магнітної мікроструктури епітаксійних плівкок залізо-ітрієвого гранату. *Журнал Прикарпатського університету імені Василя Стефаника*, **1** (1) (2014), 81–86.

Методом конверсійної електронної мессбауерівської спектроскопії проведено дослідження тонкої магнітної мікроструктури приповерхневого шару епітаксійної плівки залізо-ітрієвого гранату орієнтації (111). Встановлено наявність двох магнітонееквівалентних позицій іонів Fe^{3+} в тетраедричних вузлах структури граната та парамагнітну фазу, яка формується іонами Fe^{2+}. Застосовуючи метод діагоналізації матриці ядерного гамільтоніану змішаної магнітної дипольної та електричної квадрупольної взаємодій, отримано інформацію про просторову орієнтацію магнітних моментів окремих катіонних підграток досліджуваної структури та значення компонент тензора градієнта електричного поля на ядрах ^{57}Fe у різних кристалічнонееквівалентних позиціях.

Ключові слова: залізо-ітрієвий гранат, конверсійна електронна мессбауерівська спектроскопія, ефективне магнітне поле, тензор градієнта електричного поля.

«Journal of Vasyl Stefanyk Precarpathian National University» is an academic periodical journal of Precarpathian National University, the main task of which is a publication of new original scientific matters, survey and problem articles, in mathematical, economic, medical, human and social sciences.

Every issue of journal refers to such series: "*Series of Natural and Mathematical Sciences*" and "*Series of Social and Human Sciences*".

Journal is issued since 2014 with regularity 4 issues per year.

Author Guidelines

The article should include: the title of the article, the authors and the main information about them (institutional name, email address and contact details), an abstract and keywords in English and Ukrainian languages. All articles are published in English only. The article submitted on the provided UDC, PACS numbers or 2010 Mathematics Subject Classification.

List of references is made as follows:

-BOOK (original in English)
[1] Author1 A.A., Author2 B.B., Author3 C.C. *Title of the book*. PublishingHouse, City, Year.

-BOOK as part of a series of publications (original in English)
[2] Author1 A.A., Author2 B.B., Author3 C.C. *Title of the book*. In: Editor1 A.A., Editor2 B.B. (Eds.) SeriesTitle, Number. PublishingHouse, City, Year.

-BOOK (original Ukrainian or Russian)
[3] Author1 A.A., Author2 B.B., Author3 C.C. *English translation of title of the book*. PublishingHouse, City, Year. (in Ukrainian) or (in Russian)

-ARTICLE (original English) (required indicate doi, if available)
[4] Author1 A.A., Author2 B.B., Author3 C.C. Title of the article. *Title of the Journal,* **Volume** (Number) (Year), PageF-PageL. doi:xxxxxxx

-ARTICLE (original Ukrainian or Russian) (required indicate doi, if available)
[5] Author1 A.A., Author2 B.B., Author3 C.C. English translation of title of the article. *Title of the Journal*, **Volume** (Number) (Year), PageF-PageL. doi: xxxxxxx (in Ukrainian) or (in Russian)

-CONFERENCE ABSTRACT
[6] Author1 A.A., Author2 B.B. Title of abstract. In: Editor1 A.A., Editor2 B.B. (Eds.) Proc. of the Intern. Conf. ``Title of the Conference'', City, Country, Month DateF-DateL, Year, PublishingHouse, City, Year, PageF-PageL.

The submission file should be in MS Word or TeX.

The text is single-spaced; uses a 10,5-point font Palatino Linotype; and all illustrations, figures, and tables are placed within the text at the appropriate points, rather than at the end.

SCIENTIFIC JOURNAL

Journal of Vasyl Stefanyk Precarpathian National University

Vol. 1, No. 1, 2014

Series Natural and Mathematical Sciences

Technical Editor: Tanya Ilechko (*E-mail*: kolitania@yandex.ua)

Publishing house Certificate DK № 2718 from 12.12.2006

Publishing house of Vasyl Stefanyk Precarpathian National University,
1, Bandery Str., 76018, Ivano-Frankivsk, Ukraine. *Tel*.: +38(0342)71-56-22, *e-mail*: vdvcit@pu.if.ua